



UPPSALA
UNIVERSITET

*Digital Comprehensive Summaries of Uppsala Dissertations
from the Faculty of Science and Technology 1277*

Atomic layer deposition of zinc tin oxide buffer layers for Cu(In,Ga)Se₂ solar cells

JOHAN LINDAHL



ACTA
UNIVERSITATIS
UPSALIENSIS
UPPSALA
2015

ISSN 1651-6214
ISBN 978-91-554-9313-4
urn:nbn:se:uu:diva-260882

Dissertation presented at Uppsala University to be publicly examined in Högssalen, Lagerhyddsvägen 1, Uppsala, Friday, 16 October 2015 at 13:00 for the degree of Doctor of Philosophy. The examination will be conducted in English. Faculty examiner: Research Director Negar Naghavi (French National Centre for Scientific Research).

Abstract

Lindahl, J. 2015. Atomic layer deposition of zinc tin oxide buffer layers for Cu(In,Ga)Se₂ solar cells. *Digital Comprehensive Summaries of Uppsala Dissertations from the Faculty of Science and Technology* 1277. 104 pp. Uppsala: Acta Universitatis Upsaliensis. ISBN 978-91-554-9313-4.

The aim of this thesis is to provide an in-depth investigation of zinc tin oxide, Zn_{1-x}Sn_xO_y or ZTO, grown by atomic layer deposition (ALD) as a buffer layer in Cu(In,Ga)Se₂ (CIGS) solar cells. The thesis analyzes how changes in the ALD process influence the material properties of ZTO, and how these in turn affect the performance of CIGS solar cells.

It is shown that ZTO grows uniformly and conformably on CIGS and that the interface between ZTO and CIGS is sharp with little or no interdiffusion between the layers. The band gap and conduction band energy level of ZTO are dependent both on the [Sn]/([Zn]+[Sn]) composition and on the deposition temperature. The influence by changes in composition is non-trivial, and the highest band gap and conduction band energy level are obtained at a [Sn]/([Zn]+[Sn]) composition of 0.2 at 120 °C. An increase in optical band gap is observed at decreasing deposition temperatures and is associated with quantum confinement effects caused by a decrease in crystallite size. The ability to change the conduction band energy level of ZTO enables the formation of suitable conduction band offsets between ZTO and CIGS with varying Ga-content.

It is found that 15 nm thin ZTO buffer layers are sufficient to fabricate CIGS solar cells with conversion efficiencies up to 18.2 %. The J_{sc} is in general 2 mA/cm² higher, and the V_{oc} 30 mV lower, for cells with the ZTO buffer layer as compared to cells with the traditional CdS buffer layer. In the end comparable efficiencies are obtained for the two different buffer layers. The gain in J_{sc} for the ZTO buffer layer is associated with lower parasitic absorption in the UV-blue region of the solar spectrum and it is shown that the J_{sc} can be increased further by making changes to the other layers in the traditional CdS/i-ZnO/ZnO:Al window layer structure. The ZTO is highly resistive, and it is found that the shunt preventing i-ZnO layer can be omitted, which further increases the J_{sc}. Moreover, an additional increase in J_{sc} is obtained by replacing the sputtered ZnO:Al front contact with In₂O₃ deposited by ALD. The large gain in J_{sc} for the ZTO/In₂O₃ window layer stack compensates for the lower V_{oc} related to the ZTO buffer layer, and it is demonstrated that the ZTO/In₂O₃ window layer structure yields 0.6 % (absolute) higher conversion efficiency than the CdS/i-ZnO/ZnO:Al window layer structure.

Keywords: CIGS; Solar cells; Thin film; Buffer layer; TCO; Window layer; Zinc tin oxide; ZTO; Indium oxide

Johan Lindahl, Department of Engineering Sciences, Solid State Electronics, Box 534, Uppsala University, SE-75121 Uppsala, Sweden.

© Johan Lindahl 2015

ISSN 1651-6214

ISBN 978-91-554-9313-4

urn:nbn:se:uu:diva-260882 (<http://urn.kb.se/resolve?urn=urn:nbn:se:uu:diva-260882>)

*A single ray of sunlight is enough to
drive away many shadows.*

Dedicated to friends and family.

List of papers

This thesis is based on the following papers, which are referred to in the text by their Roman numerals.

- I J. Lindahl, U. Zimmerman, P. Szaniawski, T. Törndahl, A. Hultqvist, P. Salomé, C. Platzer-Björkman, and M. Edoff, "Inline Cu(In,Ga)Se₂ Co-evaporation for High-Efficiency Solar Cells and Modules," *IEEE Journal of Photovoltaics*, vol. 3, no. 3, pp. 1100-1105, 2013.
- II M. Kapilashrami, C. X. Kronawitter, T. Törndahl, J. Lindahl, A. Hultqvist, W-C. Wang, C-L. Chang, S. S. Mao, and J. Guo, "Soft X-ray characterization of Zn_{1-x}Sn_xO_y electronic structure for thin film photovoltaics," *Physical Chemistry Chemical Physics*, vol. 14, no. 29, pp. 10154-10159, 2012.
- III J. Lindahl, J. T. Wätjen, A. Hultqvist, T. Ericson, M. Edoff, and T. Törndahl, "The effect of Zn_{1-x}Sn_xO_y buffer layer thickness in 18.0% efficient Cd-free Cu(In,Ga)Se₂ solar cells," *Progress in Photovoltaics: Research and Applications*, vol. 21, no. 8, pp. 1588-1597, 2013.
- IV J. Lindahl, C. Hägglund, J. T. Wätjen, M. Edoff, and T. Törndahl, "The effect of substrate temperature on atomic layer deposited zinc tin oxide," *Thin Solid Films*, vol. 586, pp. 82-87, 2015.
- V J. Lindahl, J. Keller, O. Donzel-Gargand, P. Szaniawski, M. Edoff, and T. Törndahl, "Deposition temperature induced conduction band changes in zinc tin oxide buffers layers for Cu(In,Ga)Se₂ solar cells," Manuscript.
- VI J. Keller, J. Lindahl, M. Edoff, L. Stolt, and T. Törndahl, "Potential gain in photocurrent generation for Cu(In,Ga)Se₂ solar cells by using In₂O₃ as a transparent conductive oxide layer," *Progress in Photovoltaics: Research and Applications*, DOI: 10.1002/pip.2655, early view, 2015.

Reprints were made with permission from the respective publishers.

The author's contributions to the papers

- I Most of the planning of the experimental work. All of the solar cell fabrication and analysis. Main author.
- III Sample fabrication and writing the corresponding part of the paper.
- III Most of the planning of the experimental work. All of the sample fabrication, solar cell measurements and material characterization with exception of the TEM, XPS and RBS sample analysis. Main author.
- IV Most of the planning of the experimental work. All of the sample fabrication. The XRR and XRF characterization. Main author.
- V Most of the planning of the experimental work. All of the sample fabrication. All solar cell measurements. Main author.
- VI Part of the planning of the experimental work. Some of the sample fabrication. The XRR and some of the XRF characterization. Co-author.

Additional papers

The following papers are the result of work done under the Ph.D. project but are not included as part of this thesis:

P. Szaniawski, J. Lindahl, T. Törndahl, U. Zimmerman, and M. Edoff, “Light-enhanced reverse breakdown in Cu(In,Ga)Se₂ solar cells,” *Thin Solid Films*, vol. 535, no. 1, pp. 326-330, 2013.

M. Edoff, J. Lindahl, J. T. Wätjen, and T. Nyberg, “Gas flow sputtering of Cu(In,Ga)Se₂ for thin film solar cells. In *Proceedings of 42nd IEEE Photovoltaic Specialist Conference*, 2015.

Contents

1.	Introduction	13
2.	Basic concepts of solar cells	17
2.1	Energy bands in semiconductors.....	17
2.2	Recombination mechanisms	18
2.3	Photoelectric and photovoltaic effects	19
2.4	The p-n junction.....	20
2.5	Charge separation in a solar cell diode	22
2.6	Current-voltage characteristics	23
2.7	The solar cell module.....	26
3.	The Cu(In,Ga)Se ₂ solar cell.....	27
3.1	The CIGS solar cell stack.....	27
3.1.1	Substrate	29
3.1.2	Back contact.....	29
3.1.3	CIGS absorber.....	29
3.1.4	The window layer stack	33
3.1.5	Shunt preventing layer	33
3.1.6	Front contact	33
3.1.7	Grid	34
3.1.8	Anti-reflective coating	35
3.1.9	Scribing.....	35
3.2	Buffer layer engineering theory	37
3.2.1	Recombination paths in Cu(In,Ga)Se ₂ solar cells.....	37
3.2.2	Inversion of the absorber close to the junction	37
3.2.3	Buffer layer band line-up.....	38
3.2.4	Different buffer layers	40
3.2.5	Atomic layer deposition of buffer layers	41
4.	Solar cell characterization methods	46
4.1	Current density vs. voltage.....	46
4.2	Quantum efficiency	48
4.3	Open circuit voltage vs. temperature	49
4.4	Numerical simulations	51

5.	Material properties of ZTO thin films deposited by ALD	52
5.1	The ALD process for ZTO	53
5.2	General ALD growth of ZTO	54
5.3	Composition of ALD ZTO	57
5.4	ALD growth of ZTO on CIGS	60
5.5	Structure of ALD ZTO	63
5.6	Optical properties of ALD deposited ZTO	66
6.	Performance of CIGS solar cells with ZTO buffer layers	69
6.1	General performance of the ÅSC baseline CIGS	69
6.2	Performance of ZTO buffer layers as compared to CdS	69
6.3	Conduction band line-up in ZTO	72
6.3.1	Conduction band energy changes due to composition	72
6.3.2	Conduction band energy changes due to morphology	73
6.4	The effect of ZTO thickness on solar cell performance	78
7.	Window layer engineering	80
7.1	Omitting the i-ZnO layer	80
7.2	Replacing the ZnO:Al contact with In ₂ O ₃	81
8.	Concluding remarks and outlook	85
	Summary in Swedish	87
	Acknowledgements	90
	Appendix I	92
	Profilometry	92
	X-ray reflectivity	92
	Electron microscopy	92
	Scanning electron microscopy	92
	Transmission electron microscopy	93
	X-ray diffraction	93
	Rutherford backscattering spectroscopy	93
	X-ray Spectroscopy	94
	X-ray absorption spectroscopy	94
	X-ray photoelectron spectroscopy	95
	Energy dispersive X-ray spectroscopy	95
	X-ray fluorescence	95
	X-ray emission spectroscopy	95
	Secondary ion mass spectroscopy	96
	Reflectance-transmittance spectroscopy	96
	Ellipsometry	96
	Four point probe	97
	Hall measurement	97
	References	98

Abbreviations

PV	Photovoltaic	η	Conversion efficiency
CIGS	Cu(In,Ga)Se ₂	R_S	Series resistance
ZTO	Zn _{1-x} Sn _x O _y	G_{SH}	Shunt conductivity
ALD	Atomic Layer Deposition	MPP	Maximum power point
E_F	Fermi level energy	P_{out}	Output power
VB	Valence band	P_{in}	Incoming power
E_V	Valence band energy maximum	ÅSC	Ångström Solar Center
CB	Conduction band	SLG	Soda lime glass
E_C	Conduction band energy minimum	TCO	Transparent conducting oxide
E_g	Band gap energy	i-ZnO	Intrinsic zinc oxide
SRH	Shockley-Read-Hall recombination	ZnO:Al	Aluminum doped zinc oxide
SCR	Space charge region	RF	Radio frequency
QNR	Quasi-neutral region	AR	Anti-reflective
J	Current density	Φ_b	Recombination barrier
V	Voltage	ΔE_C	Conduction band offset energy
V_{bi}	Built in potential	ΔE_V	Valence band offset energy
q	Electron charge	CBO	Conduction band offset
N_{CB}	Effective density of states in CB	CBD	Chemical bath deposition
N_{VB}	Effective density of states in VB	EQE	External quantum efficiency
N_A	Density of acceptors	IQE	Internal quantum efficiency
N_D	Density of donors	E_A	Activation energy
χ	Electron affinity	J_{00}	Saturation current density pre-factor
DC	Direct current	$k_B T/q$	Thermal voltage
J_0	Diode current density	LED	Light-emitting diode
k_B	The Boltzmann constant	KCN	Potassium cyanide
T	Temperature	R_{SH}	Sheet resistance
J_L	Photo generated current density	UV	Ultraviolet
A	Ideality factor		
J-V	Current-voltage characteristics		
J_{SC}	Short circuit current density		
V_{OC}	Open circuit voltage		
J_{MP}	Maximum power current density		
V_{MP}	Maximum power voltage		
FF	Fill factor		

1. Introduction

Today's energy supply and energy use are unsustainable from economic, environmental and social perspectives. Driven by economic activity and a growing global population, the greenhouse gas emissions are expected to increase, unless more vigorous efforts to reduce emissions are facilitated. The Intergovernmental Panel on Climate Change (IPCC) baseline scenario predicts an increase in global mean surface temperature of between 3.7 °C to 4.8 °C in 2100 as compared to pre-industrial levels [1]. At the United Nations Climate Change Conference meeting in Cancun, Mexico in 2010, the world leaders agreed on a goal to limit the increase in global mean surface temperature in 2100 to 2.0°C. To be able to prevent the temperature from exceed a 2.0 °C increase, more rapid improvements in energy efficiency and a tripling to nearly a quadrupling of the share of zero- and low carbon energy supply from renewables, nuclear energy and fossil energy or bioenergy with carbon dioxide capture and storage must be implemented by year 2050 [1].

The irradiation from the sun that enters the atmosphere is on a global mean 340 W/m² [2] and this energy is the source of more than 99.9% of all renewable energy flows on the Earth's surface [3]. A small portion of the solar energy is converted into wind, flowing water, temperature and salt gradients and energy bound in plants and animals. As some irradiation is reflected or absorbed in the atmosphere, the irradiation that hits the surface of the earth is on a global mean 185 W/m² [2]. With an area of 5.1×10^8 km² the surface of the earth receives 94 400 TW on average, or 8.266×10^8 TWh per year. This is 7915 times more than mankind's total energy consumption of 104 400 TWh in 2012 [4]. Thus, the greatest potential for renewable energy is in systems that utilize the solar energy directly.

There are a variety of techniques and different ways to convert sunlight energy into electricity, heat and fuels. Electricity is in many ways a preferable energy form since electricity is relatively easy to transfer over long distances and it can easily be transformed to do work, create motion or heat. One way to convert solar energy directly to electricity is by the means of a technique called photovoltaics.

Photovoltaics, also called solar cells or commonly abbreviated to PV, are electronic devices that convert sunlight directly into direct current electricity. The name photovoltaic originates from a physical process called the photo-

voltaic effect (see section 2.3). The photovoltaic effect was first observed in 1839 by Alexandre Edmond Becquerel who created the world's first solar cell [5]. In this experiment silver chloride was placed in an acidic solution that was connected to platinum electrodes. When the setup was illuminated voltage and current were generated. In the following years of the late 1800s and in the first half of the 1900s some sporadic experiments with different materials were conducted. In 1905 Albert Einstein explains the photoelectric effect on the quantum basis, proposing a simple description of "light quanta", or photons, for the first time in 1921 [6]. Associated with the development of modern semiconductor technology the first practical silicon solar cell, which converted the incoming sunlight energy into electricity with 6 % efficiency, was invented in 1954 by Bell Laboratories [7]. The year after, Bell Laboratories produced the first PV module (see section 2.7), consisting of 432 small silicon solar cells [8]. In the following part of the 1950s and in the 1960s semiconductor based solar cells were started to be used in satellites [8]. It was first in the mid-1970s, after the oil crisis, that the modern era of PV module development started as PV were developed to be used in different applications also on Earth. Particularly, PV were used in consumer electronics and in applications where connection to the electricity grid was too expensive or impossible, such as for boats, mountain huts and telecommunication facilities. The module price at this time was between 20 and 50 US\$/W [8]. In the following two decades research on single-crystalline and later multi-crystalline silicon solar cells and modules drove costs down and improved efficiency, durability and quality. However, it was not until Germany reconstructed their feed-in-tariffs laws in 2000 that a substantial market was created. What Germany did was to promise a fixed purchasing price for 20 years to a producer of renewable electricity, based on the generation costs of the specific technique. These rates were designed to decline annually based on expected cost reductions. Germany's feed-in-tariff scheme was later followed by similar feed-in-tariff schemes or direct capital subsidies programs in other countries, and consequently a global PV market was created. Major PV system cost reductions followed, driven by scale-of-production, better production technologies, technology improvements, stream-lining of installation processes and cheaper cost of capital as the PV market grew and the whole industry got more experienced. Since the mid-70s the learning curve for PV modules has been a price reduction of 20 % each time the world market doubles, as illustrated in Figure 1.1, and the price has dropped from 50 US\$/W to approximately 0.6 US\$/W as of the end 2014 [9]. This price reduction has enabled PV to surpass grid-parity in many countries around the world, i.e. the production cost of PV electricity is lower than the variable part of the end consumer electricity prices, encouraging companies and private persons to reimburse bought electricity with self-produced PV electricity. At the end of 2014 PV accounted for about 1 % of the global electricity demand [10]. However, the global PV market still heavily depends on different governmental subsidies.

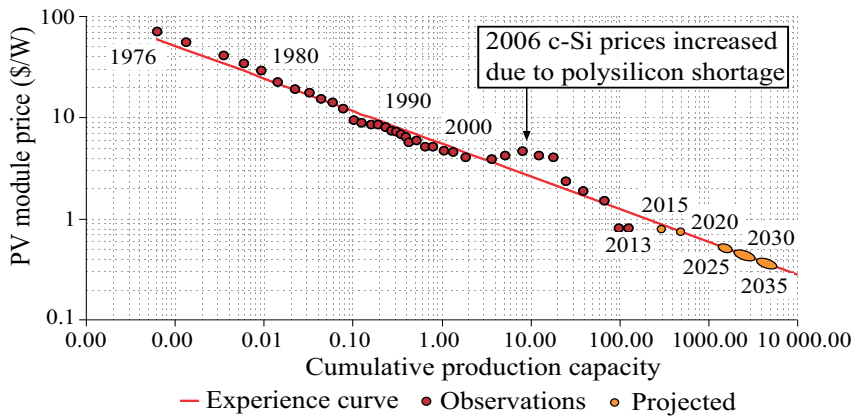


Figure 1.1 PV module price experience curve [9].

To further reduce costs, supplementary technology improvements are necessary. These include light to electricity conversion efficiency improvements, efficient production techniques, utilizing cheaper and abundant materials, reduce material consumption and increasing the life time of PV products. The mono- and multi-crystalline silicon PV techniques currently dominate the PV market. These techniques use wafers of a few hundred micrometers in thickness. A way of reducing material usage is to make solar cells out of semiconductor materials that are better at absorbing light than silicon. These solar cells are generally referred to as thin film solar cells. There currently exist three major thin film technologies that have been commercialized, thin film silicon, CdTe and CIGS. The last two are both named after the compound used in the light absorbing layer in the solar cell. CdTe is based on an absorbing material consisting of cadmium (Cd) and tellurium (Te), while CIGS, or Cu(In,Ga)Se_2 , is based on copper (Cu), indium (In), gallium (Ga) and selenium (Se). These technologies have demonstrated high conversion efficiencies in both commercial production and at lab scale. At the time of writing this thesis the record conversion efficiencies were 21.5 % for CdTe and 21.7 % for CIGS [11]. One drawback with both of the technologies is that they conventionally contain cadmium, which is classified as toxic and carcinogenic [12]. For CdTe, cadmium exists in the crucial light absorber layer and is hard to omit, but for CIGS cadmium is traditionally used in a thin layer called the buffer layer. Development of alternative buffer layer materials is therefore a major topic in the CIGS research. In addition to getting rid of the cadmium, developing buffer layers of alternative materials has also been identified as a possible way to increase the conversion efficiency by reducing parasitic absorption of light in the top most layers of the CIGS solar cell.

The main topic of the papers in this thesis is the investigation of zinc tin oxide, or $\text{Zn}_{1-x}\text{Sn}_x\text{O}_y$ (ZTO), which is a promising material as an alternative buffer layer in CIGS solar cells. The method that is used for depositing ZTO is atomic layer deposition (ALD), where the influence of the ALD process parameters on the ZTO material properties is studied. Furthermore, the thesis includes in-depth investigations on how the material properties of ZTO affect the heterojunction, the energy-band line-up and in the end the output performance CIGS solar cells.

2. Basic concepts of solar cells

2.1 Energy bands in semiconductors

The commercial available PV technologies today, silicon and thin film solar cells, are based on semiconductor materials. Semiconductors are defined by their conductance, which is somewhere between that of metals and insulators.

Semiconductor materials are usually made up of several crystals of the same specific crystal structure. A crystal structure consists of atoms in an ordered periodic arrangement. This order limits the possible energies that the electrons of the atoms can have, since the Pauli principle states that two electrons cannot occupy the same quantum state simultaneously [13]. The quantum states of the atoms generally form overlapping bands of states within the crystal. When there is no available energy, i.e. at 0 K, all electrons within the crystal will occupy the lowest available quantum states up to a certain energy level. This energy level is known as the Fermi level (E_F). Under this condition the highest energy band with occupied states is defined as the valence band (VB) and the highest energy of the occupied states as the valence band maximum (E_V). There are also bands with unoccupied states and the unoccupied band with lowest energy is called the conduction band (CB) and the lowest energy of unoccupied states within the band as the conduction band minimum (E_C). In a semiconductor there is a gap of forbidden energies for the electrons to occupy between the two bands. This gap is the major reason for semiconductors electrical behavior and is called the band gap or band gap energy (E_g).

There are two different kinds of band gaps, direct band gaps and indirect band gaps. The background is that E_V and E_C are each characterized by a certain momentum-like vector in the Brillouin zone, usually called the k-vector. The band gap is called direct if the k-vectors of E_V and E_C are the same, and if they are different it is called an indirect band gap.

When there is no energy available, i.e. at 0 K, the valence band is filled with electrons and there is no free quantum state that an electron can move to. Thus, no current can flow as no charge carrier can move. If an electron gains enough energy, by e.g. heat, it can cross the band gap. In the case of a direct band gap, this transition only needs enough energy to occur. However, in the

case of an indirect band gap, the electron must also change momentum, which can be received from a phonon.

When an excited electron leaves behind a vacancy in the otherwise full valence band, this vacancy, or lack of one electron, can be seen as an imaginary particle with a positive charge and is called a hole. The excited electron in the conduction band has plenty of free quantum states within a small energy interval and can now move through the semiconductor material due to the presence of states extending through the material. However, in order for excited electrons to move these extending states can only be partially filled. The same applies to electrons in the valence band that can move to the holes the excited electron left behind. However, it is usually easier to look at the movement in the valence band as the movement of the imaginary positively charged holes, which use a reversed energy scale, than the movement of numerous electrons. To summarize, if energy is available some electron-hole-pairs will be created and the excited electrons in the conduction band and the holes in the valence band can move through the semiconductor, meaning that current can flow.

The solar cell absorber material that is treated in this thesis is CIGS, which is in detail described section 3.1.3, and has a direct band gap.

2.2 Recombination mechanisms

An electron that has been excited up to the conduction band is in a metastable state and has a certain probability to loose part of its energy to crystal vibrations, other electrons or to light emission through photons as it is transferred to an empty state with a lower energy. One such process is the relaxation of an excited electron from the conduction band down to the valence band. In this process the electron must move into an empty valence band state, thus filling a hole. This process is called recombination. There are three basic types of recombination; radiative recombination, Shockley-Read-Hall (SRH) recombination and Auger recombination. The dominant recombination in CIGS solar cells is SRH recombination. In SRH recombination the electron is relaxed through energy states within the band gap, which are introduced by defects in the semiconductor crystal [14]. These energy states are called deep-level traps and can absorb differences in momentum between carriers. SRH recombination is the dominant recombination process in semiconductor materials that contain defects.

2.3 Photoelectric and photovoltaic effects

In a beam of light the energy of the photons is proportional to the frequency of the light. When light shines on a material, an electron in the material can absorb the energy of one of the photons. If the energy that is transferred from the photon to the electron is higher than the electron binding energy of the material (also called the materials work function), the electron is ejected. All of the photon's energy is absorbed by the electron, so if the photon energy is higher than the work function the excess energy contributes to the free electron's kinetic energy. If the photon energy is lower than the work function, the electron is unable to escape the material. The process when materials emit electrons when light shines upon them is called the photoelectric effect and the ejected electrons are called photoelectrons.

The photovoltaic effect is directly related to the photoelectric effect, but is a different process. Electrons that absorb sufficient energy from incident photons can be excited from the valence band to the conduction band. The excited electron will most likely quickly recombine with the same or another hole (see section 2.2). However, if the excited electrons and the holes are separated they will create an electric current and a voltage difference over the material as they leave behind ionized crystalline atoms. The separation of electrons and holes can be enhanced i.e. by thermal gradients or a built-in potential in the material. The formation of voltage or electric current in a material that it is exposed to photons is called the photovoltaic effect and the PV technology is based on this process.

2.4 The p-n junction

The properties of the semiconductor can be altered by a conscious introduction of impurities in the semiconductor material. This is called doping the material. One type of doping is to introduce impurity atoms, called acceptors, which introduce unoccupied energy states in the valence band. This will create an excess of holes in the material and this kind of doping and material is called p-type. Similarly, the other type of doping is to introduce impurity atoms, called donors, which have occupied states just below or above the conduction band. These donors will contribute with excess electrons in the conduction band of the material and the doping becomes n-type. In an undoped semiconductor E_F is situated in the middle of the band gap. For n-type semiconductors E_F is situated closer to the E_C for p-type semiconductors closer to the E_V .

An n-type material adjacent to a p-type material is called a p-n junction. In this device an electric field is created across the junction between the two doped regions, as illustrated and described by Figure 2.1. The extension of the field in the region surrounding the junction is called the depletion region, or the space charge region (SCR), and the resulting potential after integrating the field in this region is called the built in potential (V_{bi}) [15]. V_{bi} is dependent on the band gap and the doping in the respective p-type and n-type side of the junction according to:

$$qV_{bi} = E_g - kT * \ln\left(\frac{N_{CB}N_{VB}}{N_A N_D}\right) \quad (1)$$

where q is the electron charge, N_{CB} the effective density of states in the conduction band, N_{VB} the effective density of states in the valence band, N_A the density of acceptors and N_D is the density of donors.

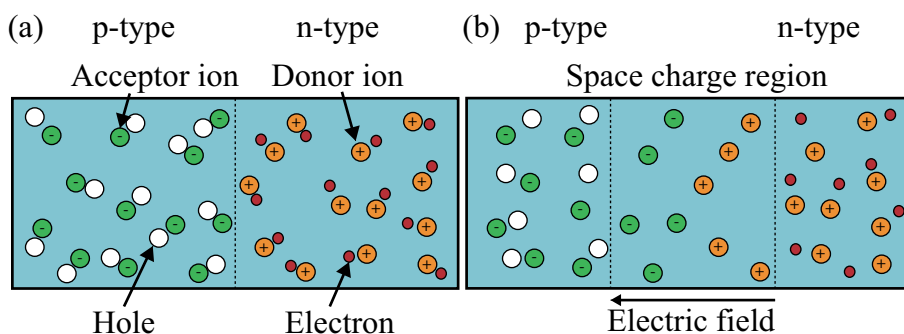


Figure 2.1. (a) A semiconductor material is doped with acceptor atoms on the left side and donor atoms on the right side. As the excess holes and electrons diffuse, the acceptor and donor atoms that are fixed in the crystal structure become ions. (b) When the electrons and holes diffuse over the junction and recombine, an uneven charge distribution is created. This uneven charge distribution gives rise to an electric field that will get stronger as more recombination takes place. However, as the field gets stronger it will counteract the diffusion of the excess holes and electrons, and a steady state occurs with no flow of electrons or holes over the junction at equilibrium.

At a steady-state condition at a given temperature the drift current due to the electric field cancels the diffusion current. Thus, both the electron and hole currents across the junction is zero. For this case the E_F must be constant throughout the sample and V_{bi} is an indirect measure of the band bending required to keep E_F constant at equilibrium.

A p-n junction can be made up of similar semiconductor materials, which have equal band gaps and electron affinities (χ), but different doping, and are then called a homo-junction. If a p-n junction is made up of two different materials with different band gaps and electron affinities, it is called a hetero-junction. Figure 2.2 illustrates the band diagram of a general homo-junction, while Figure 3.2 illustrates the specific band diagram of the hetero-junction CIGS solar cell. A p-n junction connected to two terminals is called a diode device.

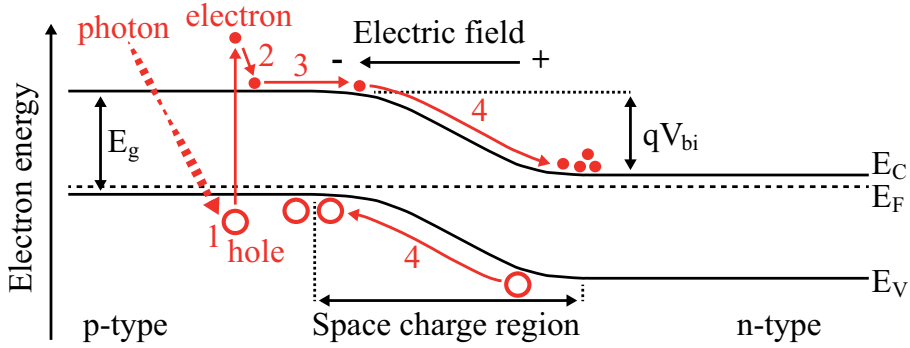


Figure 2.2. The black lines show the energy band diagram of an abrupt p-n homo-junction at thermal equilibrium. The red graphics illustrate the processes of charge separation in a solar cell diode. (1) An incoming photon is absorbed and creates an electron-hole pair as the electron is excited into the conduction band. (2) The excess energy of the excited electron is lost through thermalization as it relaxes down to the conduction band edge. (3) The electron diffuses and enters the space charge region. (4) The electrons and holes that enter the space charge region are affected by the electric field and are separated.

2.5 Charge separation in a solar cell diode

When light shines on a photo-diode, electron-hole pairs are created if the photon energy is sufficient to overcome E_g . If the energy of the photon is higher than E_g the excess energy is usually lost through thermalization as the electron relaxes down to E_C . To be able to collect the energy of the electron-hole-pairs created by photons, the electrons and holes must be separated, since they otherwise sooner or later will recombine (see section 2.2). The separation is done by the introduced built in potential in the p-n junction. The electrons and holes that drift so that they come in contact with the field in the SCR are separated as the field will move the electrons to the n-type side and holes to the p-type side of the p-n junction. This process is illustrated in Figure 2.2.

The gathering of charges on each side of the junction creates a voltage. The charges can then be collected by the terminals in a solar cell diode. When these are connected in a circuit, the electrons from the n-type side will flow through the circuit to the p-type side due to the potential difference. Thus, a direct current (DC) is created, which is fed by the incoming light.

2.6 Current-voltage characteristics

If one consider a diode at a dark steady state condition at room temperature, just a few, by thermal energy exited, electrons in a diode, will be pulled from the p-type material to the n-type by the electric field. The barrier of the electric field will at the same time prevent electrons to move in the opposite direction. Thus, only a very small current will flow through the device. However, if an external potential bias is applied the barrier will be lowered. At some point the barrier will be so low that the many electrons in the conduction band at the n-type side can start to flow across the junction to the p-type side. In the same way, but in the opposite direction, holes from the p-type side will cross the junction to the n-type side. Both these flows will contribute to a large current in the diode at a certain forward bias. This behavior of an ideal diode is described by the diode equation [16]:

$$J = J_0 \left(e^{\frac{qV}{k_B T}} - 1 \right) \quad (2)$$

where J is the current density in the device, J_0 the dark saturation current, V the applied external bias voltage, k_B the Boltzmann constant and T the crystal temperature. J_0 is an parameter that depends on the semiconductor material properties. A diode made of a low quality material with large recombination will have a larger J_0 . Furthermore, J_0 increases as the temperature increases.

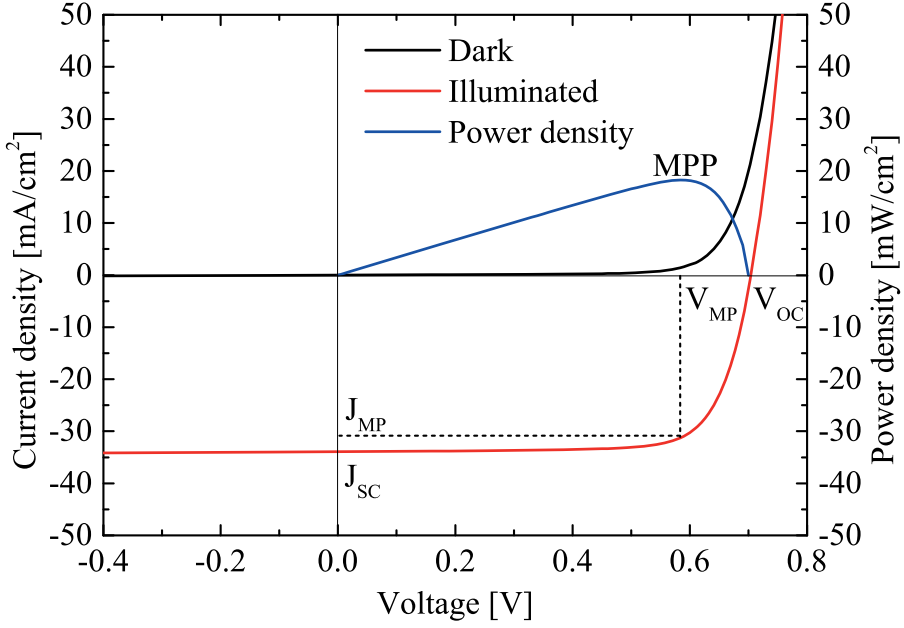


Figure 2.3. Typical current-voltage characteristics of a solar cell under dark and illuminated condition along with the power density produced in the solar cell.

In a solar cell diode that is subjected to illumination, additional current will flow across the junction as the incoming photons create electron-hole pairs that are separated by the electric field. This current is usually called the photocurrent, J_L . Furthermore, most solar cells are not ideal diodes, which make it necessary to add an ideality factor, A , usually ranging between 1-2, to the denominator of the exponent in Equation 2:

$$J = J_0 \left(e^{\frac{qV}{Ak_B T}} - 1 \right) - J_L \quad (3)$$

Equation 3 is the central equation for describing the behavior of a solar cell. A graphical illustration of Equation 3 for a typical solar cell under dark and illuminated conditions is given in Figure 2.3.

In the typical current-voltage (J-V) curve of a solar cell there are some electrical parameters that are of importance when characterizing a solar cell. One of them is the short circuit current (J_{SC}), which is defined as the current that passes through a short circuit connected solar cell when there is no bias applied. J_{SC} is a measure of how many of the photo-excited electrons that reach the contacts. J_{SC} will decrease with increasing E_g , since fewer photons will have enough energy to create electron-hole pairs. Ideally, J_{SC} equals the light induced photocurrent J_L . Another important parameter is the open circuit

voltage (V_{OC}), which is where the forward bias diffusion current equals J_L . Setting J to zero in Equation 3 gives the ideal value:

$$V_{OC} = \frac{Ak_B T}{q} \ln \left(\frac{J_L}{J_0} + 1 \right) \quad (4)$$

Since J_0 depends on the semiconductor material properties, Equation 4 shows that so does V_{OC} . Through J_0 , V_{OC} depend on V_{bi} , and thereby the band gap as Equation 1 shows. So, when J_{SC} decreases, V_{OC} increases with increasing E_g and there is a tradeoff between those two parameters.

An important point in the J-V curve is the maximum power point (MPP) which is the point where the output power $P_{out} = J \times V$ of the solar cell is at its maximum. The current and voltage at this point are defined as J_{MP} and V_{MP} , respectively. The measure of how close the product $J_{SC} \times V_{OC}$ is to MPP is another important parameter and is called the fill factor (FF). This parameter is defined as:

$$FF = \frac{V_{MP} J_{MP}}{V_{OC} J_{SC}} \quad (5)$$

The FF is affected by the total series resistance (R_S) in the solar cell. Furthermore, it is also influenced by electrical paths that bypass the p-n junction, which is gathered in the shunt conductance (G_{SH}) parameter. Including these parameters into Equation 3 results in:

$$J = J_0 \left(e^{\frac{q(V - JR_S)}{Ak_B T}} - 1 \right) + G_{SH}(V - JR_S) - J_L \quad (6)$$

The sole purpose of a solar cell is to convert the incoming power of the light to electric power. The ability to do this is defined by the conversion efficiency (η), which is the ratio between the incoming power (P_{in}) of the light and the output power, P_{out} , of the solar cell. The relation between the other parameters of the solar cell and η can be written as:

$$\eta = \frac{V_{OC} J_{SC} FF}{P_{in}} \quad (7)$$

2.7 The solar cell module

The current that a solar cell will produce at a certain illumination is decided by the quality of the device and the area of the cell. The output voltage of a solar cell is determined, as Equation 4 demonstrates, by the properties of the semiconductor. In a silicon solar cell the upper limit for V_{OC} is about 700 mV [17]. This voltage is too low for practical applications, as it would entail huge losses in regular cables. To increase the voltage, solar cells can be series connected by linking the back contact of one cell to the front contact of an adjacent cell. Generally, the output voltage of a string of series connected cells is the sum of the voltages of the individual cells. In a similar way, parallel connected cells will add up the current. A device that consists of a number of cells that are series and/or parallel connected to provide a desired power capability is called a module. Another function of a commercial module is to encapsulate the cells to protect them from weather or mechanical induced degradations and stresses. Furthermore, modules can be series and/or parallel connected to increase the output voltage or current of a system. The in-depth properties and physics of modules and systems lie outside the scope of this thesis and the reader is referred to textbooks for further information.

3. The Cu(In,Ga)Se₂ solar cell

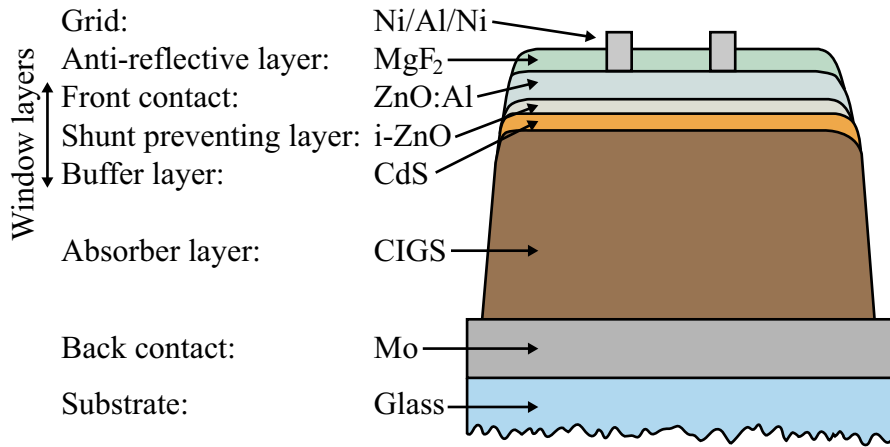


Figure 3.1. Schematic view of the layers in a typical CIGS solar cell. This specific stack of layers is used as the reference CIGS solar cells in this thesis.

3.1 The CIGS solar cell stack

A CIGS solar cell consists of a hetero p-n junction and is typically made up of a substrate and the six layers illustrated in Figure 3.1. The hetero p-n junction is formed between the p-doped absorber and the n-doped layers in the window layer stack. Figure 3.2 demonstrates the band diagram of a typical CIGS solar cell, where the major part of the band bending takes place in the absorber. The absorber is therefore usually divided into the space charge region and the quasi-neutral region (QNR) that lacks an electric field.

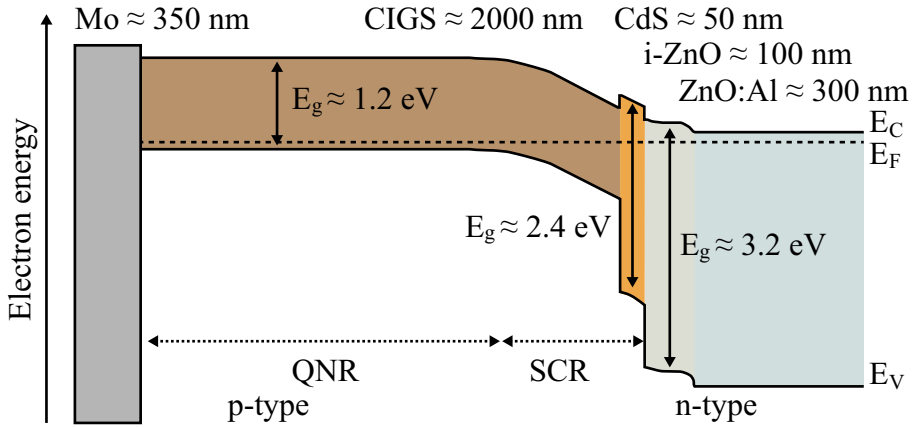


Figure 3.2. Schematic band diagram of a typical complete CIGS solar cell at equilibrium.

Table 3.1. Summary of the different layers and the deposition methods used for fabrication of solar cells in the papers in this thesis.

Layer	Deposition method	Used in paper	Typical thickness [nm]	Typical sheet resistance [Ω/square]
Mo back contact	DC sputtering	I, III, V, VI	350	0.6
CIGS absorber	In house in-line co-evaporation	I, III	1700	
	One stage batch co-evaporation	V	2000	
	In-line co-evaporation at Solibro Research	VI	2000	
CdS buffer layer	Chemical bath deposition	I, III, V, VI	50	
ZTO buffer layer	Atomic layer deposition	I, II, III, IV, V, VI	15 (varied)	
i-ZnO	RF-sputtering	I, III, V, VI	90	
ZnO:Al front contact	RF-sputtering	I, III, V, VI	350 (225) ¹	30
In ₂ O ₃ front contact	Atomic layer deposition	VI	205	30
Ni/Al/Ni grid	Evaporation	I, III, V, VI	3000	0.015
AR coating	Evaporation	I, III, V, VI	105	

¹ The baseline process was developed and improved between paper V and VI. The value within the brackets are for the ZnO:Al layers in paper VI.

Paper I gives an extensive summary of the Ångström Solar Center (ASC) baseline for producing thin film CIGS solar cells. Most of the processes described in paper I are used throughout this thesis and are shortly discussed below. However, the CIGS used in the different papers are coming from different sources. The CIGS layers used in paper I and III are produced in an in-house inline co-evaporator and the process and properties of the CIGS are shortly described below. For paper V an in-house batch reactor with open-boat Cu, In and Ga sources is used and the CIGS in paper VI is deposited by an inline co-evaporation process at Solibro Research AB. Table 3.1 summarizes the different deposition methods used in this thesis.

3.1.1 Substrate

For CIGS solar cells several different kinds of substrates are used, such as glass, flexible steel or different types of plastics [18][19]. Soda-lime glass is the most common substrate and has so far yielded the highest efficiencies [20]. In addition to giving mechanical support to the rest of the solar cell stack, soda lime glass provides Na atoms that are proven to improve the growth of the absorber layer and the performance of solar cells [19].

The substrates used in the ASC baseline are made from low iron soda-lime glass (SLG). They are either $12.5\text{ cm} \times 12.5\text{ cm}$ (2 mm thick) or $10\text{ cm} \times 10\text{ cm}$ (1 mm thick). The substrates are submitted to a cleaning process before the deposition of the molybdenum back contact.

3.1.2 Back contact

As a conducting back contact, a thin layer of polycrystalline Mo is normally used. This layer is deposited by DC magnetron sputtering [21][22]. The preferred contact resistivity value is $\leq 0.3\text{ }\Omega\text{cm}$ [22]. The thickness is decided by the resistance requirements and the ability of the Mo to let through Na. The thickness therefore varies between different research groups.

The molybdenum back contact layer in the ASC baseline is deposited in a vertical inline DC sputtering system where the substrates pass in front of the target with a speed of 7 cm/min. The sputtering pressure and power is 0.8 Pa and 1500 W, respectively, and the resulting Mo layers have a sheet resistance of $0.6 \pm 0.1\text{ }\Omega/\text{square}$ and a thickness of 350 nm.

3.1.3 CIGS absorber

The material responsible for absorbing the light in CIGS solar cells is made up of the elements Cu, In, Ga and Se. CIGS is a p-type (doped by defects) compound semiconductor and a mixture of the parent compounds CuInSe_2

and CuGaSe₂. Both these compounds have a chalcopyrite crystal structure and the E_g are 1.02 eV for pure CuInSe₂ [23] and 1.68 eV for pure [24]. In the lattice structure In and Ga are situated at the same lattice sites, which makes it possible to tune the E_g in CIGS by changing the $[Ga]/([In]+[Ga])$ ratio. To calculate the bandgap of the CuIn_{1-x}Ga_xSe₂, the empirical expression

$$E_g = 1.010 + 0.626x - 0.167x(1 - x) \quad (8)$$

where x is the $[Ga]/([In]+[Ga])$ ratio, can be used [25].

The quality of CIGS as an absorber in solar cells also depends on the $[Cu]/([In]+[Ga])$ ratio. A Cu content above 1.0 improve the grain growth, but conductive Cu_xSe starts to segregate from the film, which increases the shunt conductance and lowers the FF of the solar cell [26]. To get the benefits of the growth of larger grains, but avoid the detrimental Cu_xSe phase, a process with a Cu rich stage followed by a Cu poor stage can be implemented. In high-performance CIGS solar cells the $[Ga]/([In]+[Ga])$ ratios are typically 0.2 to 0.3 and the $[Cu]/([In]+[Ga])$ ratios between 0.7-1.0 [21].

Depending on the incoming radiation, optimum band gaps can be calculated as Shockley and Queisser did for black body radiation [27]. Due to the absorption of light with specific wavelengths in the atmosphere (see Figure 4.1) there exist two E_g values that yield efficiency maximums if the radiation of the AM1.5 spectrum (see section 4.1) is evaluated. One at an absorber E_g of 1.15 eV, which yields a theoretical maximum conversion efficiency of 32.8 %, and a second at an absorber E_g of 1.35 eV, which yields 33.0 % [28]. Furthermore, the $[Ga]/([In]+[Ga])$ ratio can be graded through the depth profile of the CIGS absorber. This makes it possible to increase E_g at the top and bottom interfaces of the CIGS layer, which has the positive effects that the recombination current is decreased, while maintaining an E_g in the middle of the absorber layer that is fit for absorption and collection [29]. So far the best devices have been made with graded CIGS that have the lowest E_g close to the 1.15 eV maximum [20][30][31]. However, in this thesis CIGS with linear gradients are exclusively used.

The CIGS absorber layer can be deposited by a number of different deposition methods, such as co-evaporation, sputtering, sputtering of metallic layers followed by selenization, electrodeposition followed by selenization, electro spray deposition etc. [18]. The most common method in research is thermal co-evaporation, which has been used to produce the devices with the highest efficiencies [20].

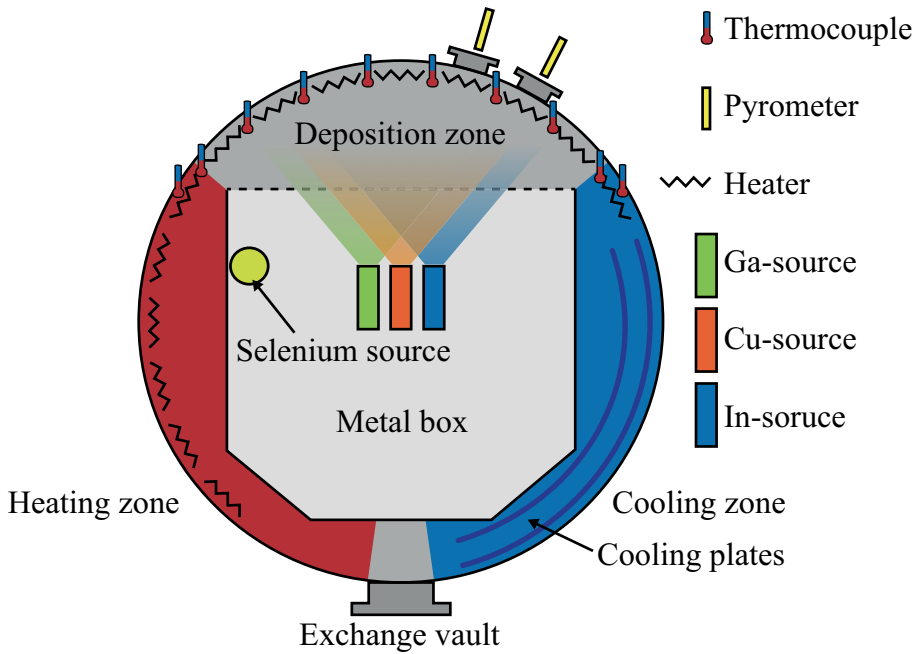


Figure 3.3. Schematic illustration of the ÅSC in-line co-evaporation system.

Paper I in this thesis gives a complete review of the in-house in-line co-evaporation system and the resulting CIGS. The in-house batch reactor with open-boat Cu, In and Ga sources used in paper V is described in [32][33], while the CIGS in paper VI is supplied from Solibro Research AB.

Figure 3.3 shows a schematic illustration of the in-house in-line co-evaporation system. In this system the substrates are mounted into 24 vertical metal frames that are loaded facing inwards onto a carousel inside the deposition chamber. The three single metal sources are controlled with an accuracy better than ± 1 °C and are situated in the middle facing outwards in the order, gallium, copper, and indium. Selenium is evaporated in excess from a source placed at the bottom of the evaporation system. The substrates on the carousel move sequentially through a heating zone, a deposition zone and a cooling zone. Quartz halogen lamps are used in the heating and deposition zones to heat the substrates from the backside to 520 °C. One full round for the carousel takes 60 min, whereof the substrates spend 17.5 min in the deposition zone. Usually, the rotation speed is increased after a sample has passed the deposition zone by a factor of 2 to avoid elemental selenium condensing on the CIGS surface.

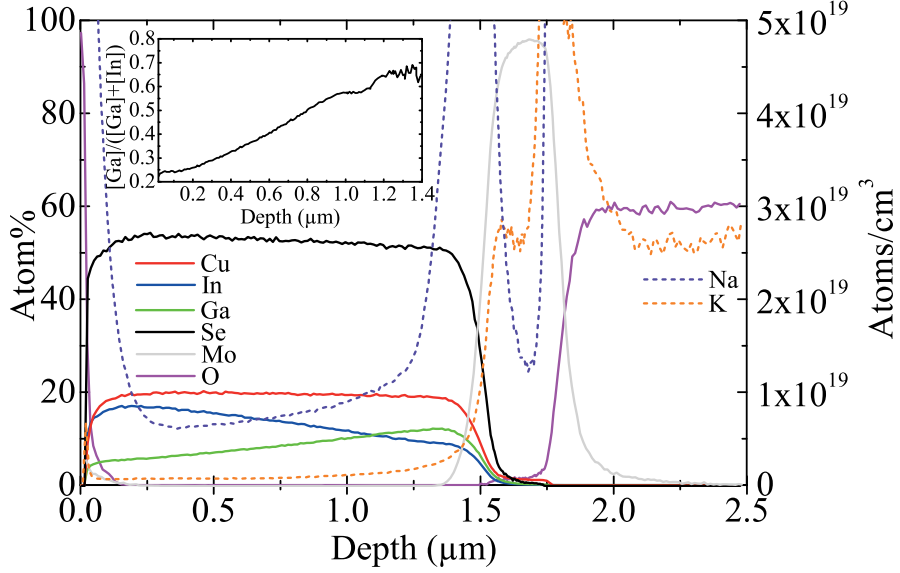


Figure 3.4. Concentration depth profile over a baseline device from the CIGS layer down to the glass substrate measured by SIMS. Cu, In, Ga, Se, Mo, and O are measured in atom percentage on the left axis, whereas Na and K are measured in atoms/cm³ on the right axis. The inset shows the $[Ga]/([In]+[Ga])$ ratio as a function of depth.

The drift in CIGS composition from sample to sample and from run to run is very small in the ÅSC in-line co-evaporation system. With constant source temperatures and similar source filling heights, XRF measurements demonstrate that the $[Cu]/([In]+[Ga])$ ratio of the standard process recipe is 0.90 and the $[Ga]/([In]+[Ga])$ ratio is 0.45, with run to run $[Ga]/([In]+[Ga])$ and $[Cu]/([In]+[Ga])$ variations less than 0.05 on identical positions on each sample. The typical layer thickness is approximately 1700 ± 300 nm, between runs, but varies much less within a run. The thickness, $[Cu]/([In]+[Ga])$ and $[Ga]/([In]+[Ga])$ variations over a single sample are all less than 5%.

The alignment of the metal sources and the sequential nature of the deposition process results in an almost linear Ga gradient through the thickness of the layer, as the SIMS (see the appendix) measurement in Figure 3.4 demonstrates. The $[Ga]/([In]+[Ga])$ ratio increases from 0.25 at the front to 0.65 towards the back contact, which by using equation (8) results in E_g values of 1.14 and 1.38 eV, respectively. This gradient forms a back-surface field, which causes electrons to move away from the back contact and thereby reduces the probability of recombination at the contact [34].

3.1.4 The window layer stack

In order to form a p-n junction an n-type material is needed on top of the p-type CIGS absorber. In CIGS solar cells this n-type material is actually made of three layers, collectively called the window layer stack. In a CIGS solar cell the collection of photo-generated carriers from the absorber is what contributes to the current, while almost all carriers generated in the window layer stack are lost. The window layers therefore need to be as transparent as possible, hence the name ‘window layers’. The layer closest to the absorber is the buffer layer, traditionally made of cadmium sulfide, CdS, but several other materials are used as well [35][36]. The topic of buffer layers is an essential part of this thesis and is further discussed in section 3.2.

The other layers in the window layer stack are a transparent conducting oxide (TCO), as a front contact, and occasionally a shunt preventing layer in between the front contact and the buffer layer.

3.1.5 Shunt preventing layer

For some buffer layer and front contact designs a highly resistive layer is needed in-between those two layers to improve device performance. This layer, usually made of ~50 nm intrinsic zinc oxide (i-ZnO), reduces the influence of shunt currents in the CIGS and electrical inhomogeneities over the device area [37][38]. The i-ZnO layer is usually needed in the traditional window layer stack with the CdS buffer layer and the aluminum doped zinc oxide (ZnO:Al) front contact, but it has been found that it can be beneficial to omit it when other alternative buffer layers are used [35].

In the ÅSC CIGS solar cell baseline, cells with the CdS buffer layer also include an i-ZnO layer with a typical thickness of 90 ± 10 nm. This i-ZnO layer is deposited by radio frequency (RF) sputtering at a power of 200 W using a target with a purity of 99.9 %.

3.1.6 Front contact

It is of high importance that the front contact has high E_g and a high transmittance throughout the wavelength region of the absorber band gap so that the photons are collected in the absorber layer. Furthermore, high lateral conductivity is also needed to reduce resistive losses. There is somewhat a tradeoff between these two requirements. The conductivity mainly depends on the free charge carrier density and the mobility. However, free charge carriers can absorb some of the energy in long wavelength light and therefore reduce the yield of the solar cell. It is therefore important that the front contact material has a high mobility and a low free charge carrier density. The thickness of the front contact depends on the design of the device. Due

to the tradeoff, a thicker front contact will have a higher conductivity and therefore lower R_S associated losses and higher FF , but absorb more of the incoming light and therefore some losses in J_{SC} . Thicker front contact layers are usually used for modules as compared to single cells, since modules need to handle higher currents than single cells. Typically, modules may require a sheet resistance of (R_{SH}) 5–10 Ω/square , while 20–30 Ω/square is enough for small area cells [21].

The standard front contact in the ÅSC baseline is ZnO:Al. The front contact is deposited subsequently after the i-ZnO layer in the same sputtering system. For the front contact, a sputtering power of 300 W and a ZnO:Al target containing 2 % by weight of Al_2O_3 is used. The resulting layer has a thickness of 350 ± 20 nm and a sheet resistance of 30 ± 10 Ω/square .

3.1.7 Grid

For laboratory test cells, where interconnection between individual cells is lacking, the front TCO needs to be contacted in order to measure the cell. It is common to deposit a metal contact on top of the TCO to provide a contact pad for the current density vs. voltage characterization (see section 4.1). This metal front contact also has the benefit of reducing the resistive losses in the cell, which leads to that the TCO can be thinned down. The drawback of the grid is that it shadows a part of the solar cell. Thus, the grid needs to be carefully designed.

At ÅSC a Ni/Al/Ni stack is used as the front contact. It is deposited by evaporation where an aperture mask is used to define the grid pattern. The function of the first thin Ni layer is to prevent the aluminum to react with oxygen from the front contact and form a high resistive oxide layer. The second Ni layer prevents in the same way Al to react with air. The second Ni layer also facilitates an ohmic contact between the grid and the measuring probe. The total grid thickness of the grid is 3000 ± 500 nm. None-structured Ni/Al/Ni layers with this thickness deposited on glass substrates have sheet resistances between 0.01 and 0.02 Ω/square .

3.1.8 Anti-reflective coating

An antireflective (AR) coating can be deposited on top of the finished cells in order to reduce the reflection of the incoming light in the surface and interfaces in the window layer stack. Using an anti-reflective coating is especially important when evaluating alternations in the window layer stack since modifications in layer thickness, density, composition, etc. change the optical properties of the window layers. This can change the optical interference fringes at different wavelengths, which can be seen in quantum efficiency measurements (see section 4.2). The match of the interference fringes in the window layer stack with the AM1.5 light spectrum (see section 4.1) can be better or worse, which affects the current in the solar cell. Besides reducing the overall reflection, an AR coating reduces these interference effects. However, using an AR coating in a commercial module is not practical since a cover glass is typically required, so it is mainly a tool for research purpose.

For the analysis of cells in this thesis, an AR coating of MgF_2 is used. To optimize the performance, the thickness of the AR coating is 105 ± 5 nm and it is evaporated from a resistively heated baffled box source. Due to mainly an increase in J_{SC} , the AR coating typically increases the conversion efficiency of the cells with 1 % (absolute).

3.1.9 Scribing

Out of a large area of the CIGS solar cell stack single solar cells are needed to be defined. This is done by removing the layers on top of the Mo outside the cell area by mechanical scribing or laser patterning. The recommend standard size for solar cell measurement is a cell area of 1 cm^2 , but many labs routinely use cells in the order of about 0.5 cm^2 . At ÅSC the baseline procedure involves mechanical scribing of 0.5 cm^2 cells with a stylus.

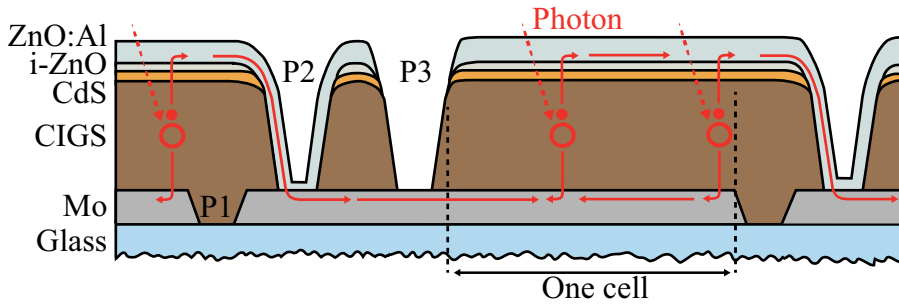


Figure 3.5. Schematic illustration of the CIGS module pattern. The red illustrates the processes of charge separation and the flow of the photocurrent.

Mini-modules with ten series connected cells are made in paper I. In order to make a module, the individual cells need to be series interconnected. This is done by first patterning the Mo back-contact layer into individual cells. This step is commonly called P1 and is at ÅSC done by direct induced laser ablation through the glass substrate using a pulsed laser. The patterned substrate is then covered with CIGS and a buffer layer. After deposition of the i-ZnO layer, the process sequence is interrupted for the second, P2, patterning step. Adjacent to the P1 lines a trench down to the Mo back contact is opened. At ÅSC this is done by mechanical scribing with a stylus. This trench is filled as the ZnO:Al front contact is deposited, resulting in a direct contact between the front and the back contacts. Finally, a third patterning step, P3, removes the whole stack of deposited layers down to the Mo back contact adjacent to the P2 lines. This provides electrical isolation of the front contacts of neighboring cells. P3 is at ÅSC made with the same stylus as the P2 scribe line. Figure 3.5 schematically illustrates a monolithically integrated CIGS module with the movement of photo-generated electron-hole indicated.

3.2 Buffer layer engineering theory

The role of the buffer layer is to ensure good interfacial properties between the CIGS absorber and the shunt preventing layer and the front contact. This includes several aspects which are discussed in this section.

3.2.1 Recombination paths in Cu(In,Ga)Se₂ solar cells

The dominating recombination process in CIGS solar cells is SRH recombination (see section 2.2) since the semiconductor materials in the solar cell stack contains relatively many defects. One important issue when developing highly efficient CIGS solar cells is to minimize the recombination, as it limits V_{OC} . There are a few different recombination paths that can dominate in a device. It is either recombination currents in the space-charge or neutral regions of the absorber layer or at any of the critical interfaces, including the absorber/buffer layer interface or absorber/back contact. These recombination paths are schematically illustrated in Figure 3.6, with the exception of the absorber/back contact path.

Recombination in the absorber depends on absorber material parameters, such as defect deep trap states in the band gap, grain size, doping density and the diffusion length for electrons [39]. The recombination is usually higher in the SCR than in the QNR since there are a comparable amount of electrons and holes in the SCR. The variation in the ideality factor A between 1 and 2 depends on the energies of the deep traps and as they move towards the band edges, $A \rightarrow 1$.

The recombination at the absorber/back contact interface is usually very small as long as the absorber thickness is larger than the minority-carrier diffusion length. A graded absorber that creates a back surface field decreases the absorber/back contact recombination even further [21].

The absorber/buffer layer interface recombination depends on the defect density at the interface, the interface recombination barrier (Φ_b) and the conduction band line-up (see section 3.2.1). The different recombination paths are effectively connected in parallel and V_{OC} will therefore be limited by one dominant recombination current [21]. A way of determining the dominant recombination path is to perform a V_{OC} vs. temperature measurement (see section 4.3).

3.2.2 Inversion of the absorber close to the junction

A heterojunction solar cell may, in contrast to a homojunction solar cell, contain a high density of states at the interfaces due to defects. The highest recombination takes place when the electron density equals the hole density,

i.e. when E_F is situated in the middle of the band gap [40]. One therefore wants to avoid having this E_F position at an interface due to the higher density of states there that leads to enhanced recombination. By an asymmetric doping this E_F position can be moved into the bulk of the CIGS, which is beneficial for the performance of the solar cell since there usually is a lower density of states in the bulk than at an interface. This is called inversion and is basically when the band bending positions the CB of the p-type absorber close to E_F near the junction, which is the opposite situation than in the QNR where the VB on a p-type material is much closer to E_F . Figure 3.6 illustrates a band diagram where inversion of the absorber takes place. The doping of the buffer layer along with the other window layer properties contributes to the inversion of the CIGS absorber.

3.2.3 Buffer layer band line-up

The energy band alignment between the different layers in a CIGS solar cell strongly affects the performance and the absence of a buffer layer usually results in a low V_{OC} [41]. The reason is mainly the unfavorable conduction band line up that is formed between CIGS and ZnO, which leads to a higher interface recombination (see section 3.2.1). Figure 3.6 illustrates two different conduction band line-ups that can occur in a heterojunction CIGS solar cell. Figure 3.6 (a) demonstrates a situation where the conduction band energy of the buffer layer (E_C^{buffer}) is lower than the conduction band energy of the absorber ($E_C^{absorber}$), which leads to a negative conduction band offset energy (ΔE_C) as $\Delta E_C = E_C^{buffer} - E_C^{absorber}$. This situation is called a negative conduction band offset (CBO), which commonly is referred to as a cliff. A cliff is undesirable since it reduces the inversion close to the interface and leads to increased recombination via interface states, and thereby losses in V_{OC} and FF [42][40][43]. Between CIGS and ZnO a cliff is formed [41] and this is a major reason why a buffer layer is needed for high efficient CIGS solar cells.

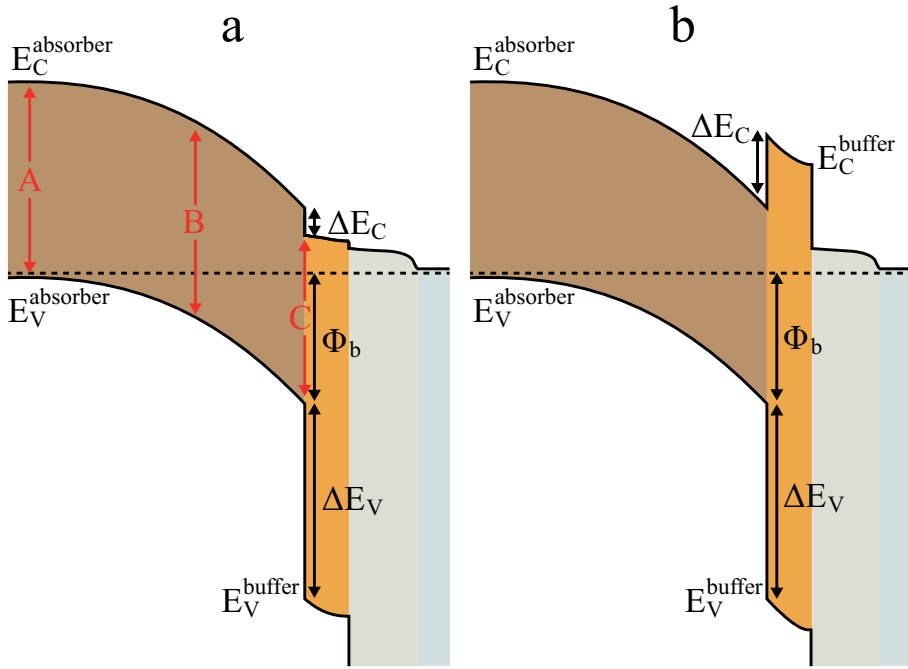


Figure 3.6. Band alignments at the interface between the absorber and two different buffer layers. (a) Illustrates a cliff like conduction band offset where the conduction band offset energy (ΔE_C) is negative. (b) Illustrates a spike like conduction band offset where the ΔE_C is positive. Φ_b indicates the potential barrier for interface recombination and the red arrows in figure (a) demonstrates the different recombination paths that are discussed in section 3.2.1. These are (A) recombination in the QNR of the absorber (B) recombination in the SCR of the absorber and (C) recombination through defect states at the absorber/buffer interface.

The opposite situation, illustrated in Figure 3.6 (b), is when $\Delta E_C = E_C^{buffer} - E_C^{absorber} > 0$. This positive CBO is commonly referred to as a spike. A large spike may lead to a barrier that, under forward bias conditions, blocks photo-generated electrons in the absorber from entering the front contact, and therefore has a detrimental effect on J_{SC} and FF [43][44]. However, a moderate spike does not limit current collection and is therefore the desirable conduction band line-up [43]. What kind of CBO that will be formed depends on the E_g and χ of the CIGS at the interface and the E_g and χ of the buffer layer.

3.2.4 Different buffer layers

To summarize, a good buffer layer should have the these properties [35]:

- A sufficiently wide E_g , since absorption of photons in the window layers do not contribute to the photocurrent in a solar cell.
- A suitable conduction band line-up between the absorber and the shunt preventing layer or the front contact.
- A low defect density at the absorber/buffer interface and/or inversion of the absorber surface with a position of the absorber CB close to the E_F .

Traditionally the most used buffer layer in CIGS solar cells is cadmium sulfide, CdS, deposited by chemical bath deposition (CBD). CdS more or less fulfills all the above requirements, even if one of the drawbacks of the CdS as a buffer layer is that it has a relative low optical band gap, $E_g \approx 2.4\text{-}2.5$ eV [45], which absorbs some high energy photons in the 350-550 nm part of the sunlight spectrum. This absorption ultimately leads to lower current output. The deposition method of CBD is from an industrial point of view another drawback since it usually is the only liquid based process in a processing line with otherwise solely vacuum based deposition methods. Handling the chemical waste of the CBD process is problematic since Cd is classified as toxic and carcinogenic [12] and several regions in the world have statutory limitations of the usage of Cd in products.

Due to drawbacks of the low bandgap and the deposition process from an industrial point of view, alternative buffer layers have become a major topic within CIGS research. Different wide bandgap materials, such as Zn(O,S), In_2S_3 , $\text{Zn}_{1-x}\text{Mg}_x\text{O}$ and $\text{Zn}_{1-x}\text{Sn}_x\text{O}_y$ (the latter is the main topic of this thesis) and deposition methods has been proposed, and are extensively reviewed in [35][36]. All these buffer layers have in common, regardless of the deposition technique, that they increase the J_{SC} of cells when they replace CdS. However, cells with an alternative buffer layer usually end up with a lower V_{OC} and FF compared to CdS reference cells [35]. Several suggestions for this effect have been proposed, such as a good lattice matching between CdS and CIGS [46], Cd n-doping of the top surface of the CIGS that creates a buried homo-junction [21][47] and an in situ etching effect in the CBD deposition process that removes Cu_xSe phases and the natural oxides from the CIGS surface that are formed directly at air exposure [48]. It is probably a combination of these properties of the CBD deposited CdS that still makes it the state of the art buffer layer that is used in most world record devices, including the latest record device that demonstrate a conversion efficiency of 21.7 % [11].

3.2.5 Atomic layer deposition of buffer layers

Atomic layer deposition (ALD) is a chemical vapor deposition technique that utilizes sequential self-terminating gas to solid reactions. The reactants, usually denoted precursors, are pulsed into the reactor separately in a sequential manner, where the gas molecules interact with the substrate due to chemical or physical reactions. The adsorption of molecules on a surface is divided into two general classes, chemisorption and physisorption [49].

In chemisorption the electronic structure of the precursor molecules is changed when new covalent or ionic bonds are formed between the precursor elements/molecules and the elements/molecules at the substrate. A surface contains a limited number of places where the chemical bonding can occur. These places are called reaction sites and they limit the number of adsorbed molecules so that only one layer, a monolayer, of the precursor species is adsorbed. The amount of atoms each precursor pulse adds to a surface in an ideal ALD precursor pulse is decided by two factors; the number of reactive surface sites, which are decided by the surface, and the steric hindrance, which depends on the size of the precursor molecules.

Physisorption is a weaker form of interaction than chemisorption, caused by van der Waals forces, that takes place between a molecule and a surface. In physisorption the precursor molecule typically undergoes minimal changes and the interaction is not specific to a certain element or molecule, i.e. reaction site, which leads to that physisorption of multilayers can occur.

The adsorption of molecules on a surface can be both irreversible and reversible, and depends on the temperature. Irreversible adsorption is necessary for growing a film with a self-terminating ALD process. Figure 3.7 illustrates how different adsorption processes depend on time during ALD pulses of precursors and purging. It is only the adsorption processes in Figure 3.7(a) and (c) that fulfill the ALD requirements of self-terminating irreversible adsorption. In the case of Figure 3.7(c) it is only the dotted line that contributes to the actual growth of the film.

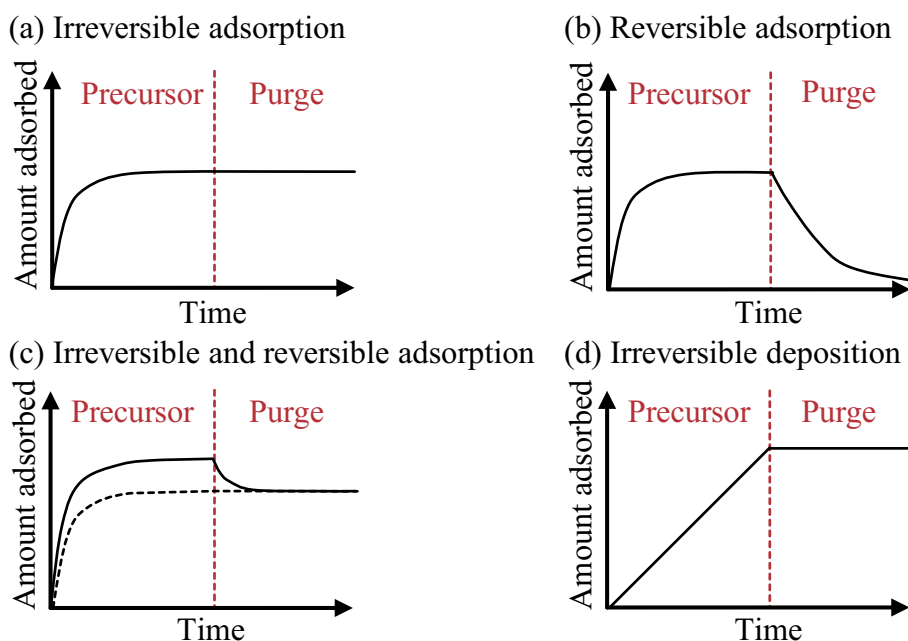


Figure 3.7. Schematic examples of how the amount of adsorbed material varies with time during ALD pulses for different adsorption processes: (a) Irreversible saturating adsorption, i.e. self-terminating reactions, (b) reversible saturating adsorption, i.e. desorption during purge pulses, (c) combined irreversible and reversible saturating adsorption and (d) irreversible non-saturating adsorption, i.e. deposition. The vertical dashed line marks the end of the precursor pulse and the beginning of a purge or evacuation pulse.

In an ideal ALD process the substrate surface is exposed to the precursors one at a time, and if the pulse time is long enough the surface will be saturated by precursor adsorbents. Atoms and molecules that are not incorporated in the film are removed as gaseous reaction byproducts. The film growth is done through the repeated exposure of the individual precursors in a pulsing scheme, where each precursor pulse adds reaction sites for the following precursor. Between the precursor pulses a non-reactive gas is usually purged onto the surface to remove non-reacted precursor molecules and gaseous reaction by-products. The smallest repeating pulse sequence is called an ALD cycle. Figure 3.8 schematically illustrates an ALD cycle for an ALD process for a binary film. The amount of material that is added in each cycle is referred to as growth per cycle. The ALD cycle in Figure 3.8 can then be repeated a set number of times to reach the desired film thickness, where the total amount of ALD cycles depends on the amount of material deposition in each cycle.

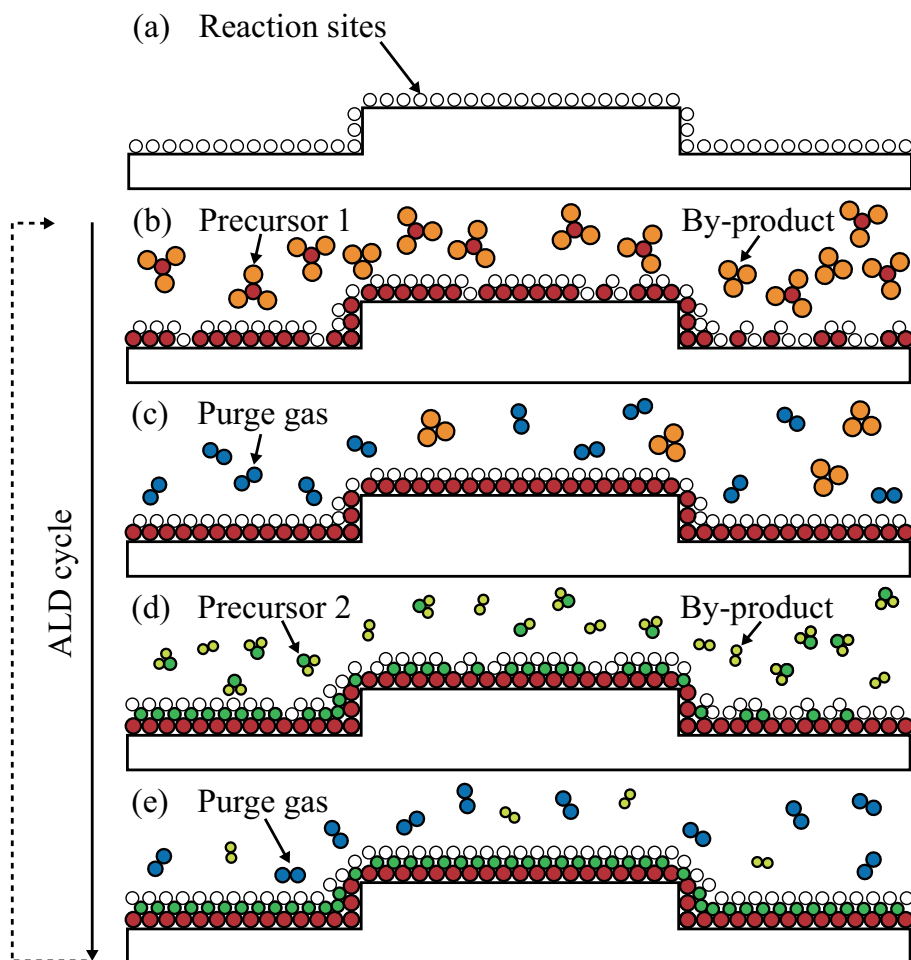


Figure 3.8. Schematic illustration of a typical ALD cycle. (a) The original substrate surface contains a certain number of reaction sites. (b) The substrate is exposed to the first gas-phase precursor, which interact with the reaction sites on the substrate. When no more sites are available for reaction, the film growth stops and the reaction is self-terminated. (c) A non-reactive gas is purged onto the sample to remove the non-reacted precursor molecules and the gaseous reaction by-products. (d) The sample is exposed to a second gas-phase precursor and another self-terminating reaction take place. (e) A second purge step is added to remove excess precursor and by-product molecules.

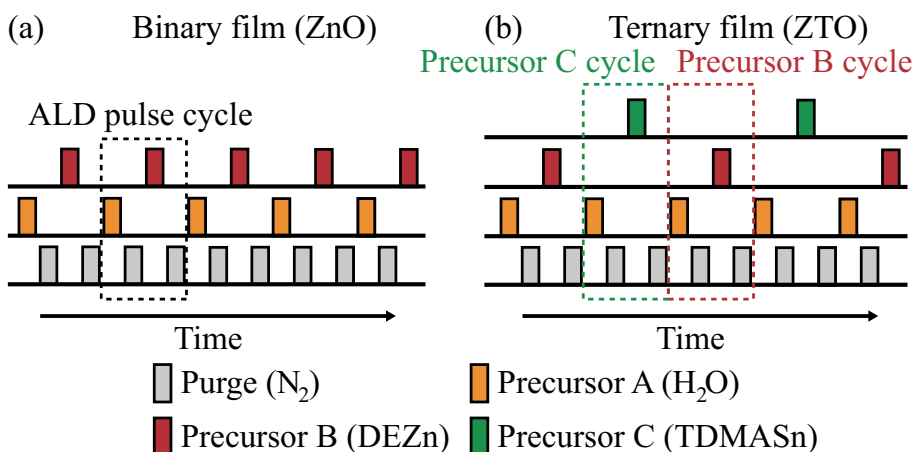


Figure 3.9. (a) Illustration of a typical pulse scheme for a binary film, where ZnO is used as an example. (b) A typical pulse scheme for a ternary film with an equal amount of precursor A and B cycles, where ZTO is used as an example. The precursors that have been used in this thesis (see section 5.1) are stated within the parentheses. The dotted squares indicate one ALD cycle of ZnO and SnO_x, respectively.

Films that contain several elements can also be readily grown by ALD by changing/adding precursors to the pulsing scheme. Figure 3.9(a) illustrates a pulsing scheme for a binary film, where the growth of ZnO used in this thesis is taken as an example. Furthermore, in Figure 3.9(b) the pulsing scheme for ZTO is used as a typical example of the growth of ternary film. The growth of ZTO can be viewed as a mixture of ZnO and SnO_x cycles, where the ratio of ZnO and SnO_x cycles can be used to effectively tune the ZTO film composition.

Since ALD is a surface controlled process, other parameters than the reactants, substrate and temperature usually have little or no influence on the growth. Figure 3.10 shows a schematic representation of the ALD growth rate as a function of temperature and lists different non-self-terminating reactions that can occur at both low and high temperatures. The temperature range in the middle, where the growth reactions fulfill the ALD requirement of self-termination is called the ALD-window. The growth rate within the ALD-window can decrease with increasing temperature, which can be caused by a decrease in the number of reactive sites as the temperature is increased. The growth rate can also be constant with regard to the deposition temperature, which is because steric hindrance causes saturation instead of the number of reactive sites. A third case inside the ALD window can occur if an increase of the temperature leads to that energy barriers for new reactions are exceeded, which will lead to that the growth rate increases with increasing temperature.

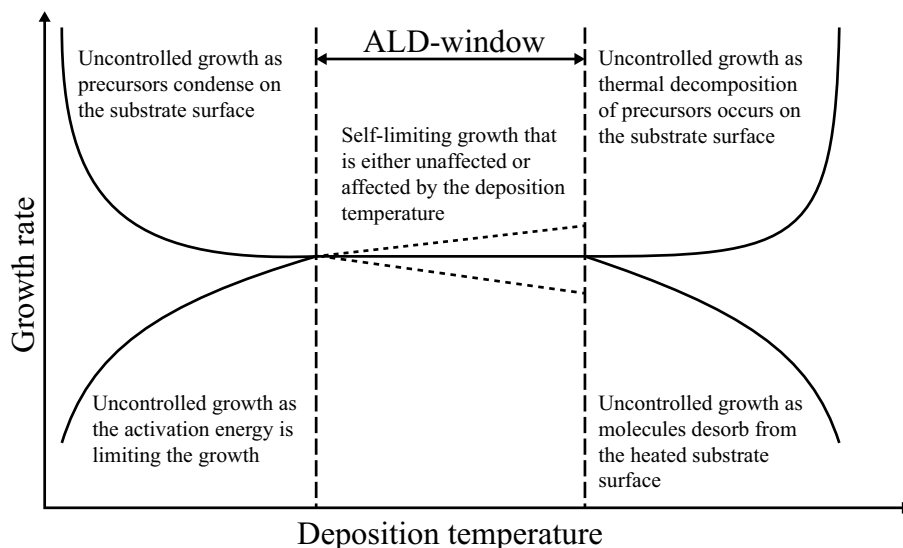


Figure 3.10. A schematic illustration of how the ALD deposition temperature can influence the growth rate.

The influence of the temperature on the growth rate is usually stronger outside of the ALD-window and the growth rate can be either very high or very low at both low as well as at high temperatures due to the different reactions described in Figure 3.10.

Some of the advantages of the ALD method are; high uniformity, good step-coverage of 3D-structures, precise thickness control, low growth temperature (typically 100–350 °C) and the possibility to coat sensitive substrates. Furthermore, for ternary films the possibility to change the ALD cycle fraction to get specific ratios between different precursors leads to an excellent composition control. The main drawbacks are a relatively low growth rate and limitations in process chemistry due to source materials. The characteristics of ALD make it a suitable method for buffer layer deposition in CIGS solar cells. The conformal growth makes it possible to grow thin dense films with low pinhole densities that still completely cover the rough CIGS surface. Alternative buffer layers deposited by ALD have previously been extensively reviewed in [35][50][51]. Moreover, ALD is a dry vacuum process, which is a benefit from a production point of view since it can be integrated in CIGS production lines that usually contain other vacuum processes. The critical issues of the ALD method in industrial production include high-uniformity over large areas, reactant handling and the deposition rates [51]. The deposition rates in conventional single substrate reactors usually are too slow for the high-throughput rates that are needed in conventional PV module manufacturing. This issue can be solved by implementing batch ALD, large area ALD, spatial in-line ALD or roll-to-roll ALD processes [51].

4. Solar cell characterization methods

Characterization and analysis of the electrical performance of solar cells are fundamental in PV research. Table 4.1 summarizes the different methods utilized in this thesis, for what information they have been used to obtain and in which paper they have been implemented. An overview of the techniques is given in the following sections.

Table 4.1. List of electrical characterization methods used in this thesis.

Characterization method:	Abbreviation:	Used to obtain:	In paper:
Current density vs. voltage	J-V	V_{OC} , J_{SC} , FF , η , R_s , G_{SH} , A	I, III, V, VI
Quantum efficiency	QE	Spectral response, J_{SC} , CIGS interface band gap	I, III, V, VI
Open circuit voltage vs. temperature	V_{OC} vs. T	Recombination path	V
Numerical simulations	-	Device band energy levels	V

4.1 Current density vs. voltage

The most fundamental of solar cell characterization techniques is the measurement of cell conversion efficiency by current J-V characterization. To obtain the J-V curve (see Figure 2.3) of a solar cell a variable voltage source is used while the voltage and current at the cell terminals are recorded.

It is essential to have standardized test procedures and conditions so that comparison of devices manufactured by different companies or laboratories can be compared. The standard when measuring the J-V characteristics of solar cells is to do it at a cell temperature of 25 °C, with the air mass 1.5 spectrum (AM1.5) [52] and at an intensity of 1 kW/m². This is usually done with a four-point probe configuration, to eliminate probe contact resistance. Figure 4.1 illustrates the spectrum of extraterrestrial light and the AM1.5 spectrum.

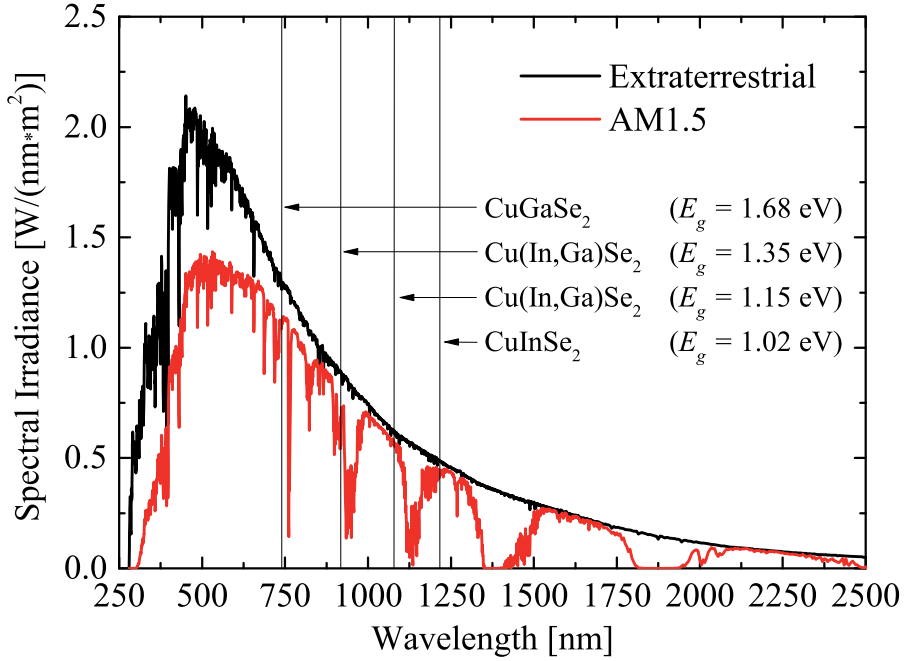


Figure 4.1. Solar irradiance for extraterrestrial radiation (black) and the AM1.5 spectrum (red). The E_g of the parent compositions CuGaSe₂ and CuInSe₂ along with the two E_g values of CIGS that would yield theoretical maximum values are indicated in the figure (see section 3.1).

Practically, the measurements are usually done in solar simulators that are made to reproduce the AM 1.5 solar spectrum in the best possible way. For the papers in this thesis two different solar simulators are used; a tungsten halogen lamp and an ORIEL Sol2A solar simulator from Newport Stratford Inc. Both simulators are calibrated to give an intensity corresponding to the photon flux at 1 kW/m² with a certified silicon photo diode from Hamamatsu Photonics. The spectrums of the two solar simulators are not exactly matching the AM1.5 spectrum, so to obtain accurate current values external quantum efficiency measurements can be used to calculate a correct J_{SC} value.

From the measured J–V data, other solar cell parameters such as R_s , G_{SH} and A of a device are extracted by using an evaluation method suggested in [53].

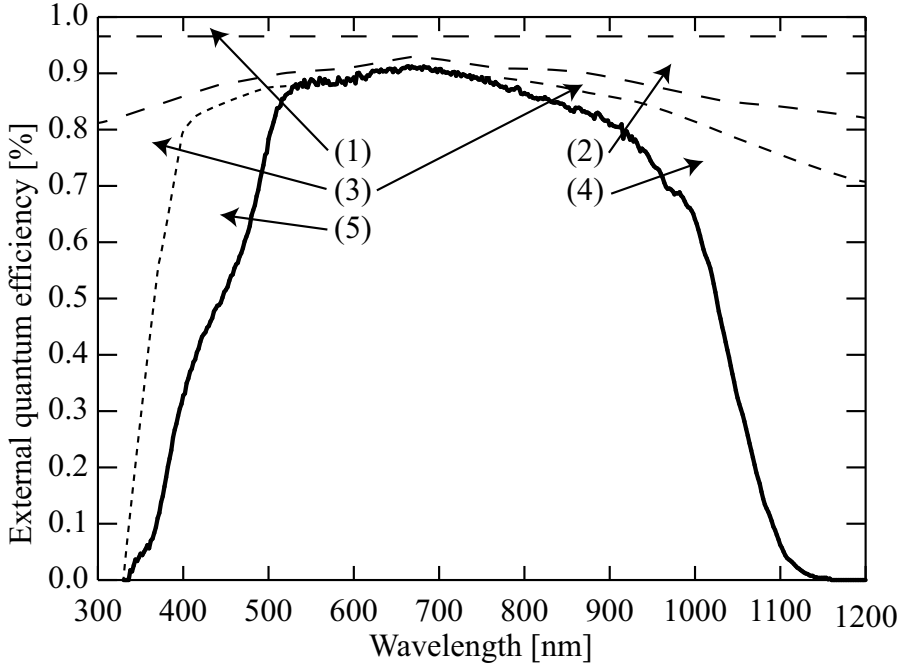


Figure 4.2. External quantum efficiency (solid line) and optical loss mechanisms for a typical CIGS solar cell. The losses are; (1) shading from the grid, (2) reflection from the Cu(In,Ga)Se₂/CdS/ZnO layers, (3) absorption in the ZnO layers, (4) insufficient absorption and collection, (5) absorption in CdS buffer layer.

4.2 Quantum efficiency

The spectral response of a solar cell can be determined by quantum efficiency (QE) measurements. The quantum efficiency is a measure of the solar cells ability to convert light of a specific wavelength into current. The obtained value is the ratio of the number of charge carriers collected to the number of photons in the incoming light. There are two different types of quantum efficiencies used for solar cell characterization, external quantum efficiency (EQE) and internal quantum efficiency (IQE). EQE compares the collected charge carriers with all the photons that strike the solar cell. IQE on the other hand compares the collected charge carriers with the photons that are absorbed by the solar cell, i.e. the reflectance of the cell is deducted. IQE is therefore always higher than EQE.

The current that the solar cell produces when exposed to sunlight, i.e. J_{SC} , can be determined by integrating the EQE over the whole solar AM1.5 spectrum. Furthermore, from EQE measurements the effective optical band gaps of the different layers in the solar cell stack can be obtained, along with opti-

cal losses in the window layer stack and generation losses in the absorber. The method is therefore used to determine the losses that are reducing J_{SC} from the maximum achievable photocurrent. Figure 4.2 illustrates a typical EQE curve of a typical CIGS solar cell. In Figure 4.2 also point out the different losses in a typical CIGS solar cell. An in-house built system, similar to the measurement setup presented in [54], is used for the EQE measurements in this thesis.

4.3 Open circuit voltage vs. temperature

A useful tool when analyzing the recombination mechanisms (see section 2.2) in thin film solar cells is to measure V_{OC} at different temperatures. The advantage is that at the V_{OC} condition there is no current going through the device, which means that there are no parasitic circuit elements involved.

From the standard diode equation:

$$J = J_0 e^{\frac{qV}{Ak_B T}} - J_L \quad (3)$$

As the photo generated current density (J_L) $\approx J_{SC}$ in high-quality solar cell and the diode current density (J_0) can be expressed as

$$J_0 = J_{00} e^{\frac{-E_A}{Ak_B T}} \quad (9)$$

one can write an equation for V_{OC} as

$$V_{OC} = \frac{E_A}{q} - \frac{Ak_B T}{q} \ln \left(\frac{J_{00}}{J_{SC}} \right) \quad (10)$$

where E_A is the recombination activation energy, A the ideality factor, $k_B T/q$ is the thermal voltage and J_{00} a weakly temperature dependent saturation current density pre-factor. E_A , A , and J_{00} all depend on the dominating recombination mechanism [53]. A semi-logarithmic plot of J_{SC} vs. V_{OC} at a given temperature can yield A and J_{00} [39]. A is usually only weakly dependent or independent of the temperature [53][39]. For devices that fulfill this condition, the recombination activation energy E_A can be determined by plotting the V_{OC} as a function of the temperature. E_A is obtained from where an extrapolated line, from the linear regime of V_{OC} around 300 K, intercepts the y-axis at $T = 0$ K, as illustrated in Figure 4.3. Furthermore, a measure of A and J_{00} can be obtained from the slope of the line.

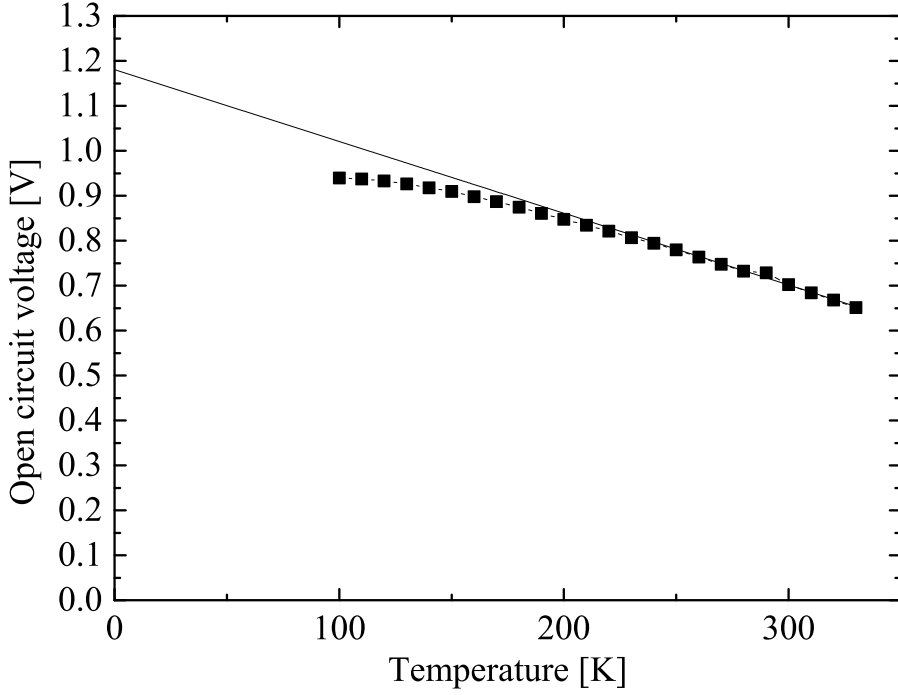


Figure 4.3. Open circuit voltage plotted versus temperature for a high-quality CIGS reference solar cell (containing a CdS buffer layer) from the series in paper V.

One can conclude that SRH recombination in the absorber bulk is the dominant recombination mechanism if E_A is close to the absorber E_g at the absorber/buffer layer interface as $T \rightarrow 0$ K [53][39][55]. On the other hand, an E_A that is lower than the absorber E_g at the absorber/buffer layer interface is an indication that interface recombination is the dominant mechanism and E_A is in those cases the interface recombination barrier Φ_b [55][42] (see Figure 3.6).

The temperature-dependent J-V measurements done in paper V are performed in a cryostat-based setup with the sample stage cooled by liquid N_2 . Illumination is provided by a white LED.

4.4 Numerical simulations

Numerical simulations can be a valuable tool to understand and explain the measured J-V characteristics of CIGS solar cells. In paper V an one-dimensional device simulation tool, called SCAPS-1D (a Solar Cell Capacitance Simulator) [56], is employed. The SCAPS programme was originally developed for cell structures of thin film CuInSe₂ and the CdTe solar cells. In SCAPS a large number of parameters can be simulated at different temperatures and illuminations, including; V_{OC} , J_{SC} , FF , η , QE, generation and recombination profiles, carrier current densities, spectral response, heterojunction band structures, distribution of electric fields, etc.

5. Material properties of ZTO thin films deposited by ALD

The main topic of this thesis is to evaluate how the zinc tin oxide material, or $\text{Zn}_{1-x}\text{Sn}_x\text{O}_y$ (ZTO), functions as a buffer layer in thin film CIGS solar cells. Material characterization of layers and interfaces is essential when engineering CIGS solar cells and is a crucial part to understand the behavior and performance of the cells. Table 5.1 summarizes the different methods utilized in this thesis, for what information they have been used to obtain, and in which paper they have been implemented. A detailed description and discussion of each method lies outside of the scope of this thesis, but a short general description of each method is found in Appendix I. This chapter goes through the material properties that are obtained for the ALD-ZTO process in the different papers.

Table 5.1. List of material characterization methods used in this thesis.

Characterization method	Abbreviation	Used to obtain material property	In paper
Profilometer	-	Thickness	I, III, VI
X-ray reflectivity	XRR	Thickness, density	III, IV, VI
Scanning electron microscopy	SEM	Thickness	II
Transmission electron microscopy	TEM	Thickness, structure, surface coverage	III, IV, V, VI
X-ray diffraction	XRD	Structure	II, IV, VI
Rutherford backscattering spectroscopy	RBS	Composition	III, IV
X-ray fluorescence	XRF	Composition	I, IV, VI
X-ray photoelectron spectroscopy	XPS	Surface coverage, elemental depth profile	III, IV
Energy dispersive X-ray spectroscopy	EDS	Elemental depth profile	II, III, VI
Secondary ion mass spectroscopy	SIMS	Elemental depth profile	I
Reflectance-transmittance spectroscopy	R-T	Light reflectance, transmittance, absorption and optical band gap	III, VI
Ellipsometry	-	Band gap, refractive index	II, IV
X-ray absorption spectroscopy	XAS	Conduction band energy level	II
X-ray emission spectroscopy	XES	Valence band energy level	II
Four point probe	-	Sheet resistance	I
Hall measurement	-	Resistivity, charge carrier density, mobility	VI

5.1 The ALD process for ZTO

In this thesis the ZTO films are solely produced by ALD following a standard process that involves a Microchemistry F-120 ALD reactor equipped with the precursors: diethyl zinc (DEZn or $\text{Zn}(\text{C}_2\text{H}_5)_2$), tetrakis(dimethylamino) tin (TDMASn or $\text{Sn}(\text{N}(\text{CH}_3)_2)_4$), and deionized water 18 M Ω cm (H_2O). Both the water and the diethyl zinc precursors are effused into the chamber at room temperature, whereas the Sn precursor is heated in a N_2 bubbler in a water bath to 40 °C to achieve a suitable vapor pressure. As a carrier gas, nitrogen, N_2 (6N), is used. The samples are loaded into the reactor at least 30 min prior to film deposition for temperature stabilization. The pulse cycle sequence is DEZn or TDMASn: N_2 : H_2O : N_2 , as il-

lustrated in Figure 3.9, and the pulse sequence times 400:800:400:800 ms. The reactor and process are in more detail described in [57]. The $[\text{Sn}]/([\text{Zn}]+[\text{Sn}])$ composition of the ZTO films is controlled by the relative number of zinc or tin containing precursor pulses. As an example, a process with a Zn:Sn pulse sequence of 3:2 is defined as one with three Zn precursor: N_2 : H_2O : N_2 cycles for every two Sn precursor: N_2 : H_2O : N_2 cycles and the $\text{Sn}/(\text{Zn}+\text{Sn})$ cycle fraction is thereby 0.4.

Other deposition conditions such as deposition temperature, number of pulse cycles and relative amount of tin or zinc containing precursor cycles are varied in the different papers to investigate these conditions effect on material properties, and ultimately the performance of ZTO buffer layer containing CIGS solar cells. Table 5.2 summarizes the deposition conditions that are used in the different papers. The deposition conditions affect the material parameters, and these changes are discussed in this section, while the influence of the material parameters on solar cell performance is discussed in section 6.

Table 5.2. Summary of the deposition conditions that are used in the different papers in this thesis.

Deposition condition	Paper					
	I	II	III	IV	V	VI
Substrate temperature	120 °C	120 °C	120 °C	Varied	Varied	135 °C
Number of cycles	500	Varied	Varied	1000	1000	600
$\text{Sn}/(\text{Zn}+\text{Sn})$ cycle fraction	0.4	Varied	0.4	Varied	0.4	0.5

The glass substrates used for material analysis of the ZTO films is either quartz glass, or the low-iron SLG described in section 3.1.1. Furthermore, in paper II silicon substrates is used.

5.2 General ALD growth of ZTO

The ALD process of growing the ternary compound ZTO films includes both $\text{DEZn}:\text{N}_2:\text{H}_2\text{O}:\text{N}_2$ and $\text{TDMA}:\text{N}_2:\text{H}_2\text{O}:\text{N}_2$ cycles. To have a good control of the growth in an ALD process it is important that the reactions are self-terminating (see section 3.2.5) [49]. It has previously been shown that the reactions are self-terminating in the process of growing pure ZnO from DEZn and water [58] and pure SnO_2 from TDMA and water [59].

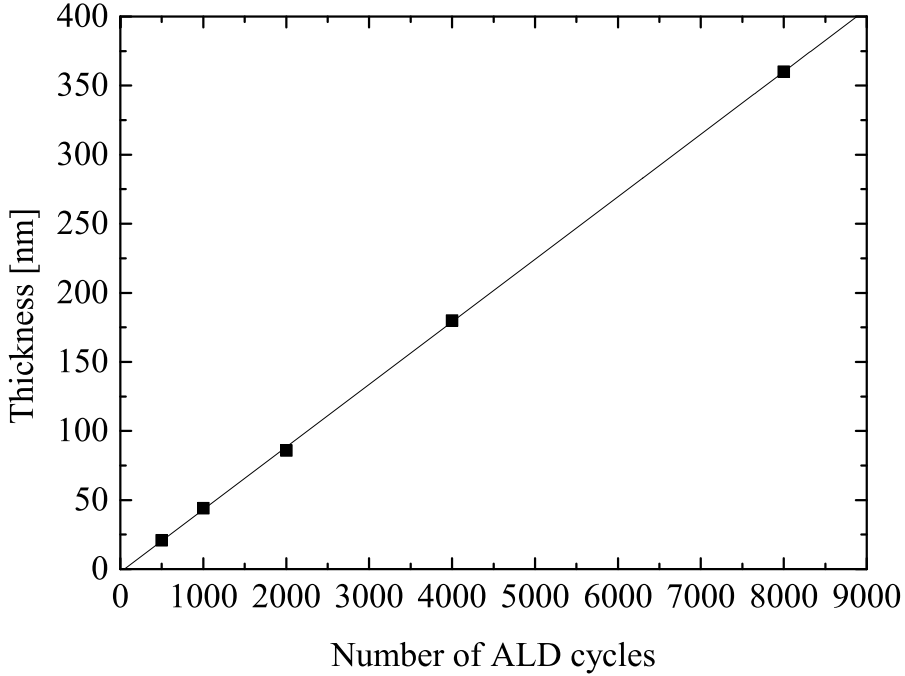


Figure 5.1. Number of DEZn/TDMASn:N₂:H₂O:N₂ cycles deposited with a Sn/(Zn+Sn) cycle fraction of 0.4 at 120 °C as compared with the resulting thickness of the ZTO film, measured by XRR and profilometer in paper III.

The number of pulse cycles used together with the growth rate per cycle determines the thickness of ALD films. The growth rate of ternary ZTO shows a linear growth with respect to the number of pulse cycles. At a deposition temperature of 120 °C and a Sn/(Zn+Sn) cycle fraction of 0.4 the growth rate is found to be $\sim 0.4 \text{ \AA/cycle}$, as Figure 5.1 illustrates. In paper IV, the growth rate of ZnO and SnO_x is found to be 1.6 and 1.1 \AA/cycle , respectively, at a deposition temperature of 120 °C. The growth rate of the ternary ZTO films is therefore much lower than for the binary oxides, which is due to a significantly reduction of the reaction site density on a ZnO surface after a TDMASn treatment [60] (further discussed in section 5.3). The growth rates of both the binary oxides and the ternary ZTO films in this thesis correlate well with previous findings [61].

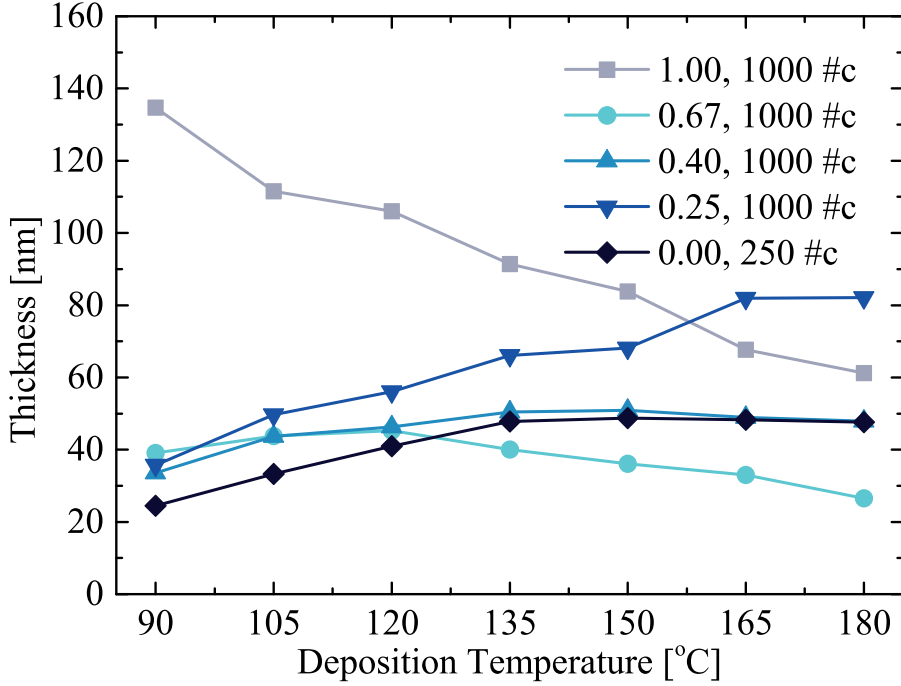


Figure 5.2. Thickness as a function of deposition temperature, measured by XRR, for binary ZnO and SnO_x films along with ternary ZTO films. These are deposited on glass substrates with Sn/(Zn+Sn) cycle fractions of 1.00, 0.67, 0.40, 0.25 and 0.00 by the stated number of deposition cycles (from paper IV).

In paper IV the deposition temperature is varied and the influence on the thickness, i.e. the growth rate, investigated. Figure 5.2 shows that pure ZnO layers exhibit a growth rate that initially increases with the substrate temperature until around 135 °C, where the growth rate becomes temperature independent and stays at ~ 1.8 Å/cycle. This behavior is typical for some ALD processes and the reason for the lower growth rate at lower deposition temperature is that the growth rate is limited by reaction barriers and insufficient energy of the reactants at the sample surface (see section 3.2.5). It is also common that an ALD process has a region of temperature independent growth within the ALD-window of self-terminating reactions (see section 3.2.5). Generally, ZnO deposition from DEZn and H₂O has this region of temperature independent growth between ~ 110 and ~ 170 °C [58]. The growth rate of ~ 1.8 Å/cycle within the process window, obtained in paper IV, also corresponds well with previously reported values [58]. At deposition temperatures above this region (not reached in paper IV) the growth rate may either increase, due to non-saturated growth caused by thermal decomposition of DEZn [62], or decrease, due to desorption of H₂O from the film surface [63][64][65].

In contrary to the growth of ZnO, the growth rate of SnO_x does not demonstrate any region of temperature independent growth. Rather, the growth rate decreases with increasing deposition temperature, from ~1.3 Å/cycle at 90 °C to ~0.6 Å/cycle at 180 °C, which has been suggested to be due to a gradual decrease in surface hydroxyl groups [59][66].

Furthermore, as can be seen in Figure 5.2, the influence of the deposition temperature on the growth rate for the ternary ZTO films seem to correlate well with binary ZnO and SnO_x films, as the temperature dependent growth rate of the 0.67 Sn/(Zn+Sn) cycle fraction process is similar to that of the SnO_x and the 0.25 Sn/(Zn+Sn) cycle fraction process to the ZnO process.

5.3 Composition of ALD ZTO

The [Sn]/([Zn]+[Sn]) composition of ZTO films is controlled by the relative number of zinc or tin containing precursor pulses. As an example, a Sn/(Zn+Sn) cycle fraction of 0.4 includes three Zn precursor:N₂:H₂O:N₂ cycles for every two Sn precursor:N₂:H₂O:N₂ cycles. In the Zn_{1-x}Sn_xO_y notation, the index x corresponds to the [Sn]/([Zn]+[Sn]) composition of the films while y depends on x as in $y = x + 1$, with the assumptions that the oxidation states of zinc and tin are +2 and +4, respectively, and the simplification that there is no hydrogen in the films. For all ternary ZTO films in this thesis the [Sn]/([Zn]+[Sn]) composition is found to be lower than the Sn/(Zn+Sn) cycle fraction, as illustrated by Figure 5.3. Both the low Sn content with respect to the cycle fraction in the films and the lower growth rate of the ternary ZTO films compared with the binary oxides discussed in section 5.2 can be explained by that a TDMASn treatment of a ZnO surface significantly reduces the reactions site density, which originates from TDMASn having four ligands available for surface reactions [60]. An observation that point in the same direction is made in paper IV, where the ZnO and SnO_x cycles are mixed in different ways in two different 0.4 Sn/(Zn+Sn) cycle fraction recipes. In this investigation a pulse sequence of ZnO:ZnO:ZnO:SnO_x:SnO_x demonstrate a higher growth rate as compared with a pulse sequence of ZnO:SnO_x:ZnO:SnO_x:ZnO.

Furthermore, it is found in paper IV and in [61] that the growth rate of ternary ZTO is influenced by the Sn/(Zn+Sn) cycle fraction. As can be observed in Figure 5.2, the thickness of ZTO films deposited with a high Sn/(Zn+Sn) cycle fraction are at higher temperatures thinner than films deposited with a low Sn/(Zn+Sn) cycle fraction.

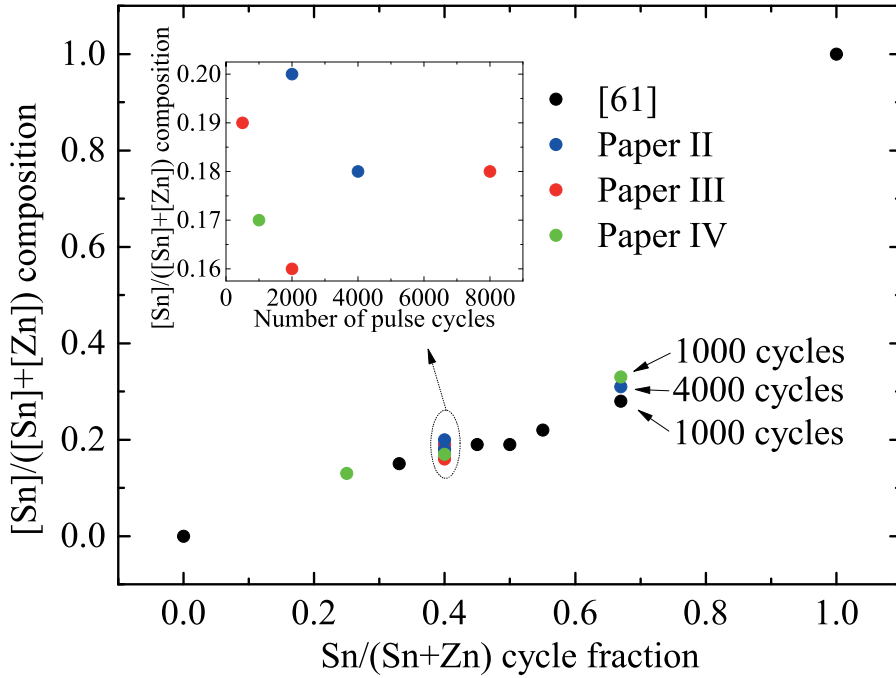


Figure 5.3. Summary of published ZTO composition values, measured by either RBS or RBS calibrated XRF, as a function of the Sn/(Zn+Sn) cycle fraction in the ALD process. All samples are deposited at a temperature of 120 °C. The samples from [61] have all been deposited with 1000 cycles. The inset shows measured [Sn]/([Zn]+[Sn]) composition as a function of the number of pulse cycles for samples produced with the 0.4 Sn/(Zn+Sn) cycle fraction.

It is noteworthy that the measured composition somewhat varies between different samples deposited with the same input deposition conditions, as can be seen at the 0.4 and 0.67 cycle fractions in Figure 5.3. These variations do not seem to be associated with changes in the film thickness, as the inset in Figure 5.3 shows. This is strengthened by the results in paper III, where an EDS scan over a 360 nm thick ZTO film shows a uniform distribution of Zn, Sn and O throughout the entire film. Rather, the variations in composition are likely to be related to both slightly different deposition conditions between different runs and measurement errors in the composition analysis methods.

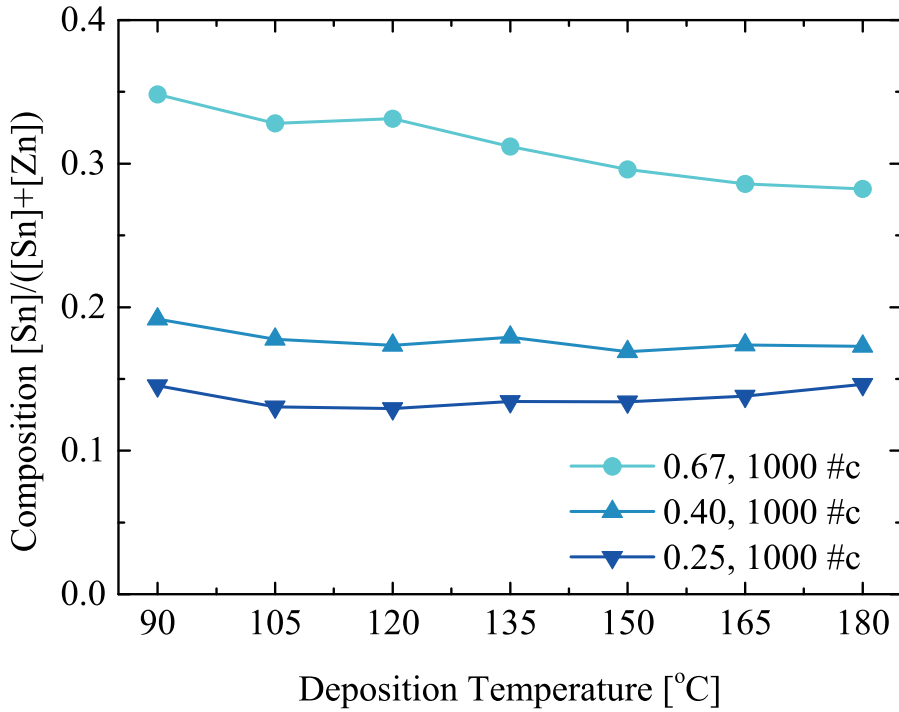


Figure 5.4. Composition as a function of deposition temperature, measured by RBS calibrated XRF, for ternary ZTO films. These are deposited on glass substrates with Sn/(Zn+Sn) cycle fractions of 0.67, 0.40 and 0.25 by the stated number of deposition cycles (from paper IV).

The deposition temperature has only a minor effect on the composition of ternary ZTO films, as Figure 5.4 demonstrates. In the investigated interval between 90 and 180 °C the films with the most varying composition are those deposited with the 0.67 Sn/(Zn+Sn) cycle fraction, where the [Sn]/([Zn]+[Sn]) composition decreased from 0.35 at 90 °C to 0.28 at 180 °C. Even though that the growth rate changes throughout the temperature interval, as Figure 5.2 shows, the composition of both the 0.4 and 0.25 Sn/(Zn+Sn) cycle fraction films show fairly constant [Sn]/([Zn]+[Sn]) composition of approximately 0.17 and 0.13, respectively.

To summarize, the composition of ternary ZTO films is uniform throughout the thickness and is above all controlled by the Sn/(Zn+Sn) cycle fraction, while the impact of deposition temperature and thickness of the films are negligible.

5.4 ALD growth of ZTO on CIGS

In ALD, different substrates may influence the initial growth rate of a process. This is the case when comparing growth of ZTO on a glass substrate to growing a layer with the same ALD parameters on CIGS. From TEM measurements in paper III, it is found that ZTO layers grown by 500, 2000 and 8000 cycles have thicknesses of approximately 13, 76 and 342 nm, respectively, on CIGS. It is concluded that ZTO films grown on CIGS are ~10 nm thinner as compared to ZTO films grown on quartz glass, regardless of the overall thickness of the films. This indicates a lower initial growth of ZTO on CIGS, usually called substrate inhibited growth, which can be caused by a lower number of reactive sites (see section 3.2.5) on the substrate compared to on the ALD-grown material [49]. Since the general growth rate of ZTO is ~0.4 Å/cycle, one can estimate that it takes about 250 cycles before the CIGS surface is completely covered by a ZTO film and normal film on film growth takes place. It is suggested that accumulation of sodium carbonate (Na_2CO_3) at the CIGS surface, especially for air exposed CIGS, is the reason for the low initial growth of ZnO on CIGS [67].

In paper III, an EDS scan over a 360 nm thick ZTO film deposited on CIGS, deposited with a Sn/(Zn+Sn) cycle fraction of 0.4 at a deposition temperature of 120 °C, demonstrates a uniform distribution of Zn, Sn and O throughout the entire film. Furthermore, this EDS scan shows no diffusion of elements across the interface. It also shows that the transition region of the interface is below 15 nm, with the resolution being limited by beam spreading in the sample and the spot size. That the ZTO/CIGS interface is sharp is confirmed by the EDS scans performed in paper V, which are shown in Figure 5.5. These two scans show the counts of the K-peaks of Cu and Zn for CIGS/ZTO interfaces where the ZTO is deposited at 120 °C and 180 °C, respectively. The In and Sn signals are not shown in the figure because they have overlapping L-peaks and Ga is omitted because Ga ions were used under the sample preparation, which leaves traces in the sample. The difference in intensities between the two scans is due to a shadowing effect from the sample holder that occurred in the scan of the 120 °C sample. Figure 5.5 demonstrates that no diffusion of elements across the interface seems to occur and that the interface is within 8 nm for both samples. This means that the influence of the deposition temperature on the inter-diffusion across the CIGS/ZTO interface seems to be limited.

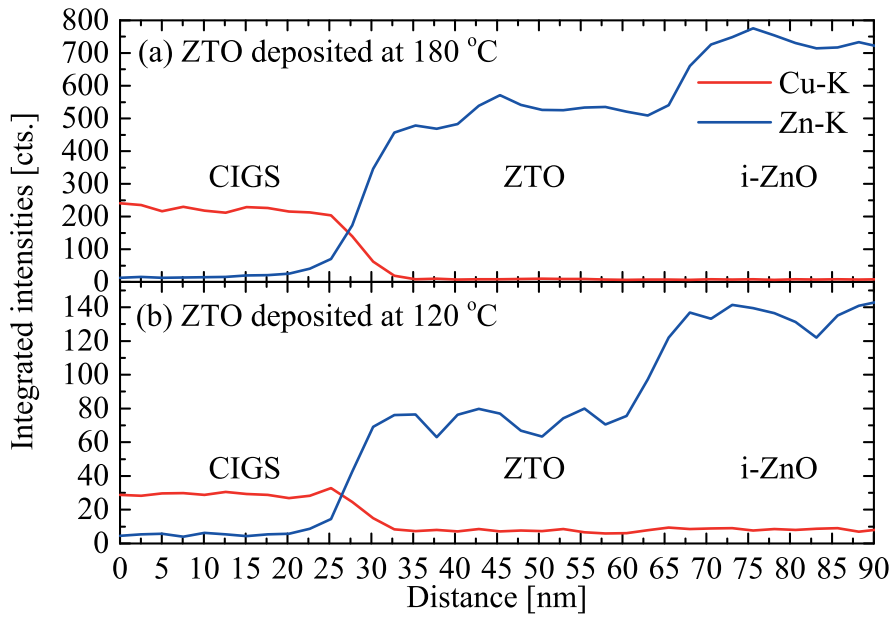


Figure 5.5. EDS scans over the CIGS/ZTO interface, where the ZTO buffer layer is deposited by a Sn/(Zn+Sn) cycle fraction of 0.4. (a) The ZTO layer is deposited at 180 °C. (b) The ZTO layer is deposited at 120 °C (from paper V).

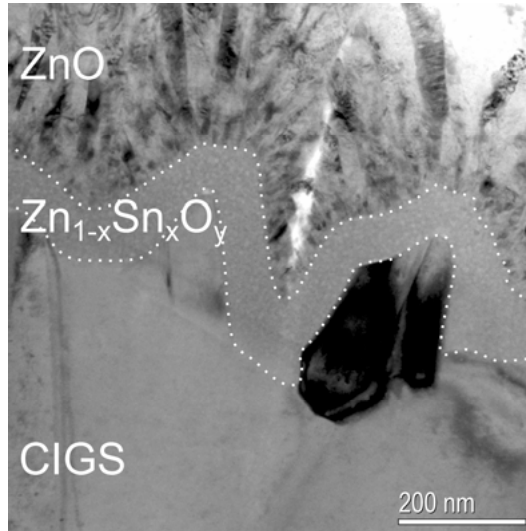


Figure 5.6. TEM image of a 76 nm thick ZTO buffer layer on CIGS deposited with a Sn/(Zn+Sn) cycle fraction of 0.4 (from paper III).

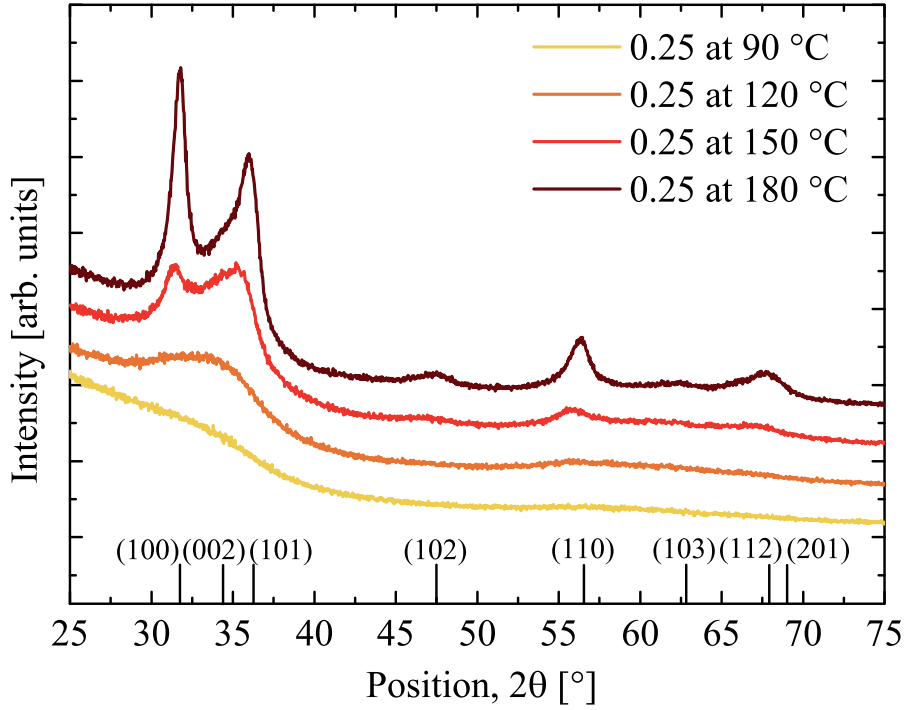


Figure 5.7. GIXRD diffractograms of ZTO films as-deposited by the 0.25 Sn/(Zn+Sn) cycle fraction process at deposition temperatures of 90, 120, 150 and 180 °C, respectively. The peak positions of powder ZnO are shown at the bottom.

As discussed in section 3.2.5, one of the benefits of ALD is that excellent step coverage can be achieved. This is also true for ALD growth of ZTO on CIGS. Figure 5.5 clearly illustrates the conformal coverage of a ZTO buffer layer on a rough CIGS surface. The excellent step coverage means that even layers as thin as 13 nm yield a complete coverage of the CIGS surface, according to the TEM and XPS analysis performed in paper III.

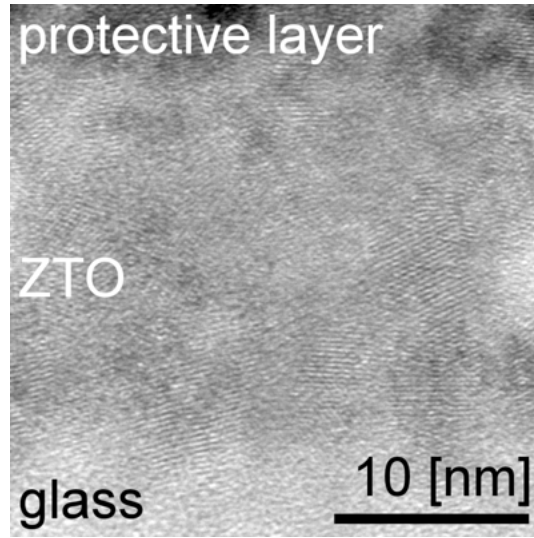


Figure 5.8. A high resolution TEM image of a ZTO film deposited by the 0.25 Sn/(Zn+Sn) cycle fraction process at a deposition temperature of 90 °C.

5.5 Structure of ALD ZTO

Binary ZnO as-deposited by ALD with DEZn and water as precursors crystallizes in the hexagonal wurtzite structure [61][58], while as-deposited binary SnO_x from the TDMASn and water precursors appears to be amorphous, according to XRD measurements [61][59][66].

In general, ternary ZTO can form two crystal structures; the metastable zinc metastannate structure, ZnSnO₃, and the stable zinc orthostannate structure, Zn₂SnO₄ [68]. However, ZTO films as-deposited by TDMASn, DEZn and water, are in general considered to be amorphous above a [Sn]/([Zn]+[Sn]) composition of ~0.1 at 120 °C [69][61][70]. That ZTO is amorphous can be a benefit since no stress due to lattice mismatch between the ZTO and the CIGS is induced. This could possibly reduce the amount of recombination centers at the CIGS/buffer layer interface. Furthermore, the lack of crystal boundaries in an amorphous buffer layer could make it better at preventing shunt currents as grain boundaries are common shunt paths.

In paper IV the general assumption that ALD ZTO is amorphous is questioned. The results from the XRD measurements in this study demonstrate that a crystalline-to-amorphous transition occurs at higher deposition temperatures, as demonstrated in Figure 5.7. Broad peaks that correspond to the high intensity peaks of crystalline ZnO appear in the diffractograms at higher deposition temperature and higher zinc content.

Furthermore, in the high resolution TEM image in Figure 5.8, areas of parallel atomic planes are visible. Although this ZTO film appears to be completely XRD amorphous in the diffractogram in Figure 5.7 Fourier transformation reveals that these lattice planes line up well with the positions for polycrystalline ZnO. This discloses that the ZTO film has a polycrystalline character with an apparent grain size approximated to be in the range of 10 nm. A combination of too small crystallites with poor crystalline quality, that give rise to a large peak broadening, and a too small diffraction volume for the XRD measurement are probably the reasons why the ZTO film looks amorphous in XRD, while the TEM images demonstrate a nano-crystalline character.

The interpretation made in paper IV of the XRD and TEM results is that the ZTO films contain some small pure zinc oxide, ZnO, or tin doped zinc oxide, ZnO(Sn), crystallites of sizes in the range of 10 nm, possibly surrounded by an amorphous material. These crystallites are found to decrease in size with increasing tin content and decreasing deposition temperature. Complementary high resolution TEM images of one of the cells deposited at 120 °C and one of the cells deposited at 180 °C is done in paper V. This study demonstrate that the ZTO buffer layer have the same morphology when deposited on CIGS as compared to the glass substrates in paper IV. The sample where the ZTO buffer layer is deposited at 120 °C shows few crystals, and their sizes are approximately 3-4 nm, while the 180 °C sample demonstrates more crystals, and their sizes are around 5-7 nm.

One can find support for this theory in the literature. The crystal size and quality has previously been found to increase with deposition temperature for ALD grown ZnO [62]. The theory of formation of small crystallites has also been suggested by [66] in the case of X-ray amorphous SnO_x, deposited from TDMASn and water, that after annealing showed broad and low intensity XRD peaks corresponding to rutile SnO₂. Furthermore, formation of crystalline Zn₂SnO₄ after annealing of ALD grown ZTO, and that the phase separation temperature is dependent on the Zn/Sn ratio and starts at lower annealing temperatures for more zinc rich films has been observed in [71]. The crystallization of as prepared XRD-amorphous or multiphase nano-crystalline ZTO after annealing has also been observed for other deposition techniques such as pulsed laser deposition [72] and RF magnetron sputtering [73].

To summarize, in amorphous ZTO thin films, formation of small crystallites seems to occur and these crystallites can be ZnO, ZnSnO₃, Zn₂SnO₄ or SnO₂. What kind of crystallites that will form and at what deposition or annealing temperature seems to depend on the composition of the films and the growth kinetics of different deposition techniques. Higher zinc content seems to generally require lower temperatures for crystallization to occur.

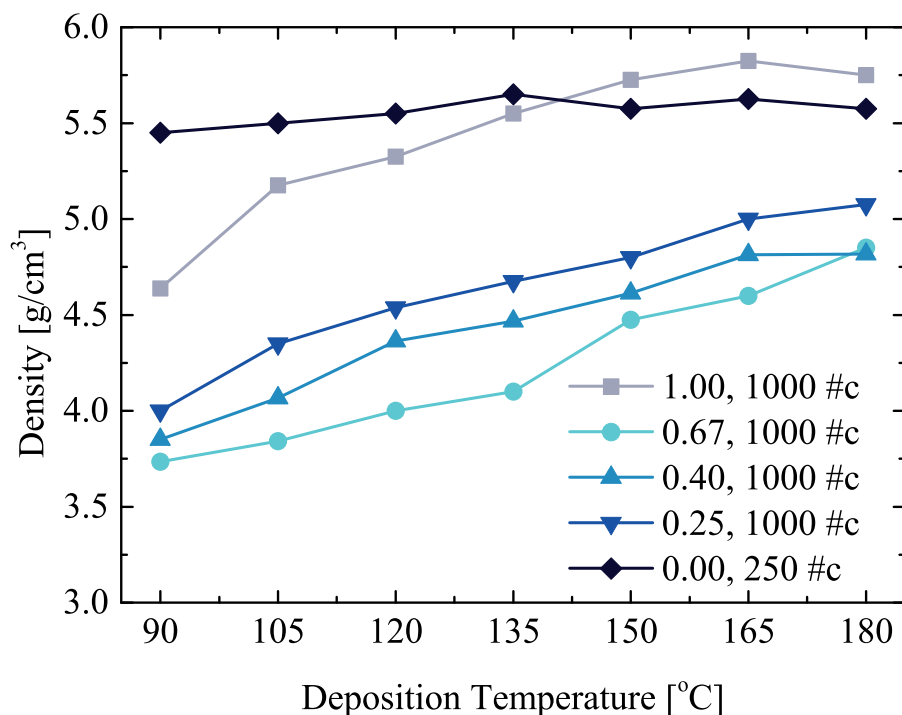


Figure 5.9. Density as a function of ALD deposition temperature, measured by XRR, for binary ZnO and SnO_x films along with ternary ZTO films. These are deposited on glass substrates with Sn/(Zn+Sn) cycle fractions of 1.00, 0.67, 0.40, 0.25 and 0.00 by the stated number of deposition cycles (from paper IV).

The effect of deposition temperature on the density of ZTO films is investigated in paper IV. The ternary ZTO films are found to be less dense than the binary ZnO and SnO_x films and the density of the ZTO films increases with increasing Zn content, as Figure 5.9 demonstrates. When the deposition temperature is increased from 90 to 180 °C, the density of the X-ray amorphous SnO_x and the ZTO films are found to increase more or less linearly with temperature, by ~1 g/cm³ in total. The deposition temperature is found to have no effect on the crystalline ZnO films as they constantly demonstrate a value of about 5.5 g/cm³, which is close to the bulk value of 5.6 g/cm³ for ZnO.

In general crystalline materials are more densely packed than amorphous materials so the amorphous-to-semi-crystalline transition in the ZTO films is one likely explanation to the density trends. Another possible explanation is that there is a higher presence of hydrogen, in the form of hydroxyl groups, remaining in the films deposited at lower deposition temperatures.

5.6 Optical properties of ALD deposited ZTO

The band gap of ZTO heavily depends on the composition as concluded in paper II. In this paper the E_g , E_V and E_C of ZnO, SnO_x and ZTO with different [Sn]/([Zn]+[Sn]) composition are determined from XAS and XES spectra and are summarized in Table 5.3. As can be seen in Table 5.3 E_g , E_V and E_C depend on the composition in a none trivial way. Furthermore, ZTO films with a [Sn]/([Zn]+[Sn]) composition of around 0.2 have a E_g of 3.0 eV, which is significantly higher than the band gap of CdS.

Table 5.3. Variation in E_g , E_V and E_C as compared to ZnO as a function of [Sn]/([Zn]+[Sn]) composition measured by XAS and XES (from paper II).

Sample	[Sn]/([Zn]+[Sn]) composition	E_g [eV]	E_V as compared to ZnO [eV]	E_C as compared to ZnO [eV]
S1	0	3.3	0	0
S2	0.13	2.2	1.2	0.1
S3	0.18	3.0	0.4	0.2
S4	0.20	3.0	0.5	0.3
S5	0.31	2.5	0.8	0.1
S6	1	2.2	1.0	-0.1

In addition to a high band gap, ZTO with a [Sn]/([Zn]+[Sn]) composition of around 0.2 has a high transmittance in the wavelength region of 350-1200 nm, regardless of the thickness, as measured by absorption spectroscopy in paper III.

It is not only the composition that effect the optical properties if ZTO. In paper IV spectroscopic ellipsometry measurements show that the refractive index increase with increasing deposition temperature. This is probably due to the higher density of the ZTO films deposited at higher temperatures. Furthermore, the Tauc plots [74] in Figure 5.10 (based on the data from the ellipsometry measurements) reveal that also the band gap is effected by the deposition temperature. The indirect Tauc model, which probably is more relevant than a direct band gap model since the films are X-ray amorphous, yields a decrease in E_g from 3.74 at 90 °C to 3.20 at 180 °C.

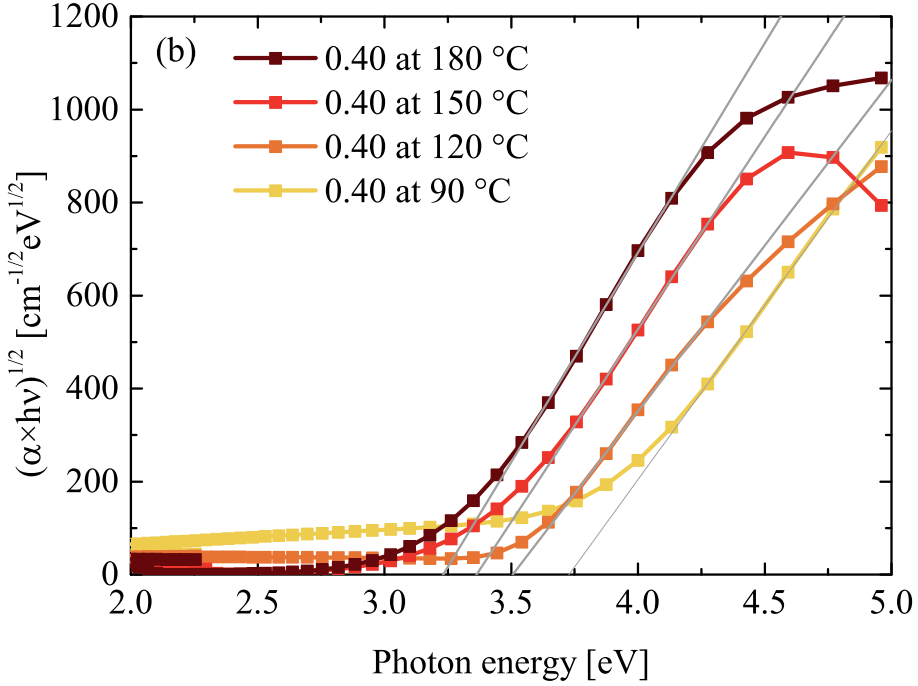


Figure 5.10. Tauc plots of ZTO films where an amorphous phase model with $r = 1/2$ is used. The films are deposited with a Sn/(Zn+Sn) cycle fraction of 0.4 at deposition temperatures of 90 °C, 120 °C, 150 °C and 180 °C, respectively (from paper IV).

It should be noted that the Tauc method is quite sensitive to the used models and how well they fit to the measured data, especially for amorphous type band gaps. In both paper III and IV, the obtained E_g values from the Tauc method are higher, approximately 0.3-0.7 eV, than the E_g extracted from XAS and XES measurement in paper II for corresponding ZTO films. Using XES and XAS for determining the E_g can also be associated with some uncertainties as the method can underestimate the optical band gap due to band gap tails. However, in paper II it is shown that the trends in E_g are the same regardless of the method.

Disregarding the exact values, the trend in Figure 5.10 is clear, and that is that the E_g of ZTO thin films decreases with an increasing deposition temperature. This trend can be related to the changes in material structure with increasing temperature (see section 5.5) as small semiconductor nanoparticles are subjected to quantum confinement effects [75]. The quantum confinement effects cause the band gap to expand from its bulk value as the nanoparticles get smaller. It has previously been found that ZnO nanoparticles in sizes up to 9 nm are small enough to demonstrate quantum confine-

ment effects, and that the band gap, E_g (in eV), relates to the particle diameter, d (in nm), according to the relation [76][77]:

$$E_g = 3.30 + \frac{0.293}{d} + \frac{3.94}{d^2} \quad (11)$$

The ZnO or ZnO(Sn) nano-crystallites that is found in the films in paper IV and V are in this size range. The trend of the decreasing band gaps of ZTO as a result of increasing deposition temperature can thereby be explained by that the ZnO or ZnO(Sn) nano-crystallites becomes larger as the deposition temperature is increased, which is making the quantum confinement effect less prone.

Furthermore, the results from the J-V and V_{OC} vs T measurements together with simulations, performed in paper V, indicates that a majority of the changes in E_g at different deposition temperatures are manifested through shifts in E_C . The findings of [77] support these conclusions as they prove that essentially all quantum size effects of pure-ZnO quantum dots takes place in the CB energy level.

6. Performance of CIGS solar cells with ZTO buffer layers

ZTO as a buffer layer has earlier been investigated in CdTe thin film solar cells, using RF magnetron sputtering as the deposition method, with an obtained record efficiency of 16.5 % [78]. The first two investigations of the ALD ZTO buffer layer in CIGS solar cells [69][61] were done within the ÅSC group at Uppsala University prior to this thesis. So far, the certified record conversion efficiency for a CIGS cell containing a ZTO buffer layer is 18.2 % (in paper I).

6.1 General performance of the ÅSC baseline CIGS

The baseline process for making CIGS solar cells is described in detail in Paper I, and also briefly in section 3.1. This baseline produces on a regular basis CIGS solar cell, with the CdS buffer layer and without the AR coating, with η between 15.4% and 17.4%. The discrepancy in the current baseline process between samples made in separate CIGS deposition runs is within 2% (absolute), and is a combination of the reproducibility of all process steps. The variation between samples made in the same CIGS deposition run, which usually means that the different samples also are included in the same deposition run for the rest of the process steps, is usually below 0.3 % (absolute).

6.2 Performance of ZTO buffer layers as compared to CdS

When developing alternative buffer layers it is common to compare them to reference samples containing a standard CBD deposited CdS layer. This is also done in paper I, III, V and VI. The general observation in all these papers is that a well behaving ZTO buffer layer yields higher J_{SC} , but so far lower V_{OC} and slightly lower FF , as compared with CdS reference samples. As discussed in section 3.2.4, this is the same typical characteristics that most alternative buffer layers have. The difference in J_{SC} and V_{OC} between

the ZTO and CdS is clearly illustrated when the certified record cells from paper I are compared in Table 6.1.

Table 6.1. Certified J-V measurement of the two ÅSC baseline record cells by Fraunhofer ISE CalLab PV Cells.

Sample	V_{OC} [mV]	J_{SC} [mA/cm ²]	FF [%]	η [%]
CdS buffer layer	722.7 ± 3.6	33.76 ± 0.94	76.09 ± 0.76	18.56 ± 0.60
ZTO buffer layer	688.7 ± 3.4	35.07 ± 0.98	75.30 ± 0.75	18.19 ± 0.59

The reason why the ZTO buffer layer yields higher current is the higher transparency of ZTO as compared to CdS, which reduces the parasitic absorption by the buffer layer in the ultra violet (UV)-blue region of the spectrum. This is distinctly visible in the EQE measurements of the two cells in Figure 6.1.

The reason for the lower V_{OC} obtained for ZTO is not yet completely understood. However, it is probably one, or a combination, of the general advantageous properties of the CBD deposited CdS stated in section 3.2.4. Namely, that ALD ZTO lacks the n-doping effect of the top of the CIGS layer that has been suggested to occur with CBD deposited CdS [21][47]. Another possible reason could be the lack of the CIGS surface etching effect in the dry ALD process, which the CBD process exhibits [48]. The surface of the CIGS is known to start to oxidize immediately when it is exposed to air. Even if the air-exposure is kept to a minimum under the transfer from the CIGS system to the ALD reactor in our lab, the oxidation of the surface and the lack of the etching effect in the ALD process could be a reason for the lower V_{OC} . This could possibly be avoided if the ALD reactor was connected to the CIGS system so that the vacuum was never breached under the transfer, as would likely be the case in an industrial production line. However, apart from the oxides that are etched in the CBD bath other impurities, such as Cu_xSe phases, would still remain at the interface and it is yet to be proven that an all vacuum process production line could have a positive effect on V_{OC} . Another way of improving the interface is to pre-treat the CIGS surface prior to the buffer layer deposition by a KCN etch, which has proven to yield better results [79]. An KCN etch is implemented in the series of paper V as it is found that the performance of the ZTO buffer layer on untreated CIGS from the in-house batch reactor is rather bad.

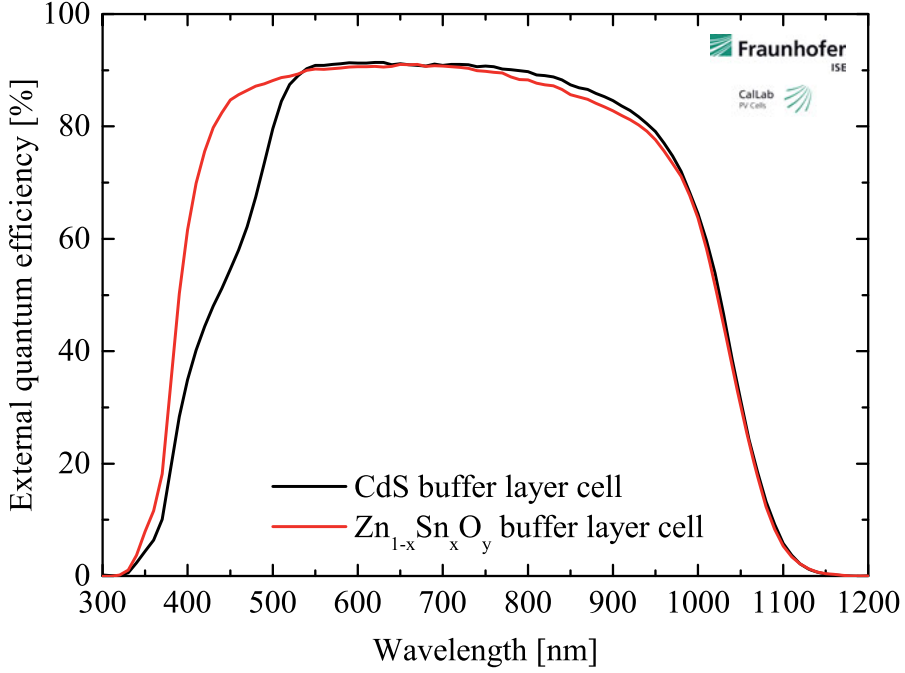


Figure 6.1. EQE measurement of the two record cells processed by the ÅSC baseline procedure (from paper I).

The slightly lower FF observed for well behaving ZTO sample as compared to CdS reference samples can in most cases be explained by the lower V_{oc} . The effect of the V_{oc} on the FF can be calculated by the empirical expression:

$$FF = \frac{v_{oc} - \ln(v_{oc} + 0.72)}{v_{oc} + 1} \quad (12)$$

Where v_{oc} is the normalized voltage defined as $V_{oc}/(AkT/q)$ [17]. The ideality factor A is found to be ~ 1.7 for both ZTO and CdS buffer layer samples in both paper III and VI. Using equation 12 results in a difference in FF of $\sim 0.75\%$ due to the difference in V_{oc} between the two record cells in Table 6.1. This is also the actual measured difference in FF between the two samples. The difference in FF between ZTO samples and the CdS reference samples are in the same magnitude also in the other papers.

6.3 Conduction band line-up in ZTO

6.3.1 Conduction band energy changes due to composition

In the initial two investigations of the ALD ZTO buffer layer done at the ÅSC it was shown that there is an intermediate optimum in solar cell conversion efficiency as a function of the $[\text{Sn}]/([\text{Zn}]+[\text{Sn}])$ composition [69][61]. This can be seen in Table 6.2. This optimum is due to a concurring maxima in V_{OC} and FF at an ALD Sn/(Zn+Sn) cycle fraction of 0.4, which corresponds to a $[\text{Sn}]/([\text{Zn}]+[\text{Sn}])$ composition of ~ 0.2 , as Figure 5.4 shows. Furthermore, J_{SC} is found to be independent on the composition.

Table 6.2. Solar cell performance as a function of ALD Sn/(Zn+Sn) cycle fraction deposited with 2000 cycles at 120 °C [61].

Cycle ratio	Thickness [nm]	V_{OC} [mV]	J_{SC} [mA/cm ²]	FF [%]	η [%]
ZnO	140	383	32.2	58.6	7.2
0.25	97	622	31.9	72.8	14.5
0.33	78	638	32.3	72.4	14.9
0.4	73	647	31.8	72.9	15.0
0.45	69	644	31.9	70.4	14.5
0.5	68	637	31.4	68.2	13.6
0.55	71	638	31.8	65.0	13.2
0.6	71	647	31.9	49.4	10.2
0.67	77	620	31.4	27.5	5.4
SnO _x	73	316	30.5	53.8	5.4
CdS ref	-	649	29.8	72.4	14.0

From the in-depth investigations of the electronic structure of ZTO in paper II, it is concluded that the optimum in V_{OC} and FF can be explained by a favorable CBO, which is formed when the ZTO buffer layer has an $[\text{Sn}]/([\text{Zn}]+[\text{Sn}])$ composition of 0.2. As shown in Table 5.3, the E_C of ZTO as compared to ZnO has a maximum of 0.3 eV at a Sn content of 0.2. By using literature data, the CBO at a $[\text{Sn}]/([\text{Zn}]+[\text{Sn}])$ composition of 0.2 is estimated to be a slightly positive spike of 0.1 eV in relation to CIGS with a $[\text{Ga}]/([\text{In}]+[\text{Ga}])$ composition of 0.3. This is similar to the CBO between CdS and CIGS. At both lower and higher Sn content, ZTO instead forms cliff-like CBO's, which explains the lower V_{OC} and FF values obtained for these compositions. A schematic illustration of the band alignment between ZnO, Zn_{1-x}Sn_xO_y, SnO_x and CIGS, based on the values in Table 5.3, is shown in Figure 6.2.

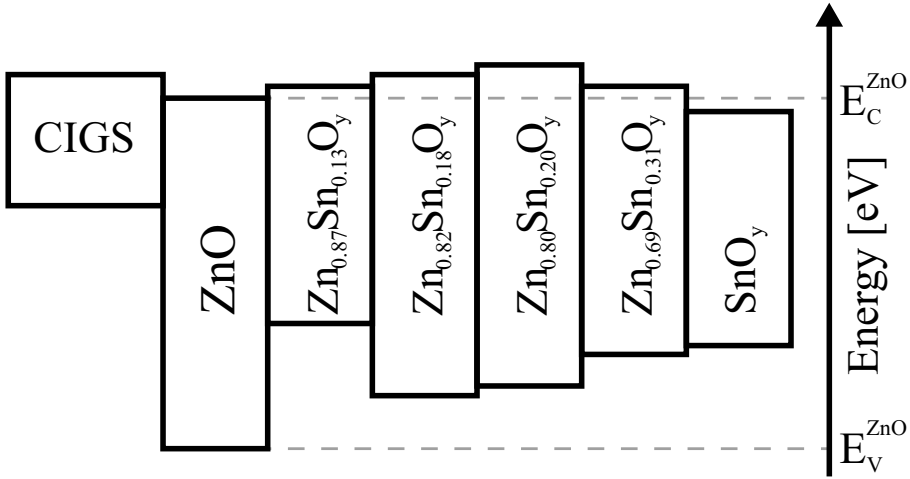


Figure 6.2. Band alignment between ZTO buffer layers and CIGS with a $[\text{Ga}]/([\text{In}]+[\text{Ga}])$ of 0.3, based on the values in Table 5.3 and literature data for the CIGS/ZnO alignment [80] (from paper II).

6.3.2 Conduction band energy changes due to morphology

It is not only the composition of the ZTO buffer layer that affects the band gap and positions of the valence and conduction bands. As discussed in section 5.6, the deposition temperature also influences the band gap of ZTO through quantum confinement effects in the nano-size ZnO crystallites that are formed in the ZTO buffer layer. These crystallites seem to become larger at higher deposition temperatures, which lead to a trend with decreasing E_g with increasing deposition temperature, from 3.7 eV at a deposition temperature of 90 °C to 3.2 eV at 180 °C, for films deposited with a Sn/(Zn+Sn) cycle fraction of 0.4.

In paper V, samples with ZTO buffer layers deposited with a Sn/(Zn+Sn) cycle fraction of 0.4 at different deposition temperatures are investigated, i.e. ZTO buffer layers with different nanostructures. As Table 6.3 shows, the J_{SC} is not affected by the deposition temperature, but there exists an optimal temperature interval between 105 and 135 °C, due to losses in V_{OC} and FF at higher and lower deposition temperatures. At lower deposition temperature the major loss is in FF , due a J-V rollover that can be seen in Figure 6.3 (a), and at higher deposition temperatures the major loss is in the V_{OC} .

Table 6.3. Average J-V parameters and standard deviation for samples containing 12 cells where the ZTO buffer layer is deposited at different temperatures (from paper V).

Deposition temperature [°C]	V_{OC} [mV]	J_{SC} [mA/cm ²]	FF [%]	η [%]
90	632 ± 7	36.4 ± 0.3	37.2 ± 3	8.5 ± 0.8
105	672 ± 10	35.6 ± 0.3	74.5 ± 0.4	17.8 ± 0.3
120	662 ± 9	36.3 ± 0.3	73.2 ± 1	17.6 ± 0.4
135	642 ± 3	38.5 ± 0.4	72.4 ± 0.3	17.9 ± 0.2
150	637 ± 6	35.7 ± 0.4	70.3 ± 0.9	16.0 ± 0.3
165	607 ± 10	35.0 ± 1	60.9 ± 8	13.0 ± 2
180	549 ± 20	35.2 ± 0.4	62.5 ± 2	11.9 ± 0.8
CdS ref	681 ± 4	35.2 ± 0.3	74.6 ± 0.6	17.9 ± 0.2

The J-V trends cannot be explained by changes in composition, since this is not affected by the deposition temperature, as Figure 5.4 shows, or by diffusion of elements across the interface, as Figure 5.5 demonstrates. Rather, the explanation for the J-V results in paper V is suggested to be the conduction band line-up. By simulating the solar cell stack and the performances of ZTO buffer layer samples in SCAPS, very similar results as the measured J-V characteristics are obtained if the assumption is made that all of the changes in E_g occur in the E_{CB} , while E_{VB} remains constant. This assumption is made since the ZTO seems to contain ZnO nanocrystallites (as discussed in section 5.5) and since essentially all of the quantum size effects of pure ZnO quantum dots have been found to affect the conduction band energy level [77]. The measured J-V performance of the actual cells and the simulated J-V performance based on measured material parameters of ZTO are shown in Figure 6.3 and the corresponding simulated band diagrams are demonstrated in Figure 6.4.

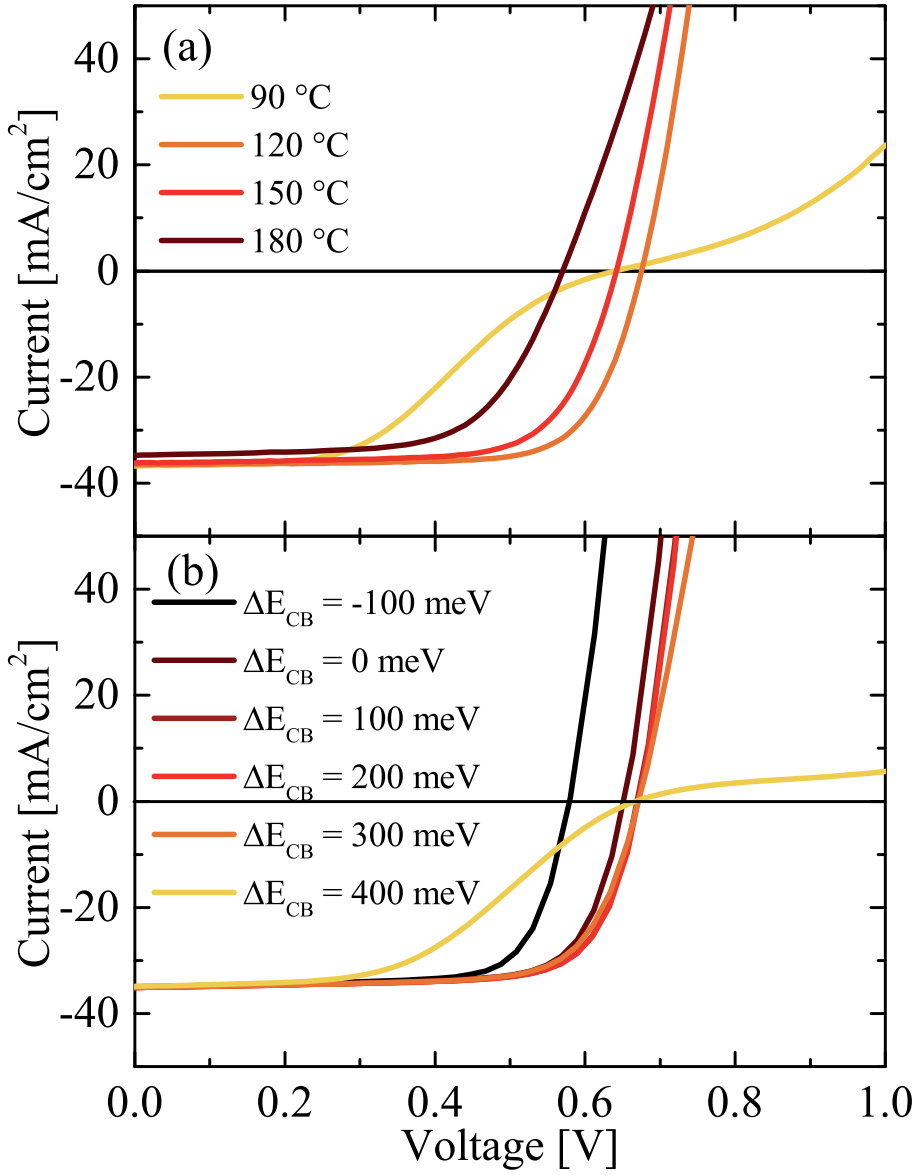


Figure 6.3. (a) J-V curves of the best solar cells where the ZTO buffer layer was deposited with a Sn/(Zn+Sn) cycle fraction of 0.4 at deposition temperatures of 90, 120, 150 and 180 °C, respectively. (b) Simulated J-V characteristics assuming different CIGS/ZTO conduction band offsets ΔE_{CB} (from paper V).

The simulations in Figure 6.4 shows that a large CBO spike 0.4 eV is formed when the E_g of ZTO is 3.7 eV, i.e. at a deposition temperature of 90 °C, and that a CBO cliff of -0.1 eV is formed at a ZTO E_g of 3.2 eV, i.e. at a deposition temperature 180 °C. The intermediate ZTO bandgaps, obtained at deposition temperatures of 105-135 °C, exhibit more favorable CBO's of a flat band or a small spikes. Figure 6.3(b) clearly illustrates that the highest conversion efficiencies are achieved for small spike CBO's between 0.1-0.3 eV. However, a too large spike, according to the simulations in Figure 6.3(b), leads to a blocking behavior with major FF losses and a slight decrease in V_{OC} . On the other hand, a cliff CBO will result in a major loss in V_{OC} .

Measurements of V_{OC} vs. T reveal that the activation energies are 1.10 and 1.13 eV, for the samples where the ZTO buffer layers are deposited at 120 °C and 150 °C, respectively. That means that the E_A is similar to the CIGS E_g close to the interface, which is estimated to 1.15 eV from EQE measurements of these two samples. As discussed in section 4.3, an E_A similar to the E_g means that Shockley-Read-Hall recombination in the absorber bulk is the dominant recombination mechanism [39][53], which indicates that a favorable CBO is formed for these two samples. The E_A values for the samples with ZTO buffer layers deposited at 90 °C and 180 °C are found to be significantly lower, ~ 0.7 and ~ 0.9 , respectively. This indicates that interface recombination is the dominant mechanism in these two samples [42][55][81], which correlates well with the theory that a large CBO spike is formed at 90 °C and that a CBO cliff is formed at 180 °C.

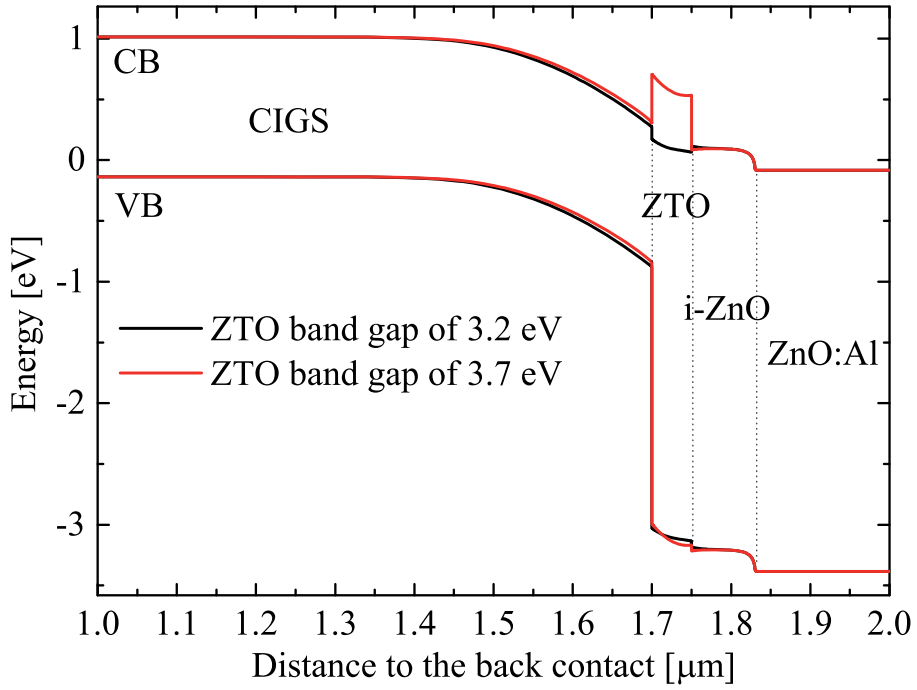


Figure 6.4. Simulated band diagrams at short circuit conditions of CIGS devices with ZTO bandgaps of 3.2 eV and 3.7 eV.

One can conclude that the simulated band diagrams and J-V characteristics, along with the V_{OC} vs. T measurements, correlate well with the measured J-V characteristics in Table 6.3 and it seems like the theory of conduction band offsets, discussed in section 3.2.3, can explain the behavior of the samples where the ZTO buffer layer is deposited at different deposition temperatures.

To summarize, both the composition and the nano-structure of the ZTO film affects the E_{CB} , which means that both the ALD Sn/(Zn+Sn) cycle fraction and/or deposition temperature can be used to tune the CBO between the buffer and the CIGS layers.

6.4 The effect of ZTO thickness on solar cell performance

In paper III the thickness of ZTO buffer layers is varied and the effect of the solar cell performance is investigated. The relationship between the ZTO buffer layer thickness and solar cell performance, for samples with and without the shunt preventing i-ZnO layer, is shown together with CdS buffer layer reference samples in Figure 6.5. This section focuses only on the ZTO buffer layer thickness changes, and performance by omitting the i-ZnO buffer from the window layer stack is discussed in section 7.1. The thickness of the ZTO does not influence the current, as the small variations in J_{SC} are not significant, and as expected the ZTO yields higher J_{SC} as compared to the CdS reference samples, as Figure 6.4 demonstrates.

For V_{OC} the situation is the opposite. The ZTO buffer layer is associated with lower V_{OC} values than the CdS references and there is a clear decreasing trend in V_{OC} for the ZTO samples when the thickness is increased. The decreasing trend of the V_{OC} is not fully understood, but one theory is that the ZTO has a low carrier concentration, i.e. low n-doping, which will lead to a decrease of the inversion in the top-most part of the absorber as the thickness of the buffer layer increases. In a preliminary study (not included in this thesis) it is found that the ZTO material is highly resistive and the resistivity is influenced by light. Depending of the light intensity values between 20-160 G Ω have been obtained. Due to the very high resistivity, it has not been possible to determine carrier concentration at Uppsala University, and the theory that it is a weaker inversion that lowers the V_{OC} needs further proof.

The slightly decreasing trend in FF with increasing ZTO thickness observed in Figure 6.5 can be correlated to the decreasing V_{OC} trend by using equation 12. As V_{OC} , and therefore also FF , decreases with increasing ZTO thickness the highest efficiencies are, as can be seen in Figure 6.5, achieved for samples where a ZTO buffer layer deposited with only 500 cycles is used. These 500 cycles correspond to a thickness of ~15 nm on CIGS as measured by TEM.

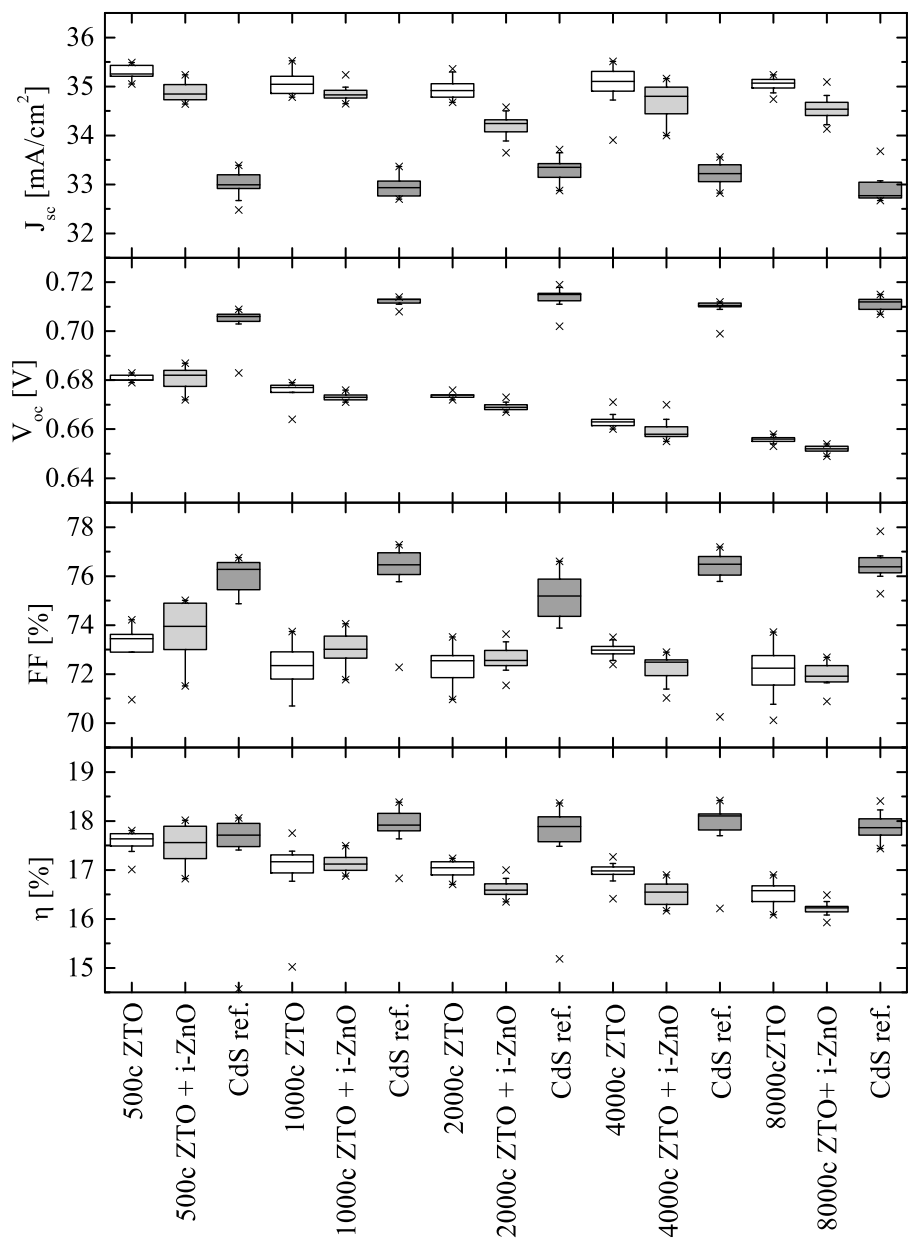


Figure 6.5. Box plots over J_{sc} , V_{oc} , FF and η for CIGS solar cells where the thickness of the ZTO buffer layer is varied and where the i-ZnO layer has been omitted. These cells are compared with the standard CdS reference samples with a fixed CdS layer thickness. The edges of the boxes represent the 25th and 75th percentile, the whisker lengths defines the upper inner and lower inner fence values, the line in the middle of the box marks out the median value and the crosses the minimum and maximum values (from paper III).

7. Window layer engineering

So far this thesis has only treated the effect on solar cell performance by exclusively changing the properties of the buffer layer, while the rest of the window layer stack is kept the same. However, the performance of a CIGS solar cell depends on all of the layers in the window layer stack and how they interact and work together. Changing from one buffer layer to another, or making changes in a buffer layers material properties, can have advantages that are only beneficial if changes are made to the other layers in the window layer stack as well. This chapter discusses some effects associated with the ZTO buffer layer if the other layers in the window layer stack are changed.

7.1 Omitting the i-ZnO layer

The highly resistive i-ZnO layer traditionally used in the window layer stack is needed for solar cells with CdS buffer layers to reduce the influence of shunt currents in CIGS solar cell [37][38]. The i-ZnO layer is used with ZTO in the certified record cells in paper I, but in paper III it is shown that this layer can be omitted. The white boxes in Figure 6.5 mark out the performance of ZTO buffer layer samples without the i-ZnO layer. Overall, ZTO buffer layer samples without an i-ZnO layer yield a slightly higher J_{SC} and V_{OC} than samples with an i-ZnO layer. The higher J_{SC} can be explained by that the onset of strong absorption in ZTO take place at higher photon energies than in ZnO and that the effective optical band gap of ZnO:Al is wider than that of i-ZnO, due to the Moss-Burstein effect [82][83]. Omitting the i-ZnO therefore reduces the absorption in the window layer stack of high energy photons in the UV-blue region of the spectrum, which is clearly demonstrated in Figure 7.2. The slightly higher V_{OC} obtained for ZTO samples without the i-ZnO layer compared with ZTO samples with the i-ZnO layer is likely associated with the higher current measured for the samples without the i-ZnO.

An interesting result when comparing ZTO buffer layers with and without the i-ZnO layer is the shift in FF between the 2000 and 4000 cycle samples in Figure 6.5. For thinner ZTO buffer layers higher FF are obtained if the i-ZnO is present, while higher FF is obtained for the two thickest ZTO buffer

layers if the i-ZnO is omitted. This can possibly be associated to the R_S and G_{SH} of the device. As mentioned in section 6.4, ZTO is highly resistive and it is observed in the literature that high resistivity of other ZnO-based alternative buffer layers is favorable for both FF and V_{OC} [84][85][86]. In paper III R_S and G_{SH} are extracted from the measured J–V data and as the thickness is increased from ~ 15 nm to ~ 340 nm, R_S increases from ~ 0.5 to ~ 1.0 Ωcm^2 , while G_{SH} decreases from ~ 2.5 to ~ 0.4 mS/cm^2 in the samples without the i-ZnO layer. Adding the i-ZnO on top of the ZTO buffer layer increases R_S but decreases G_{SH} . High R_S is negative for the FF , while low G_{SH} is positive as the leakage current then is restrained. The shift in FF might therefore be explained by the tradeoff between R_S and G_{SH} and that it is the total resistance of the ZTO and i-ZnO layers that decides the magnitude of these parameters.

The properties of both the ZTO buffer layer and the i-ZnO layer also affect the ability of the devices to prevent shunts. In paper III four shunted cells are found among the samples with thinner ZTO and no i-ZnO. This indicates a thin ZTO buffer layer possible needs an i-ZnO layer to avoid problems with shunts. However, paper III contains too few samples and cells for quantitative confirmation of this assumption.

7.2 Replacing the ZnO:Al contact with In_2O_3

In paper VI indium oxide, In_2O_3 , deposited by ALD is tried as a new front contact. This TCO is grown in the same Microchemistry F-120 ALD reactor as the ZTO buffer layer at a deposition temperature of 135°C , using cyclopentadienylindium(I), $\text{In}(\text{C}_5\text{H}_5)$, and a mixture of deionized water and oxygen gas as precursors. The pulse lengths for the In_2O_3 are 1200:800:400:1600 ms and the growth are found to be self-limiting. It turned out that the ALD In_2O_3 do not nucleate on neither CdS layers nor pure CIGS surfaces in the series of paper VI. The resulting films are found by XRD and TEM to be non-textured crystalline with a lateral grain size of ~ 60 nm. The density of the ALD In_2O_3 is determined to be 6.7 g/cm^3 by XRR.

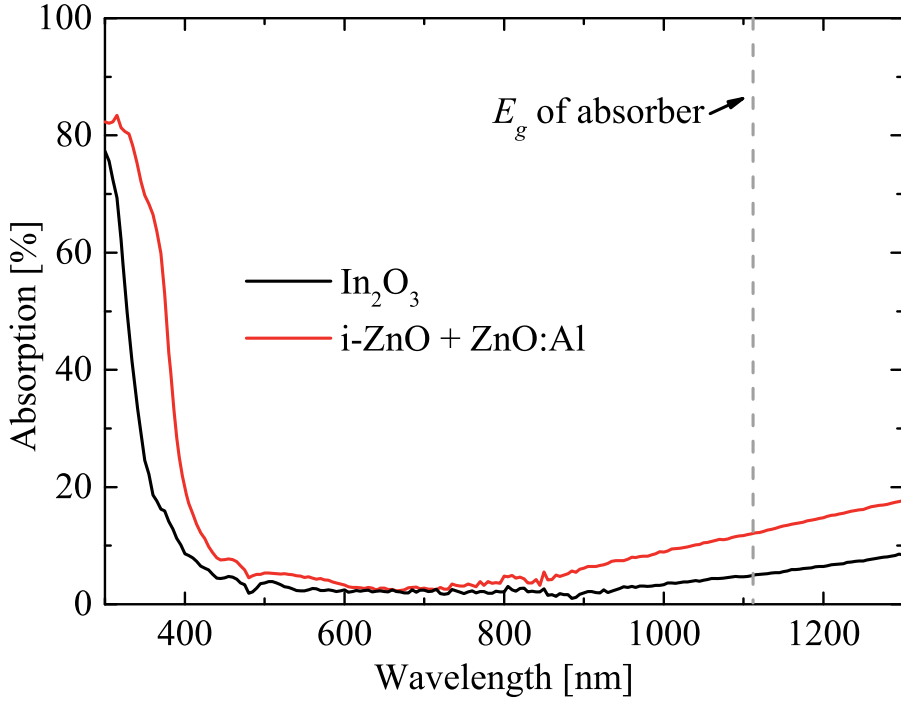


Figure 7.1. Optical absorption spectra of atomic layer deposited In_2O_3 and sputtered i-ZnO/ZnO:Al layers on glass.

The large grain size in the In_2O_3 layer contributes to a higher mobility (μ) as compared to the ZnO:Al , $46 \text{ cm}^2/\text{Vs}$ and $13 \text{ cm}^2/\text{Vs}$, respectively. The free charge carrier (electron) concentration (n) in In_2O_3 presumably originates from oxygen vacancies and is found to be 2.3×10^{20} . This is lower than the free electron concentration in the ZnO:Al TCO which is 7.3×10^{20} . The higher μ leads, despite of the lower n , to a lower resistivity of the In_2O_3 as compared to ZnO:Al . To compare the performance of the TCO's in CIGS solar cells the thickness of In_2O_3 is chosen to yield a similar R_{SH} of $\sim 30 \text{ } \Omega/\text{sq}$ as the sputtered ZnO:Al . The resulting thickness of the In_2O_3 and ZnO:Al are therefore 205 and 255 nm, respectively. The electrical properties of the two TCO's are summarized in the end of Table 7.1.

A low n in a TCO for solar cell applications is an advantage since free charge carriers can absorb the incoming photons in the near infra-red region (see section 2.3). The reduced electron concentration in In_2O_3 as compared to ZnO:Al leads, as can be seen in Figure 7.1, to a lower absorption for wavelengths above 700 nm. The higher transmission in this region should improve J_{SC} independently on the choice of buffer layer.

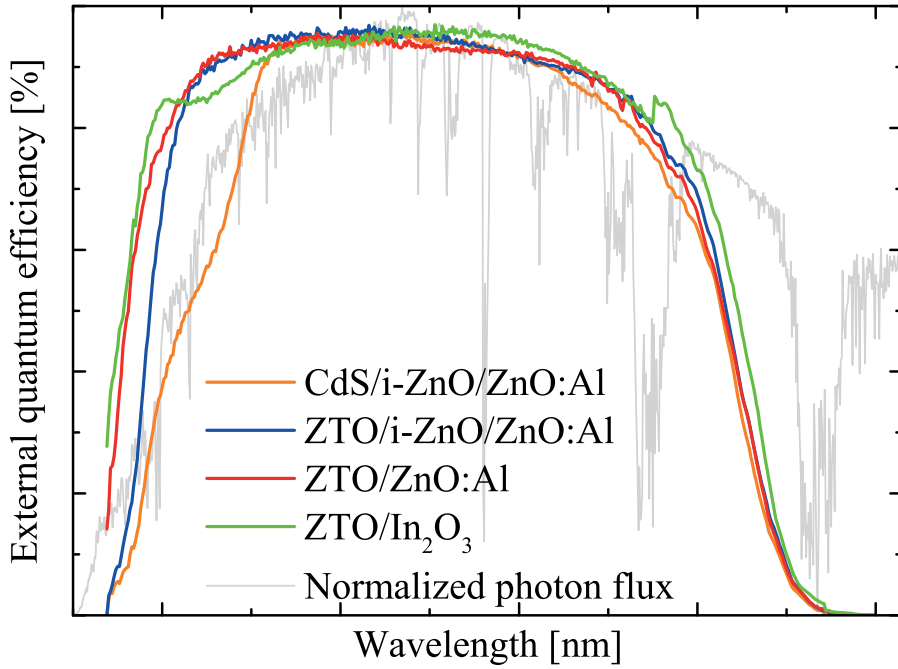


Figure 7.2. EQE curves for four different window layer stack configurations. The CdS/i-ZnO/ZnO:Al, ZTO/i-ZnO/ZnO:Al and ZTO/ZnO:Al are from paper III, while the ZTO/In₂O₃ is from paper VI. In the background the normalized photon flux of the AM1.5 spectrum is shown.

Furthermore, Figure 7.1 demonstrates that the measured direct optical E_g of In₂O₃ is higher than the optical E_g of the i-ZnO/ZnO:Al stack. In₂O₃ has a relatively small fundamental E_g of 2.8 eV, but since transitions from the highest valence band states into the conduction band is forbidden the onset of strong absorption in In₂O₃ takes place at about 3.7 eV [87][88][89]. This means that it is rather the ZTO than the In₂O₃ in the ZTO/In₂O₃ window layer stack that absorbs the photons in the UV-blue region of the solar spectrum. It should be mentioned that the difference between ZTO/ZnO:Al and ZTO/In₂O₃ window layer stack are very small in this region, as Figure 7.2 illustrates. Furthermore, as Figure 7.2 shows, this difference is negligible from a solar cell performance perspective since the photon flux at $\lambda > 350$ nm is very low in the AM1.5 spectrum.

It should be noted that there are some difference between the series in paper III and VI which Figure 7.2 are composed of, such as different CIGS, EQE setup and AR recipes. This means that a straight forward comparison between the ZTO/In₂O₃ and the other window layer stacks can't be made in other aspects than the E_g of the different window layers. One can e.g. get the impression from Figure 7.2 that the ZTO/In₂O₃ stack does not yield a higher

current production in the >700 nm wavelength region, as the discussion above states that it should. However, if one looks in the IQE-curves in paper VI one can see the improved current collection in this region for the In_2O_3 front contact as compared to an i-ZnO/ZnO:Al stack.

Table 7.1 Average J-V parameters and standard deviation for 32 cells on each sample that contain different window layer constellations. The electrical properties for the different TCO are also added.

Parameter	ZTO/ In_2O_3	ZTO/i-ZnO/AZO	CdS/i-ZnO/AZO
J-V Characteristics			
V_{OC} [mV]	631 ± 2	638 ± 2	672 ± 3
J_{SC} [mA/cm^2]	36.3 ± 0.2	34.6 ± 0.2	32.1 ± 0.2
FF [%]	72.7 ± 0.4	72.8 ± 0.9	74.0 ± 0.9
η [%]	16.6 ± 0.2	16.1 ± 0.3	16.0 ± 0.3
A	1.73 ± 0.03	1.61 ± 0.09	1.73 ± 0.08
R_s [Ωcm^2]	0.34 ± 0.06	0.69 ± 0.18	0.45 ± 0.13
J_0 [nA/cm^2]	29 ± 8	11 ± 7	14 ± 8
Electrical properties			
n [$1/\text{cm}^2$]	2.3×10^{20}	7.3×10^{20}	7.3×10^{20}
μ [cm^2/Vs]	46	13	13
d [nm]	205	255	255
R_{SH} [Ω/sq]	29	28	28
ρ [Ωcm]	5.9×10^{-4}	6.4×10^{-4}	6.4×10^{-4}

The performance of the three window layer stacks CdS/i-ZnO/ZnO:Al , ZTO/i-ZnO/ZnO:Al and $\text{ZTO/In}_2\text{O}_3$ are compared in Table 7.1. The $\text{CdS/In}_2\text{O}_3$ stack is not included since ALD growth of the In_2O_3 on CdS is not possible with the above described process due to the mentioned nucleation problem. As can be seen, the $\text{ZTO/In}_2\text{O}_3$ stack yields as expected the highest J_{SC} values and the improvement, as compared to the traditional CdS/i-ZnO/ZnO:Al , is more than $4 \text{ mA}/\text{cm}^2$. However, as usually when using the alternative ZTO buffer layer, a lower V_{OC} and slightly lower FF are obtained. Comparing $\text{ZTO/In}_2\text{O}_3$ and the ZTO/i-ZnO/ZnO:Al stack, a small decrease in V_{OC} is observed. This might be related to that In_2O_3 has a slightly larger work function than ZnO , which could affect the band alignment at the TCO/Buffer interface in a less favorable way. Despite the lower V_{OC} and FF the $\text{ZTO/In}_2\text{O}_3$ outperform the traditional CdS/i-ZnO/ZnO:Al layer with about 0.6 % (total) due to the large increase in J_{SC} .

8. Concluding remarks and outlook

The main topic of this thesis is to investigate ALD ZTO as a buffer layer in thin film CIGS solar cells. ZTO is a wide band gap semiconductor material and it is shown in this thesis that it can be uniformly and conformably grown on CIGS. The interface between the ZTO layer and CIGS is sharp and no diffusion of elements across the interface seems to occur at deposition temperatures up to the highest investigated temperature of 180 °C. The composition of ALD grown ZTO is controlled by the relative number of zinc or tin containing precursor pulses. The band gap, and consequently the conduction band energy level, of ALD ZTO demonstrates a non-trivial dependence on the $[\text{Sn}]/([\text{Zn}]+[\text{Sn}])$ composition. Furthermore, it is shown that the deposition temperature affects the band gap and conduction band energy level of ZTO due to quantum confinement effects manifested through temperature dependent changes in the monocrystalline structure of the ZTO films. Thus, it is possible to change the conduction band level of ZTO and match it with the conduction band of the CIGS absorber, so that a favorable conduction band offset and good solar cell performance can be achieved. This can be done by either changing the zinc to tin containing precursor pulse ratio or/and the deposition temperature. In this thesis, CIGS with a $[\text{Ga}]/([\text{In}]+[\text{Ga}])$ composition of about 0.25-0.3 at the absorber/buffer interface is used, which corresponds to a band gap energy of roughly 1.15 eV. It is found that a favorable conduction band offset is formed between CIGS and ZTO at deposition temperatures between 105-135 °C and for an ALD $\text{Sn}/(\text{Zn}+\text{Sn})$ pulse cycle fraction of 0.4, which corresponds to $[\text{Sn}]/([\text{Zn}]+[\text{Sn}])$ composition of approximately 0.2.

If one considers the solar AM1.5 spectrum, there exist two theoretical conversion efficiency maxima of 32.8 % and 33 % at the absorber band gap energies of 1.15 eV or 1.35 eV, respectively. So far, all of the reported best cells among different research groups are for CIGS with band gap energies close to the 1.15 eV maxima. The reasons for this is much debated, but one explanation is that a cliff conduction band offset is formed between CdS and the high band gap CIGS. The findings in this thesis that the conduction band energy level of ZTO can be increased further by lowering the ALD deposition temperature, which opens up the possibility to establish suitable conduction band offsets for high band gap CIGS. This can enable studies of CIGS with absorber band gap energies close to the second theoretical maxima for increased conversion efficiency.

CIGS cells that contain a ZTO buffer layer demonstrate in general higher J_{SC} , but lower V_{OC} , and in the end comparable efficiencies to cells with the traditional CdS buffer layer. The higher J_{SC} is due to lower parasitic absorption in ZTO as compared to CdS. The reason for the lower V_{OC} is not yet completely understood and further studies of, for example the interface, could give valuable insights into the function of this buffer layer, but also for alternative buffer layers in general.

It can be concluded that ALD ZTO is a good candidate as a cadmium free buffer layer in CIGS solar cells since similar efficiencies as compared to CdS are obtained, or even higher when combined with the In_2O_3 TCO front contact. Furthermore, it is found in this thesis that about 15 nm thin ZTO buffer layers are sufficient to fabricate highly efficient CIGS solar cells. This is an advantage from a production point of view since it means both a low material consumption, but also that the lower growth rate of ALD is a minor drawback. The low ALD growth rate might also be compensated by the fact that ALD is a vacuum based process, where the deposition of both the absorber and the front contact usually is done with vacuum methods as well. Therefore one can in a process line save time if the vacuum does not need to be broken for the buffer deposition step and if the scribing step work in vacuum. One possible way of increasing the deposition rate is to develop a chemical vapor deposition process that yields ZTO with the same material properties as for ALD, because the CVD method shows higher deposition rates in general. Finally, another advantage for the ZTO buffer layer is that it seems like the i-ZnO layer can be omitted, which means one less process step, and therefore savings due to less material consumption, shorter process times and lower equipment costs.

Summary in Swedish

På grund av utnyttjandet av fossila bränslen förväntas utsläppen av växthusgaser öka och FN förutspår genom sitt organ IPCC att den globala medeltemperaturen vid jordytan kommer att öka med mellan 3,7 °C till 4,8 °C till år 2100 jämfört med förindustriella nivåer. Globalt står energisektorn för ungefär 80 % av alla utsläpp av växthusgaser. Därför behöver krafttag göras för att fasa ut de fossila energislagen genom att introducera en förnyelsebar och miljövänlig energiförsörjning.

Den solinstrålning som träffar jorden är källan till mer än 99,9% av alla förnyelsebara energiflöden. En liten del av solenergin omvandlas till vind, strömmande vatten, temperaturgradienter, saltgradienter och till den energi som är bunden i växter och djur. Den sammanlagda energin i det ljus som varje år träffar jordens yta är ungefär 8000 gånger större än mänsklighetens totala energiförbrukning. Därför har tekniker som direkt utnyttjar solenergin den största potentialen bland alla förnyelsebara energikällor. Ett sätt att omvandla solenergi till elektricitet är med hjälp av en teknik som kallas solceller.

Dagens kommersiella solceller bygger på halvledarteknik och är dioder som har utvecklats för att omvandla energin i ljus till elektrisk energi. En diod består av två halvledarmaterial som är anslutna till två elektriska terminaler. De två halvledarmaterialen är dopade så att det ena materialet har ett överskott av termiskt exciterade elektroner i ledningsbandet (n-doping) medan det andra har ett underskott av termiskt exciterade elektroner i ledningsbandet och därmed vakanser i valensbandet (p-doping). En elektronvakans kan ses som en imaginär partikel med en positiv laddning och kallas för ett hål. Vid övergången mellan de två halvledarmaterialen skapas ett elektriskt fält i solcellsdioden. När ljus träffar en solcell absorberas fotonerna av elektroner som exciteras i materialet och elektron-hål-par bildas. Dessa laddningsbärare separeras av pn-övergångens elektriska fält och därför genereras en nettostöm i solcellen samt en elektrisk uteffekt om solcellen ansluts till en krets med en elektrisk last.

Det halvledarmaterial som dominerar solcellsmarknaden idag är kisel. En nackdel med kisel är att materialet är relativt dåligt på att absorbera ljus och det krävs skivor som är några hundra mikrometer tjocka för att effektivt absorbera allt inkommande solljus. Ett sätt att minska materialåtgången, och på

så vis potentiellt sänka produktionskostnaderna, är att göra solceller av halvledarmaterial som är bättre på att absorbera ljus än vad kisel är. Dessa typer av solceller är allmänt kallade tunnfilmssolceller. Det finns för närvarande tre kommersiella tunnfilmstekniker; amorft kisel, kadmiumtellurid och koppar-indium-gallium-selenid.

Den här avhandlingen behandlar solceller av typen koppar-indium-gallium-selenid (CIGS). CIGS är ett p-dopat material, och för att bilda en pn-övergång behövs ett n-dopat material ovanpå det ljusabsorberande CIGS-skiktet. I CIGS-solceller utgörs den n-dopade delen vanligtvis av tre skikt, som kollektivt kallas för fönsterlagren eftersom de behöver ha hög transmitans. Det översta av dessa skikt är en ledande transparent framkontakt, vilket vanligtvis utgörs av aluminium dopad zinkoxid (ZnO:Al). Det mellersta skiktet är ett hög-resistivt skikt som är till för att minska inverkan av lokala defekter i solcellen. Detta skikt består typiskt av odopad zinkoxid (i-ZnO). Det tredje skiktet, vilket är det lager som är närmast CIGS-lagret, kallas för buffertlagret. Buffertlagrets funktion är att skapa en optimerad övergång mellan CIGS-lagret och de efterföljande ZnO-lagrens egenskaper som leder till en effektiv transport av elektroner.

Traditionellt används ett buffertlager bestående av kadmiumsulfid (CdS) i CIGS-solceller. CdS är det buffertlager som hittills gett de bäst presterande solcellerna med den högsta verkningsgraden. Det finns dock vissa nackdelar med CdS , så som att kadmium är ett ämne som är klassificerat som giftigt och att CdS absorberar ljus från det UV-blå området av solens spektrum. Att utveckla högtransparenta och kadmium-fria material som alternativ till CdS är därför ett viktigt forskningsområde inom utvecklingen av CIGS-solceller. Den här avhandlingen behandlar halvledarmaterialet zink-tenn-oxid, $\text{Zn}_{1-x}\text{Sn}_x\text{O}_y$ eller ZTO, som är en lovande ersättare till CdS . Den beläggningsmetod som har använts för att växa zink-tenn-oxiden är atomlagerdeponering, ALD. ALD är en kemisk tunnfilmsteknik som är baserad på en sekventiell pulsning av reaktiva föreningar. Dessa föreningar reagerar ett i taget med ytan av ett material i en självbegränsande process. Genom att upprepa ett prov för exponeringen av de reaktiva föreningarna växer en film långsamt fram. Avhandlingen analyserar hur förändringar i ALD processen påverkar materialegenskaperna hos zink-tenn-oxiden, och hur dessa i sin tur påverkar prestandan hos CIGS-solceller.

Resultaten från materialanalyser i avhandlingen visar att ALD-metoden kan deponera zink-tenn-oxid i uniforma filmer med god stegtäckning på den ojämna CIGS ytan. Vidare visar undersökningar av gränsytan att övergången mellan CIGS-lagret och zink-tenn-oxiden är skarp och ingen diffusion av ämnen över gränsytan har uppmäts. Zink-tenn-oxidens sammansättning styrs av förhållandet mellan antalet ALD-pulser av de zink- och tennföreningar som används. Zink-tenn-oxidens sammansättning påverkar materi-

alets bandgap och ledningsbandets energinivå. Vidare så visar analyserna i avhandlingen att även beläggningstemperaturen påverkar zink-tenn-oxidens bandgap. En förklaring kan vara att zink-tenn-oxiden innehåller små nanokristaller av ZnO, eller tenn-dopad ZnO, som är tillräckligt små för att ge upphov till kvanteffekter som påverkar bandgapet. När deponeringstemperaturen och/eller zinkinnehållet ökas så blir dessa nanokristaller större, vilket resulterar i att zink-tenn-oxidens effektiva bandgap blir mindre. Det är sålunda möjligt att ändra nivån hos zink-tenn-oxidens ledningsband genom att ändra på sammansättningen och/eller beläggningstemperaturen, vilket gör att en bra matchning mellan zink-tenn-oxiden och CIGS-lagret kan uppnås. I denna avhandling har CIGS med ett bandgap på ungefär 1.15 eV använts och den bästa prestandan för ZTO-buffertlagret uppnås för en $[Sn]/([Zn]+[Sn])$ sammansättning runt 0.2 och en beläggningstemperatur på 120 °C.

En genomgående observation i avhandlingen är att solceller som innehåller ZTO-buffertlager typiskt genererar högre ström, men lägre spänning jämfört med referensceller innehållande CdS-buffertlagret. Att ZTO-buffertlagret genererar en högre ström beror på att zink-tenn-oxiden är mer transparent än kadmiumsulfiden i det UV-blå området av solens spektrum, och därmed släpper igenom fler av dessa fotoner ner till CIGS-lagret. Orsaken till den lägre spänningen är ännu inte helt klarlagd, men kan bero på att dopningsprofilerna för ZTO-buffertlagret och CdS-buffertlagret är olika samt att gränsskiktet mellan ZTO-buffertlagret och CIGS-lagret innehåller fler orenheter jämfört med gränsskiktet mellan CdS-buffertlagret och CIGS-lagret. Vinsten i ström för ZTO-buffertlagret motverkas av förlusten i spänning och i slutändan har celler med ZTO-buffertlagret jämförbar verkningsgrad med solceller som har det traditionella CdS-buffertlagret.

En stor fördel med ALD-metoden är möjligheten att belägga jämntjocka filmer på ojämna underlag. Därför behövs bara 15 nm tunna ZTO-buffertlager för att producera CIGS-solceller med en verkningsgrad på upp till 18.2 %. En annan observation är att zink-tenn-oxiden är väldigt resistiv, vilket gör det möjligt att exkludera i-ZnO-skiktet i solcellsstrukturen. Därmed görs ytterligare en vinst i ström då i-ZnO har ett mindre bandgap än zink-tenn-oxiden och framkontakten av ZnO:Al. Avhandlingen visar också att en ytterligare strömkning kan uppnås om den ledande framkontakten av ZnO:Al ersätts med indiumoxid (In_2O_3), vilken har en högre transparens i hela solspektrumet. En fönsterlagerstack med ZTO/ In_2O_3 ger så stora vinster i ström att förlusterna i spänning som är förenade med användningen av ZTO-buffertlagret kompenseras, och därmed uppmäts en 0.6 % (absolut) högre verkningsgrad för ZTO/ In_2O_3 jämfört med den traditionella CdS/i-ZnO/ZnO:Al fönsterlagerstacken.

Acknowledgements

Under these five years there has been a number of people that have contributed to my work and/or well-being at the department in one way or another that I want to thank and acknowledge.

- Both of my supervisors, for your constant care and support. I also want to thank you both for the time you have spent on going through my texts with all the small mistakes I constantly make. I also wish to thank both of you for the patients you have shown regarding my involvement in the development of the Swedish PV market and my work in IEA-PVPS.
- My main supervisor Tobias, for introducing me to a very interesting research topic with plenty of potential. Your ideas have been essential for this work and your deep knowledge in chemistry has been very valuable for a physicist like me. I appreciate that you have always have had time for my questions and prioritized my projects.
- My second supervisor Marika, for running our research group and taking care of all the bureaucratic work in order for the rest of us to do the fun stuff. Furthermore, I am so impressed by your knowledge of solar cells in general and CIGS in particular and it has been a pleasure to discuss everything from conduction band offsets to the Swedish tax laws on self-consumption of PV-electricity. I have also been amazed over that you always sound so happy when I come knocking on your door and disturb you. That has made it so much easier to ask for help these years.
- Uwe, for the amazing knowledge you have about the machines in the lab and all the time you have spent helping me fix these antagonists. Please let me know if you ever decide to scrap MrPilote, because I have long yearned to hit that rascal with a sledgehammer. I also wish to thank you for being a worthy board game opponent and being an inspiration as a lecturer.
- Lotten, for having a positive attitude that rubs off on others.
- My predecessor Adam, for handing over a smooth path for me to walk. Both with regards to the interesting buffer layer and the nice family of IEA-PVPS. Your help and advices the first year was very useful.
- Timo, for the contribution to the scientific work of course. But more importantly, for the pleasant company at our sunny cross-country

skiing trips in the Grövelsjön-mountains and all the fun moments plunging after balls in the sand (although you usually beat me at that).

- Piotr, for introducing me to all the fun board games and for being a supporting collocutor under our common though period.
- Tove, for always being a happy face across the desk that I have been able to throw stupid questions at.
- Carl, for the research collaboration and for that you actually have put up PV on your roof. The world needs more people like you.
- My desk-mate Christopher, for putting up with all my phone calls under spring-time and for the fun moments in Taipei.
- Jan, for bringing back some optimism as you took over the headache of MrPilote.
- Viktor, for your hard work of keeping the mean machines in the lab working and for keeping a straight face when my incompetence has screwed up one of them.
- Olivier, for your assistance with measurements in the very last minute despite a short notice.
- My father Göran, for a million things in life in general. But more specific to this work, for being one of few that have read all my papers and for the ground service under the hectic times of writing this thesis.
- My mother Anki, for all the hard work you have done for me over the years and all the opportunities that have given me. In the special context of this work, thank you for convincing me to accept the PhD position when I hesitated.
- My little brother Erik, for being a much needed support under a though period.
- My little brother Anders, it was fun to have you living, working and playing with me that summer. I wish I had more of your relaxed attitude in me.
- Maria, for the support and for keeping my spirits up during the last intensive part of compiling this thesis.

Appendix I

Profilometry

A profilometer is an instrument that uses a stylus that is moved laterally across the sample for a specified distance and specified contact force. As the stylus is moved it measures small surface variations in vertical movements as a function of position. A profilometer is used to measure surface roughness and it can also be used to determine the thickness of a thin film by measuring a thickness step.

X-ray reflectivity

X-ray reflectivity (XRR) is a technique where thin layers are investigated by an X-ray beam which is reflected at film interfaces and surface. The intensity of the reflected X-ray beam is measured at low incident angles, where the incident angle is increased from 0° up to a few degrees. The intensity of the reflected beam depends on the different electron densities in the layer/layers, which corresponds to different reflective indices in the classical optics. Total external reflection occurs at incident angles below a specific critical angle, usually around 0.3° . This critical angle is used to determine the density of a layer. Above the critical angle the reflection from the front surface of a layer along with the reflection from the interface of the layer and substrate interacts and give rise to interference fringes. The period of the interface fringes is related the thickness of the layer and a reduction in the intensity is associated to the roughness of the layer.

Electron microscopy

Optical microscopes are limited by the wavelengths of light. By using incoming electrons instead of light a thousand times better resolution can be achieved.

Scanning electron microscopy

Scanning electron microscopy (SEM) uses a focused beam of electrons to produce images of a sample. The electron beam interacts with the atoms in

the sample and produces various signals which contain information about surface topography and composition. The most common signal that is measured is the emitted secondary electrons from the sample. The number of secondary electrons depends on the material and the angle at which the beam hits the surface of the sample. A topography image of the sample surface is created by scanning the sample while the number of secondary electrons is detected.

Transmission electron microscopy

Transmission electron microscopy (TEM) also uses a beam of electrons, but the beam is in contrast to SEM transmitted through a very thin specimen. While the beam passes through the sample it interacts with the atoms and some of the electrons are absorbed. An image is created by detection of the transmitted beam, where the contrast is due to difference in absorption related to thickness and composition of the material.

Sample preparation in TEM is complicated since the specimens can at most be hundreds of nanometers thick. To thin down a sample different techniques are used such as ion etching, chemical etching, mechanical milling etc.

X-ray diffraction

X-ray diffraction (XRD) is a technique that measures the diffraction of an incident X-ray beam. The X-rays are diffracted by the electrons of the atoms in a crystalline material in many specific directions, and constructive interference occurs when conditions satisfy Bragg's Law [90]. This law relates the wavelength of X-rays to the diffraction angle and the lattice spacing in a crystalline sample. By measuring the angles and intensities of the diffracted X-rays the atomic and molecular structure of the sample along with unit cell dimensions can be identified.

Rutherford backscattering spectroscopy

In Rutherford backscattering spectroscopy (RBS) a sample is bombarded with a beam of high energy particles. The majority of the incident particles are implemented into the sample, but a small fraction of the particles collide with a nucleus of one of the surface atoms in the sample and are backscattered. The backscattered particles lose energy in passing through the material and in collisions. The energy losses depend on the stopping power of the sample material and on the masses of the beam particles and sample atoms. The number of backscattered particles that emanates from a given element in

the sample depends on the concentration of that element and its effective nucleus. It is therefore possible to determine the atomic mass, elemental concentrations and structure of materials versus depth below the surface by measuring the number and energy of the particles in the backscattered beam.

X-ray Spectroscopy

X-ray spectroscopy is a common name for material characterization techniques that use X-ray excitation of electrons, which enable element-selective studies of solid materials due to the unique core level energies for each element. Different X-ray spectroscopy methods use different parts of the chain of events that follows after an X-ray or electron beam hits an atom to gather information about the material.

When an X-ray or electron beam strikes a core electron, the electron is either excited to an unoccupied level or is ejected from the atom. Either way a core hole is created. The absorption pattern when the energy of the incident X-ray exceeds the binding energy of a core electron contains information, which is used in X-ray absorption spectroscopy (XAS) (section 0). When an electron is dissociated from an atom of a solid material (this is essentially the photoelectric effect, see section 2.3), it becomes a photoelectron and can be studied by X-ray photoelectron spectroscopy (XPS) (section 0). The photon emission that the sample emits when an electron from an outer shell fills the vacancy in an inner shell is used in the three techniques; X-ray fluorescence (XRF) (section 0), Energy dispersive X-ray spectroscopy (EDS) (section 0) and X-ray emission spectroscopy (XES) (section 0).

X-ray absorption spectroscopy

X-ray absorption spectroscopy (XAS) is a technique used to determine the local electronic structure of matter by tuning the X-ray energy to a range where core electrons start to be excited or ejected. This requires intense and tunable X-ray beams so a synchrotron radiation source is used. If one plots X-ray absorption as a function of energy, there is an abrupt increase in absorbance that occurs when the X-ray energy exceeds the binding energy of a core electron. These so-called absorption edges represent a core level and can be used for elemental identification as each element has specific core electron binding energies. Furthermore, in XAS the pattern of an absorption edge can be used to gain information about, among other things; the local structure, energy level of the conduction band, oxidation state and crystal bond lengths [91].

X-ray photoelectron spectroscopy

X-ray photoelectron spectroscopy (XPS), also known as electron spectroscopy for chemical analysis (ESCA) is a surface analysis method. In XPS the surface of a sample is excited by X-rays, causing photoelectrons to be emitted from the sample surface, and the binding energy calculated from an electron energy analyzer is used to measure the kinetic energy and the number of the emitted photoelectrons. From the binding energy and intensity of a photoelectron peak, the element identity, chemical state, and quantity of a detected element can be determined.

Energy dispersive X-ray spectroscopy

Energy-dispersive X-ray spectroscopy (EDS) analyses the X-rays that an atom emits when an electron from an outer shell fills the vacancy in an inner shell. A high-energy beam of charged particles, such as electrons or protons, is concentrated on the sample to give rise to the emission of characteristic X-rays from a material. The number and energy of the photons emitted from the material, as a result of the relaxation of an outer shell electron, is then measured. This allows the elemental composition of a sample to be determined. EDS is widely used in electron microscopes since these already are equipped with an electron beam.

X-ray fluorescence

The X-ray fluorescence (XRF) technique is based on the same kind of physical process as EDS, namely analyzing the characteristic photons that an atom emits when an electron from an outer shell fill the vacancy in an inner shell.

The main difference between EDS and XRF is that in XRF X-rays are used instead of charged particles. The difference between using particles and X-rays is that X-rays usually penetrate deeper into the sample and therefore get a more in-depth uniform signal. On the other hand, it is easier to achieve a higher surface resolution with a concentrated beam of particles, than with X-rays.

X-ray emission spectroscopy

X-ray emission spectroscopy (XES) is based on the same principle as X-ray fluorescence (XRF) but uses only low energy wavelength-tunable X-rays generated in a synchrotron, usually in combination with XAS. The low energy X-rays excite the core electrons to higher energy levels and the fluorescence that is emitted at the relaxation is measured. That allows XES to provide information about the partial occupied density of electronic states of a material. Combining the XAS and XES makes in-depth investigations of the

band gap of a material possible as XAS reveal information about the conduction band and XES about the valence band.

Secondary ion mass spectroscopy

Secondary ion mass spectrometry (SIMS) is a technique that uses sputtering of solid materials to eject secondary ions, where mass/charge ratios are measured with a mass spectrometer, to determine the composition of a sample. Different materials have different ionization probabilities which make SIMS in general a qualitative technique. SIMS is an analysis technique that can detect elements in the range from parts per million to parts per billion. SIMS is used for bulk investigations by using the sputtering to dig down through the sample while measuring the composition. One can thereby get information about composition gradients in samples.

Reflectance-transmittance spectroscopy

Reflectance-transmittance measurements are usually done with setups containing integrating spheres. An integrating sphere is a hollow spherical cavity that has its walls covered with a scattering white reflective coating and that has small holes for entrance and exit ports. The sample and detector are mounted to the integrating sphere in such a way that only light that has been scattered in the sphere leaves the port to the detector. By having a white reflective coating that allows photons to be scattered many times the assumption can be made that all of the light that enters the sphere also leaves the sphere at the port leading to the detector. Integrating spheres are therefore good for measurement of the total reflectance and transmittance of materials.

Ellipsometry

Ellipsometry is an optical technique which measures the change in polarization from a sample as it is subjected to radiation. The change in polarization then needs to be compared to a model, which can be rather complicated, to obtain sample properties such as the refractive index, the dielectric function, thickness, electrical conductivity, etc.

Four point probe

A four point probe setup is a simple method for measuring the sheet resistivity of i.e. thin semiconductor layers. By passing a current through two outer probes and measuring the voltage through two inner probes the sheet resistivity of a layer can be determined. The resistivity can be calculated if the thickness of the layer is known, or one can calculate the thickness of the layer if the resistivity is known.

Hall measurement

Hall measurements are used for determining the carrier density, mobility and ultimately the resistivity in semiconductor materials. The method is based on the Hall effect [92]. If a perpendicular magnetic field is applied on a semiconductor where an electric current flows, the magnetic field will exert a transverse force upon the moving charge carriers, which will push them towards one side of the semiconductor. The buildup of charge at this side will give rise to a measurable voltage between the two sides of the semiconductor, which is referred to as the Hall effect. The strength of the voltage will depend on the strength of the magnetic field and the type, number, and properties of the charge carriers in the semiconductor.

References

- [1] O. Edenhofer, R. Pichs-Madruga, Y. Sokona, E. Farahani, S. Kadner, K. Seyboth, A. Adler, I. Baum, S. Brunner, P. Eickemeier, B. Kriemann, J. Savolainen, S. Schlömer, C. von Stechow, T. Zwickel, and J. C. Minx, “IPCC, 2014: Summary for Policymakers,” in *Climate Change 2014: Mitigation of Climate Change. Contribution of Working Group III to the Fifth Assessment Report on the Intergovernmental Panel on Climate Change*, no. November 2014, Cambridge University Press, Cambridge, United Kingdom and New York, NY, USA.
- [2] M. Wild, D. Folini, C. Schär, N. Loeb, E. G. Dutton, and G. König-Langlo, “The global energy balance from a surface perspective,” *Clim. Dyn.*, vol. 40, no. 11–12, pp. 3107–3134, 2013.
- [3] B. Sandén, L. Hammar, and F. Hedenus, *Systems Perspectives on Renewable Power 2014*. 2014.
- [4] IEA, “Key world energy statistics,” Paris, 2014.
- [5] E. Becquerel, “Mémoire sur les effets électriques produits sous l’influence des rayons solaires,” *Comptes Rendus*, vol. 9, pp. 561–567, 1839.
- [6] A. Einstein, “Über einen die erzeugung und verwandlung des liches betreffenden heuristischen gesichtspunkt,” *Ann. Phys.*, vol. 17, no. 6, pp. 132–148, 1905.
- [7] D. M. Chapin, C. S. Fuller, and G. L. Pearson, “A new silicon p-n junction photocell for converting solar radiation into electrical power,” *J. Appl. Phys.*, vol. 25, pp. 676–677, 1954.
- [8] M. a. Green, “Silicon photovoltaic modules: a brief history of the first 50 years,” *Prog. Photovoltaics Res. Appl.*, vol. 13, no. 5, pp. 447–455, Aug. 2005.
- [9] IEA, “Technology Roadmap: Solar Photovoltaic Energy - 2014 edition,” Paris, 2014.
- [10] IEA-PVPS, “Snapshot of Global PV Markets 2014,” 2015.
- [11] NREL, “Best research-cell efficiencies.” [Online]. Available: http://www.nrel.gov/ncpv/images/efficiency_chart.jpg. [Accessed: 28-May-2015].
- [12] M. P. Waalkes, “Cadmium carcinogenesis in review,” *J. Iorganic Biochem.*, vol. 79, no. 1–4, pp. 241–244, Apr. 2000.
- [13] W. Pauli, “Über den zusammenhang des abschlusses der elektronengruppen im atom mit der komplexstruktur der spektren,” *Zeitschrift für Phys.*, vol. 31, pp. 765–783, 1925.
- [14] W. Shockley and W. T. Read, “Statistics of the recombination of holes and electrons,” *Phys. Rev.*, vol. 87, no. 5, pp. 835–842, 1952.
- [15] S. M. Sze, *Semiconductor devices: Physics and technology*, 2nd ed. John Wiley & Sons, 2002.

- [16] W. Shockley, *Electrons and holes in semiconductors with applications to transistor electronics*. New York: D. Van Nostrand, 1950.
- [17] M. A. Green, *Solar cells: Operating principles, technology and system applications*. Kensington: University of New South Wales, 1998.
- [18] P. Reinhard, S. Buecheler, and a. N. Tiwari, "Technological status of Cu(In,Ga)(Se,S)₂-based photovoltaics," *Sol. Energy Mater. Sol. Cells*, vol. 119, pp. 287–290, Dec. 2013.
- [19] S. Niki, M. Contreras, I. Repins, M. Powalla, K. Kushiya, S. Ishizuka, and K. Matsubara, "CIGS absorbers and processes," *Prog. Photovoltaics Res. Appl.*, vol. 18, no. 6, pp. 453–466, 2010.
- [20] P. Jackson, D. Hariskos, R. Wuerz, O. Kiowski, A. Bauer, T. M. Friedlmeier, and M. Powalla, "Properties of Cu(In,Ga)Se₂ solar cells with new record efficiencies up to 21.7%," *Phys. status solidi - Rapid Res. Lett.*, vol. 9, no. 1, pp. 28–31, 2015.
- [21] W. N. Shafarman and L. Stolt, *Cu(InGa)Se₂ Solar Cells*. 2003.
- [22] U. P. Singh and S. P. Patra, "Progress in Polycrystalline Thin-Film Cu(In,Ga)Se₂ Solar Cells," *Int. J. Photoenergy*, vol. 2010, pp. 1–19, 2010.
- [23] H. Neumann, "Optical properties and electronic band structure of CuInSe₂," *Sol. Cells*, vol. 16, pp. 317–333, 1986.
- [24] S. H. 1250–1253 Nadenau V, Hariskos D, "CuGaSe₂ based thin film solar cells with improved performance," in *Proceedings of 14th European Photovoltaic Solar Energy Conference*, 1997, pp. 1250–1253.
- [25] M. I. Alonso, M. Garriga, C. A. Durante Rincón, E. Hernández, and M. León, "Optical functions of chalcopyrite CuGa_xIn_{1-x}Se₂ alloys," *Appl. Phys. A*, vol. 74, pp. 659–664, 2002.
- [26] J. Schöldström, U. Zimmermann, and M. Edoff, "Dynamic radiative properties of the Cu(In,Ga)Se₂ layer during the co-evaporation process," *Prog. Photovoltaics Res. Appl.*, vol. 18, no. 5, pp. 321–327, 2010.
- [27] W. Shockley and H. J. Queisser, "Detailed balance limit of efficiency of p-n junction solar cells," *J. Appl. Phys.*, vol. 32, no. 3, pp. 510–519, 1961.
- [28] S. Siebentritt, "What limits the efficiency of chalcopyrite solar cells?," *Sol. Energy Mater. Sol. Cells*, vol. 95, no. 6, pp. 1471–1476, Jun. 2011.
- [29] O. Lundberg, "Band gap profiling and high speed deposition of Cu(In,Ga)Se₂ for thin film solar cells," Uppsala University, 2003.
- [30] I. Repins, M. a. Contreras, B. Egaas, C. DeHart, J. Scharf, C. L. Perkins, B. To, and R. Noufi, "19.9%-efficient ZnO/CdS/ CuInGaSe₂ Solar Cell with 81.2% Fill Factor," *Prog. Photovoltaics Res. Appl.*, vol. 16, no. 3, pp. 235–239, 2008.
- [31] P. Jackson, D. Hariskos, E. Lotter, S. Paetel, R. Wuerz, R. Menner, W. Wischmann, and M. Powalla, "New world record efficiency for Cu(In,Ga)Se₂ thin-film solar cells beyond 20%," *Prog. Photovoltaics Res. Appl.*, vol. 19, pp. 894–897, 2011.
- [32] J. Kessler, M. Bodegård, J. Hedström, and L. Stolt, "Baseline Cu(In,Ga)Se₂ device production: Control and statistical significance," *Sol. Energy Mater. Sol. Cells*, vol. 67, pp. 67–76, 2001.

- [33] P. Salomé, V. Fjällström, P. Szaniawski, J. Leitão, A. Hultqvist, P. Fernandes, J. Teixeira, B. Falcão, U. Zimmermann, A. da Cunha, and M. Edoff, "A comparison between thin film solar cells made from co-evaporated $\text{CuIn}_{1-x}\text{Ga}_x\text{Se}_2$ using a one-stage process versus a three-stage process," *Prog. Photovoltaics Res. Appl.*, vol. 23, pp. 470–478, 2015.
- [34] S. Schleussner, U. Zimmermann, T. Wätjen, K. Leifer, and M. Edoff, "Effect of gallium grading in $\text{Cu}(\text{In,Ga})\text{Se}_2$ solar-cell absorbers produced by multi-stage coevaporation," *Sol. Energy Mater. Sol. Cells*, vol. 95, no. 2, pp. 721–726, 2011.
- [35] N. Naghavi, D. Abou-Ras, N. Allsop, N. Barreau, S. Bücheler, A. Ennaoui, C.-H. Fischer, C. Guillen, D. Hariskos, J. Herrero, R. Klenk, K. Kushiya, D. Lincot, R. Menner, T. Nakada, C. Platzer-Björkman, S. Spiering, A. N. Tiwari, and T. Törndahl, "Buffer layers and transparent conducting oxides for chalcopyrite $\text{Cu}(\text{In,Ga})(\text{S,Se})_2$ based thin film photovoltaics: present status and current developments," *Prog. Photovoltaics Res. Appl.*, vol. 18, no. 6, pp. 411–433, Sep. 2010.
- [36] W. Witte, S. Spiering, and D. Hariskos, "Substitution of the CdS buffer layer in CIGS thin-film solar cells," *Vak. Forsch. und Prax.*, vol. 26, no. 1, pp. 23–27, Feb. 2014.
- [37] U. Rau and M. Schmidt, "Electronic properties of $\text{ZnO}/\text{CdS}/\text{Cu}(\text{In,Ga})\text{Se}_2$ solar cells -aspects of heterojunction formation," *Thin Solid Films*, vol. 387, pp. 141–146, 2001.
- [38] S. Ishizuka, K. Sakurai, a. Yamada, K. Matsubara, P. Fons, K. Iwata, S. Nakamura, Y. Kimura, T. Baba, H. Nakanishi, T. Kojima, and S. Niki, "Fabrication of wide-gap $\text{Cu}(\text{In}_{1-x}\text{Ga}_x)\text{Se}_2$ thin film solar cells: a study on the correlation of cell performance with highly resistive i-ZnO layer thickness," *Sol. Energy Mater. Sol. Cells*, vol. 87, no. 1–4, pp. 541–548, May 2005.
- [39] U. Rau and H. W. Schock, "Electronic properties of $\text{Cu}(\text{In,Ga})\text{Se}_2$ heterojunction solar cells—recent achievements, current understanding, and future challenges," *Appl. Phys. A*, vol. 69, pp. 131–147, 1999.
- [40] R. Klenk, "Characterisation and modelling of chalcopyrite solar cells," *Thin Solid Films*, vol. 387, pp. 135–140, 2001.
- [41] T. Törndahl, C. Platzer-Björkman, J. Kessler, and M. Edoff, "Atomic layer deposition of $\text{Zn}_{1-x}\text{Mg}_x\text{O}$ buffer layers for $\text{Cu}(\text{In,Ga})\text{Se}_2$ solar cells," *Prog. Photovoltaics Res. Appl.*, vol. 15, pp. 225–235, 2007.
- [42] M. Turcu, O. Pakma, and U. Rau, "Interdependence of absorber composition and recombination mechanism in $\text{Cu}(\text{In,Ga})(\text{Se,S})_2$ heterojunction solar cells," *Appl. Phys. Lett.*, vol. 80, no. 14, pp. 2598–2600, 2002.
- [43] T. Minemoto, T. Matsui, H. Takakura, Y. Hamakawa, T. Negami, Y. Hashimoto, T. Uenoyama, and M. Kitagawa, "Theoretical analysis of the effect of conduction band offset of window/CIS layers on performance of CIS solar cells using device simulation," *Sol. Energy Mater. Sol. Cells*, vol. 67, pp. 83–88, 2001.
- [44] M. Gloeckler and J. R. Sites, "Efficiency limitations for wide-band-gap chalcopyrite solar cells," *Thin Solid Films*, vol. 480–481, pp. 241–245, 2005.

- [45] J. M. Doña and J. Herrero, "Dependence of electro-optical properties on the deposition conditions of chemical bath deposited CdS thin films," *J. Electrochem. Soc.*, vol. 144, no. 11, pp. 4091–4098, 1997.
- [46] M. J. Furlong, M. Froment, M. C. Bernard, R. Cortés, A. N. Tiwari, M. Krejci, H. Zogg, and D. Lincot, "Aqueous solution epitaxy of CdS layers on CuInSe₂," *J. Cryst. Growth*, vol. 193, pp. 114–122, 1998.
- [47] T. Wada, S. Hayashi, Y. Hashimoto, and S. Nishiwaki, "High efficiency Cu(In,Ga)Se₂ (CIGS) solar cells with improved CIGS surface," in *2nd World Conference and Exhibition on Photovoltaic Solar Energy Conversion*, 1998, pp. 403–408.
- [48] D. Lincot, R. Ortega-Borges, J. Vedel, M. Ruckh, J. Kessler, K. O. Velthaus, D. Hariskos, and H. W. Schock, "Chemical bath deposition of CdS on CuInSe₂: combining dry and wet processes for high efficiency thin film solar cells," in *11th. E.C. Photovoltaic Solar Energy Conference*, 1992, pp. 870–873.
- [49] R. L. Puurunen, "Surface chemistry of atomic layer deposition: A case study for the trimethylaluminum/water process," *J. Appl. Phys.*, vol. 97, no. 12, p. 121301, 2005.
- [50] W. Niu, X. Li, S. K. Karuturi, D. W. Fam, H. Fan, S. Shrestha, L. H. Wong, and A. I. Y. Tok, "Applications of atomic layer deposition in solar cells," *Nanotechnology*, vol. 26, no. 6, p. 064001, 2015.
- [51] J. A. van Delft, D. Garcia-Alonso, and W. M. M. Kessels, "Atomic layer deposition for photovoltaics: applications and prospects for solar cell manufacturing," *Semicond. Sci. Technol.*, vol. 27, no. 7, p. 074002, Jul. 2012.
- [52] C. A. Gueymard, D. Myers, and K. Emery, "Proposed reference irradiance spectra for solar energy systems testing," *Sol. Energy*, vol. 73, no. 6, pp. 443–467, 2002.
- [53] S. S. Hegedus and W. N. Shafarman, "Thin-film solar cells: device measurements and analysis," *Prog. Photovoltaics Res. Appl.*, vol. 12, no. 23, pp. 155–176, Mar. 2004.
- [54] H. Field, "UV-VIS-IR Spectral responsivity measurement system for solar cells," in *AIP Conference Proceedings*, 1999, no. 462, pp. 629–635.
- [55] V. Nadenau, U. Rau, A. Jasenek, and H. W. Schock, "Electronic properties of CuGaSe₂-based heterojunction solar cells. Part I. Transport analysis," *J. Appl. Phys.*, vol. 87, no. 1, pp. 584–593, 2000.
- [56] M. Burgelman, P. Nollet, and S. Degraeve, "Modelling polycrystalline semiconductor solar cells," *Thin Solid Films*, vol. 361–362, pp. 527–532, 2000.
- [57] A. Holmqvist, T. Törndahl, F. Magnusson, U. Zimmermann, and S. Stenström, "Dynamic parameter estimation of atomic layer deposition kinetics applied to in situ quartz crystal microbalance diagnostics," *Chem. Eng. Sci.*, vol. 111, pp. 15–33, 2014.
- [58] T. Tynell and M. Karppinen, "Atomic layer deposition of ZnO: a review," *Semicond. Sci. Technol.*, vol. 29, no. 4, p. 043001, Apr. 2014.
- [59] J. Elam, D. Baker, A. Hryn, A. Martinson, M. Pellin, and J. Hupp, "Atomic layer deposition of tin oxide films using tetrakis(dimethylamino) tin," *J. Vac. Sci. Technol. A Vacuum, Surfaces, Film.*, vol. 26, no. 2, pp. 244–252, 2008.

- [60] J. T. Tanskanen, C. Hägglund, and S. F. Bent, "Correlating growth characteristics in atomic layer deposition with precursor molecular structure: The case of zinc tin oxide," *Chem. Mater.*, vol. 26, no. 9, pp. 2795–2802, 2014.
- [61] A. Hultqvist, C. Platzer-björkman, U. Zimmermann, M. Edoff, and T. Törndahl, "Growth kinetics, properties, performance, and stability of atomic layer deposition Zn–Sn–O buffer layers for Cu(In,Ga)Se₂ solar cells," *Prog. Photovoltaics Res. Appl.*, vol. 20, pp. 883–891, 2012.
- [62] J. Lim and C. Lee, "Effects of substrate temperature on the microstructure and photoluminescence properties of ZnO thin films prepared by atomic layer deposition," *Thin Solid Films*, vol. 515, pp. 3335–3338, Feb. 2007.
- [63] E. B. Yousfi, B. Weinberger, and F. Donsanti, "Atomic layer deposition of zinc oxide and indium sulfide layers for Cu(In,Ga)Se₂ thin-film solar cells," *Thin Solid Films*, vol. 387, pp. 29–32, 2001.
- [64] A. Yamada, B. Sang, and M. Konagai, "Atomic layer deposition of ZnO transparent conducting oxides," *Appl. Surf. Sci.*, vol. 112, pp. 216–222, 1997.
- [65] V. Lujala, J. Skarp, M. Tammenmaa, and T. Suntola, "Atomic layer epitaxy growth of doped zinc oxide thin films from organometals," *Appl. Surf. Sci.*, vol. 82/83, pp. 34–40, 1994.
- [66] M. N. Mullings, C. Hägglund, and S. F. Bent, "Tin oxide atomic layer deposition from tetrakis(dimethylamino)tin and water," *J. Vac. Sci. Technol. A Vacuum, Surfaces, Film.*, vol. 31, no. 6, p. 061503, 2013.
- [67] J. Sterner, "ALD buffer layer growth and interface formation on Cu(In,Ga)Se₂ solar cell absorbers," Uppsala University, 2004.
- [68] S. Baruah and J. Dutta, "Zinc stannate nanostructures: hydrothermal synthesis," *Sci. Technol. Adv. Mater.*, vol. 12, no. 1, p. 013004, Feb. 2011.
- [69] A. Hultqvist, M. Edoff, and T. Törndahl, "Evaluation of Zn–Sn–O buffer layers for CuIn_{0.5}Ga_{0.5}Se₂ solar cells," *Prog. Photovoltaics Res. Appl.*, vol. 19, no. 4, pp. 478–481, 2011.
- [70] M. N. Mullings, C. Hägglund, J. T. Tanskanen, Y. Yee, S. Geyer, and S. F. Bent, "Thin film characterization of zinc tin oxide deposited by thermal atomic layer deposition," *Thin Solid Films*, vol. 556, pp. 186–194, Apr. 2014.
- [71] J. Heo, S. Bok Kim, and R. G. Gordon, "Atomic layer deposited zinc tin oxide channel for amorphous oxide thin film transistors," *Appl. Phys. Lett.*, vol. 101, no. 11, p. 113507, 2012.
- [72] M. K. Jayaraj, K. J. Saji, K. Nomura, T. Kamiya, and H. Hosono, "Optical and electrical properties of amorphous zinc tin oxide thin films examined for thin film transistor application," *J. Vac. Sci. Technol. B Microelectron. Nanom. Struct.*, vol. 26, no. 2, pp. 495–501, 2008.
- [73] H. Q. Chiang, J. F. Wager, R. L. Hoffman, J. Jeong, and D. a. Keszler, "High mobility transparent thin-film transistors with amorphous zinc tin oxide channel layer," *Appl. Phys. Lett.*, vol. 86, no. 1, p. 013503, 2005.
- [74] J. Tauc, "Optical properties and electronic structure of amorphous Ge and Si," *Mater. Res. Bull.*, vol. 3, pp. 37–46, 1968.
- [75] M. Cahay, *Quantum Confinement VI: Nanostructured Materials and Devices : Proceedings of the International Symposium*. The Electrochemical Society, 2001.

- [76] J. Jacobsson and T. Edvinsson, "Absorption and fluorescence spectroscopy of growing ZnO quantum dots: size and band gap correlation and evidence of mobile trap states," *Inorg. Chem.*, vol. 50, no. 19, pp. 9578–86, Oct. 2011.
- [77] J. Jacobsson and T. Edvinsson, "Photoelectrochemical determination of the absolute band edge positions as a function of particle size for ZnO quantum dots," *J. Phys. Chem. C*, vol. 116, no. 29, pp. 15692–15701, Jul. 2012.
- [78] X. Wu, "High-efficiency polycrystalline CdTe thin-film solar cells," *Sol. Energy*, vol. 77, no. 5, pp. 803–814, 2004.
- [79] A. Hultqvist, J. V. Li, D. Kuciauskas, P. Dippo, M. A. Contreras, D. H. Levi, and S. F. Bent, "Reducing interface recombination for Cu(In,Ga)Se₂ by atomic layer deposited buffer layers," *Appl. Phys. Lett.*, vol. 107, no. 3, p. 033906, 2015.
- [80] C. Platzer-Björkman, J. Lu, J. Kessler, and L. Stolt, "Interface study of CuInSe₂/ZnO and Cu(In,Ga)Se₂/ZnO devices using ALD ZnO buffer layers," *Thin Solid Films*, vol. 431–432, no. 03, pp. 321–325, 2003.
- [81] U. Rau, P. O. Grabitz, and J. H. Werner, "Resistive limitations to spatially inhomogeneous electronic losses in solar cells," *Appl. Phys. Lett.*, vol. 85, no. 24, p. 6010, 2004.
- [82] E. Burstein, "Anomalous optical absorption limit in InSb," *Phys. Rev.*, pp. 632–633, 1954.
- [83] T. Moss, "The interpretation of the properties of indium antimonide," *Proc. Phys. Soc. Sect. B*, pp. 775–782, 1954.
- [84] T. Törndahl, E. Coronel, A. Hultqvist, C. Platzer-Björkman, K. Leifer, and M. Edoff, "The effect of Zn_{1-x}Mg_xO buffer layer deposition temperature on Cu(In,Ga)Se₂ solar cells: A study of the buffer/absorber interface," *Prog. Photovoltaics Res. Appl.*, vol. 17, pp. 115–124, 2009.
- [85] A. Shimizu, S. Chaisitsak, T. Sugiyama, A. Yamada, and M. Konagai, "Zinc-based buffer layer in the Cu(InGa)Se₂ thin film solar cells," *Thin Solid Films*, vol. 362, pp. 193–197, 2000.
- [86] L. C. Olsen, H. Aguilar, F. W. Addis, W. Lei, and J. Li, "CIS solar cells with ZnO Buffer layers," in *25th IEEE Photovoltaic Specialists Conference*, 1996, pp. 997–1000.
- [87] A. Klein, C. Körber, A. Wachau, F. Säuberlich, Y. Gassenbauer, S. P. Harvey, D. E. Proffit, and T. O. Mason, "Transparent conducting oxides for photovoltaics: Manipulation of Fermi level, work function and energy band alignment," *Materials (Basel)*, vol. 3, no. 11, pp. 4892–4914, 2010.
- [88] A. Walsh, J. L. F. Da Silva, S. H. Wei, C. Körber, A. Klein, L. F. J. Piper, A. Demasi, K. E. Smith, G. Panaccione, P. Torelli, D. J. Payne, A. Bourlange, and R. G. Egdell, "Nature of the band gap of In₂O₃ revealed by first-principles calculations and X-ray spectroscopy," *Phys. Rev. Lett.*, vol. 100, no. 16, pp. 2–5, 2008.
- [89] L. F. J. Piper, A. Demasi, S. W. Cho, K. E. Smith, F. Fuchs, F. Bechstedt, C. Körber, A. Klein, D. J. Payne, and R. G. Egdell, "Electronic structure of In₂O₃ from resonant x-ray emission spectroscopy," *Appl. Phys. Lett.*, vol. 94, no. 2, pp. 0–3, 2009.
- [90] W. H. Bragg and W. L. Bragg, "The reflection of X-rays by crystals," *Proc. R. Soc. London*, vol. 88, no. 605, pp. 428–438, 1913.

- [91] J. E. Penner-hahn and A. Arbor, “X-ray absorption spectroscopy,” in *eLS*, 2005, pp. 1–4.
- [92] E. H. Hall, “On a new action of the magnet on electric currents,” *Am. J. Math.*, vol. 2, pp. 287–292, 1879.

Acta Universitatis Upsaliensis

*Digital Comprehensive Summaries of Uppsala Dissertations
from the Faculty of Science and Technology 1277*

Editor: The Dean of the Faculty of Science and Technology

A doctoral dissertation from the Faculty of Science and Technology, Uppsala University, is usually a summary of a number of papers. A few copies of the complete dissertation are kept at major Swedish research libraries, while the summary alone is distributed internationally through the series Digital Comprehensive Summaries of Uppsala Dissertations from the Faculty of Science and Technology. (Prior to January, 2005, the series was published under the title "Comprehensive Summaries of Uppsala Dissertations from the Faculty of Science and Technology".)



ACTA
UNIVERSITATIS
UPSALIENSIS
UPPSALA
2015

Distribution: publications.uu.se
urn:nbn:se:uu:diva-260882